

Department of Precision and Microsystems Engineering

Effect of instrumentation position and direction inaccuracy on the calculation of virtual point transformed FRFs

Nooshinossadat Mortazavi

Report no : 2020.009
Coach : Dr. Dennis de Klerk
Professor : Prof.Dr.Peter Steneken
Specialisation : Dynamics
Type of report : Master Thesis
Date : 27 February 2020

Master Thesis

Effect of instrumentation position and direction inaccuracy on the calculation of virtual point transformed FRFs

by

Nooshinossadat Mortazavi

to obtain the degree of Master of Science

at the Delft University of Technology,

to be defended publicly on Tuesday February ??, 2020 at 10:00 AM.

Student number: 1550349
Project duration: January 4, 2019 – February 27, 2020
Thesis committee: Prof. dr. Peter Steeneken, TU Delft, supervisor
Dr. Dennis de Klerk, TU Delft, VIBES.technology
Dr. Pooria Pahlavan,, TU Delft, supervisor

This thesis is confidential and cannot be made public until February 28, 2025.

An electronic version of this thesis is available at <http://repository.tudelft.nl/>.

Abstract

This work comprises research in the field of Experimental Dynamics. This technique is currently used in the automotive area and is used to enhance the current state of FEM with the inclusion of test-based models. Building test-based models for EDS (Experimental Dynamic Substructuring) requires very accurate measurement, and this thesis examines how uncertainty on sensors and impacts affects the accuracy of the test-based model.

Dynamic Substructuring is the collection of methods to describe large and complex systems by using the models of its substructures. This approach assumes that the dynamics of each substructure is enclosed in a so-called super element at interface DoF. Modeling domains that engage condensed dynamic information, like admittance FRFs in the frequency domain, are therefore particularly suited for substructuring [49].

One of the methods to model the interface between two (or more) substructures, is coupling two substructure by a single mutual point, so-called Virtual Point. This single point is a *collocated* point, a super-element, which has both *translational* and *rotational* DoFs.

, In order to obtain the FRF of the coupling point of each substructure, an experimentally gained information is transforming into the super-element's admittance (Virtual Point FRF). The experimentally gained information is recorded by sensors and roving impacts. The transformation uses projection matrices for both input and output and is called Virtual Points Transformation (VPT).

In all experiments, we almost always have some uncertainties, and achieving true experiments is almost impossible. Making errors while mounting the sensors and roving impacts is very plausible. This mounting errors can be **positional** as well as **directional**. Because of these uncertainties, we can never find the true transformation matrices.

In this thesis, the propagation of the positional and directional uncertainty of measuring equipment (sensors and roving impacts) into the calculation of Virtual Point frequency response function is investigated analytically, as well as numerically. It is shown *which error* and in *what extend* is the most dominant error source, and in *which frequencies* and in *which cross-functions of VP* we can expect the least precise.

Expectations can be made on the inputs' or outputs' DOF with *dominant effect on error generation for a particular mode shape*, based on the local mode shape-motion of measurement area, and by using the Component Mode Synthesized method (CMS). It is shown that the error generation on measurement, and further error propagation into super-element caused by a particular error source is mode shape- and frequency-dependent.

Further, an estimation is given for the amount of influence of each dominant error source on the calculation of the forces and responses of Virtual Point, on both rotational and translational forces and responses. Since the dominant error generation is depending on the mode shape motion, the VP's cross-functions with the least precision can also be defined.

It is shown that based on the decomposition of transformation matrices, the rotational/ rotational cross-functions are the most sensitive ones to both positional and directional uncertainties if we are looking to absolute value. Then, base on the numerical results, a comparison is made between all four studied cases; Impacts Positional Uncertainty (IPU), Impacts Directional Uncertainty (IDU), Sensors Positional Uncertainty (SPU), and Sensors Directional Uncertainty (SDU). The possibility of error cancellation and the maximum error propagation is introduced.

Acknowledgement

When I have started studying mechanical engineering at TU Delft, I was full of passion. Through the years, I've changed. I survived my journey, which was a roller coaster, with its ups and its downs. Now I feel really proud to close my journey as a mechanical student with this master thesis.

To come to this state, I was not alone. My beloved husband Farzad, my darling son Makan, my lovely parents Rezvan and Morteza, my master coordinator Eveline Matroos, my close friends Banfsheh and Hamed, my supervisor Dennis de Klerk, my mentor Farbod Alijani, Paul Woerkom, and my coach Erik, they all support me and encourage me. They believed in me when so many others didn't, including myself. I would like to thank these people from the bottom of my heart.

I would also like to thank VIBES.technology team for giving me the opportunity to experience being a part of a startup, and support me with their knowledge and their good vibes for a year. I would also like to thank the chairman of this project, Prof.Dr.Peter Steeneken and (again) my supervisor Dr. Dennis de Klerk for our fruitful meetings, and for their critical questioning which helps me a lot to find my own way on my master thesis.

*Nooshinossadat Mortazavi
Delft, February 2020*

Contents

1	General Introduction	5
1.1	Motivation and research contex	5
1.2	Problem Statement	6
1.3	Research question	6
1.4	Outline of content	7
1.5	Contribution	8
I	part I	11
2	Literature survey	13
2.1	Introduction	13
2.2	Dynamic substructuring (DS)	13
2.2.1	Principal conditions for DS; Interface conditions	14
2.2.2	Component modeling	14
2.3	Experimental dynamic substructuring	16
2.3.1	Component Mode Synthesis (CMS)	17
2.3.2	Experimental modal analysis	18
2.3.3	Assumptions of EDS	18
2.3.4	Practice	19
2.3.5	Challenges and difficulties of DS	20
2.4	Measurements inaccuracies in Experimental DS	21
2.5	Sources of measurements uncertainties in DS	21
2.5.1	Sensors (output of system) as a source of uncertainty	21
2.5.2	Impacts (input of system) as a source of uncertainty	22
2.5.3	Non-linearity	24
2.5.4	Nonphysical measurements	24
2.6	Uncertainty propagation	25
2.6.1	General classification of uncertainties	25
2.6.2	Methods to analyze uncertainty propagation	26
2.6.3	Monte Carlo Simulation	26
2.7	Interface Modeling in DS	26
2.7.1	Discrete interface modelling	27
2.7.2	Virtual Point transformation	28
2.8	Methods for quality indication of VP	30
2.8.1	Decomposition techniques	30
2.8.2	Coherence analysis	31
2.8.3	Reciprocity	32
2.8.4	Driving point passivity	32
2.9	Conclusion of literature survey	33
II	Uncertainty propagation from measurements to Virtual Point (VP)	35
3	Introduction	37
4	Analyzing the problem	39
4.1	Decomposing the problem	39
4.2	Transformation matrices T_u and T_f as an uncertainty amplification factors	40
4.2.1	Setup of transformation matrices T_u and T_f	40
4.2.2	How inaccurate transformation matrices affects the VP's calculation	42
4.2.3	Influence of relative distances and relative directions of all impacts to VP	42

4.3	How uncertainty affects the measured Frequency Response Function	43
4.3.1	Mode and frequency dependency on uncertainty propagation to <i>VP</i> 's FRF	43
4.3.2	Directional uncertainty in measuring equipment	44
5	Methodology	47
5.1	Introduction	47
5.2	Analytical approach	47
5.2.1	Error sensitivity as a function of error direction	48
5.2.2	Effect of impacts direction on the propagation of positional uncertainty	51
5.2.3	FRF's error generation as a function of distance to stand node	52
5.2.4	Uncertainty propagation into <i>VP</i> 's FRF	53
5.2.5	Uncertainty propagation into <i>VP</i> 's FRF, absolute value VS percentage value.	54
5.2.6	Non-linearity and uncertainty propagation to <i>VP</i> 's FRF.	55
5.2.7	Relation of a_x and b_x and their influence on R_{VP}	56
5.2.8	Positional Uncertainty: Mode shape and frequency dependency of error propa- gation into <i>VP</i>	57
5.2.9	Positional uncertainty; Error in the estimation of <i>VP</i> 's forces and responses	58
5.2.10	Directional Uncertainty	60
5.2.11	Propagation of Directional Uncertainty into <i>VP</i>	62
5.3	FEM approach on an asymmetric structure (modal based) model.	68
5.3.1	Tracking the dominant <i>directional error source</i> for each mode shape	69
5.4	Monte Carlo simulation on an asymmetric structure (modal based) model	70
6	Results and Discussion	73
6.1	Results 1: FEM, A Complex Modal Based Model.	73
6.1.1	Measured FRF: Mode shape- and frequency-dependent dominant error sources	74
6.1.2	VP transformation: Mode shape- and frequency-dependency of dominant error source.	77
6.1.3	FRF of least precise <i>vp</i> 's cross-functions	84
6.2	Error cancellation.	86
6.2.1	Effect of symmetrical impacts placement with respect to <i>VP</i>	86
6.2.2	Effect of error's consistency on error cancellation	88
6.2.3	Effect of symmetrical Impacts placement on error cancellation	91
6.3	Results 2: Monte Carlo simulation	94
6.3.1	M.C. results: All cases on Lateral Bending	95
6.3.2	M.C. results: All cases on vertical bending	96
6.3.3	M.C. results: All cases on Torsion	97
6.3.4	Deviation on the admittance, absolute value or percentage	97
6.3.5	Evaluating the correctness of Monte Carlo simulation	99
6.4	Discussion	100
6.4.1	Comparing numerical results of IPU and IDU cases	100
6.4.2	Comparing positional error and directional error on Sensors, numerical results	100
6.4.3	Comparing the PU/DU on sensors and impacts, numerical results	100
6.4.4	Effect of error cancellation on sensors, numerical results	101
6.4.5	Comparing analytical approach and numerical results	101
7	Conclusion	103
7.1	Conclusion	103
7.2	Recommendations	106
	Appendices	109
A	Appendix A	111
B	Comparison of all cases from numerical results	113
C	SDU, Sensors Directional Uncertainty	117
C.1	Case SDU, without error cancellation	117
C.2	Case SDU, effect of error cancellation on sensors	122

D	Effect of Error cancellation, case SDU	125
E	Error propagation in percentage value;case SDU	127
F	IPU; Impacts Positional Uncertainty	129
F.1	IPU, Impacts Positional uncertainty, No Error Cancellation, Non-symmetrical Error direction	129
F.2	IPU, Impacts Positional uncertainty, with Error Cancellation	135
F.2.1	FRF of most sensitive cross-functions for dominant error sources.	141
G	Effect of error cancellation, case IPU	143
H	Case SPU; Sensors Positional Uncertainty	145
I	Transformation matrices	151
	Bibliography	153

Nomenclature

ΔY_{meas}	Deviation on measured admittance from its true value
ΔY_{VP}	Deviation on Virtual Point's Admittance from its true value
Y_{meas}	Measured admittance
Y_{true}	Measured admittance in true configuration
Y_{VP}	Virtual Point's admittance
CI	Confidence Interval
$CMIF$	Complex Mode Indicator Function
CMS	Component Mode Synthesis
$DMSM$	Direction of Mode Shape Motion
DoF	Degree of Freedom
DS	Dynamic Substructuring
EDS	Experimental Dynamic Substructuring
EMA	Experimental Modal Analysis
$EMPC$	Equivalent Multi Point Connection
FBS	Frequency Based Substructuring
FEM	Finite Element Model
FFT	Fast Fourier Transformation
FRF	Frequency Response Function
IDM	Interface Displacement Modes
IDU	Impacts Directional Uncertainty
IFM	Interface Flexibility Matrix
IPU	Impacts Positional Uncertainty
MC	Monte Carlo Simulation
$MDMS$	Movement Direction of the Mode Shape
ODS	Operational Deflection Shape
SDU	Sensors Directional Uncertainty
SPC	Single Point Connection

SPU Sensors Positional Uncertainty

SVD Singular Value Decomposition

SVD – ODS Singular Value Decomposed Operational Deflection Shape

VP Virtual Point

VPT Virtual Point Transformation

General Introduction

This work comprises research in the field of Experimental Dynamics. This technique is currently used in the automotive area and is used to enhance the current state of FEM with the inclusive of test-based models. Building test-based models for EDS (Experimental Dynamic Substructuring) requires very accurate measurement, and this thesis examines how uncertainty on sensors and impacts affects the accuracy of the test-based model.

1.1. Motivation and research context

Dynamic Substructuring (DS) is a widely used tool in industrial applications ranging from automotive and aerospace engineering to the design of wide turbines and high-tech precision machinery. Dynamic Substructuring analyses the dynamic behavior and simulates the mechanical vibrations of the substructures and components of a mechanical system separately. This method does help to calculate the assembled dynamics later using the coupling procedure. Due to improvements in sensor and signal processing technology, substructuring techniques also became attractive for the experimental community.

Dynamic Substructuring is the collection of methods to describe large and complex systems by using the models of its substructures. This approach assumes that the dynamics of each substructure is enclosed in a so-called super element at interface DoF. This means that only the dynamics which are displayed at the interface is of relevance to the substructure assembly. Modeling domains that engage condensed dynamic information, like admittance FRFs in the frequency domain, are therefore particularly suited for substructuring [49].

Compatibility condition and equilibrium condition are two interface conditions which must always be satisfied. Equilibrium condition means having the force equilibrium on the couple point's DoFs of both substructures. Compatibility condition refers to the same displacement of coupling points. The substructures (components) can be modeled by a hand full of analytical equations, by numerical models (FEM) or by experimentally obtained information.

In the field of Experimental Dynamic Substructuring, the subparts are characterized by their experimental behavior. In other words, the experimentally obtained information does describe the subdomain(s) instead of a mathematical description of the domain.

Development in digital data acquisition and the discovery of the Fourier Fast Fourier Transformation (FFT) by Cooley and Tukey in 1965 [12] gave the possibility to do a modal test and (almost) immediately obtain frequency response function (FRFs). These FRFs can be used directly to build an experimental model of the component to characterize the dynamics of the system. This experimental test-based model is potentially as powerful as any numerical model could be employed for purposes like dynamic

substructuring, transient simulation, and transfer path analysis.

There are different methods to model the interface between two (or more) substructures. One of them is coupling two substructure by a single mutual point, so-called Virtual Point. This single point is a *collocated* point, a super-element, which has both *translational* and *rotational* DoFs.

For further substructuring, we need the FRF of the single coupling point of each substructure. We need an experimentally gained information recorded by sensors and roving impacts in order to be able to calculate and build the super-element's admittance (Virtual Point FRF). Then these measured data are transforming into a super-element's admittance for using the projection matrices for both input and output. This process is called Virtual Points Transformation (VPT).

In order to calculate the super-element's admittance (by transforming measured data), the area of measurement must deform rigidly, so we assume the linearity on the measurement area.

1.2. Problem Statement

A carefully performed measurement could help to obtain results with a high accuracy in a multi-kHz range where a numerical model would already fail to produce a reliable result. However, to guarantee for a such high level of accuracy, beside a deep understanding of component's dynamics the measurements have to be done carefully [49].

Two types of errors can be made in a measurement; random errors, and systematic errors [48]. Random errors in DS are signal fluctuations. Most of the time these type of errors are caused by the measurement environment and can be evaluated through statistical analysis. Systematic errors in DS are usually caused by inaccurate sensor and hammer impact positioning, wrong calibration of measurement equipment, constant influence from the environment, leakage, and the mass loading[15].

In all experiments, always we have some uncertainties. For this reason, achieving true experiment is almost impossible. Making errors while mounting the sensors and roving impacts is very plausible. This mounting errors can be **positional** as well as **directional**. In the presence of locational or directional uncertainty the relative distances and relative orientation (between measured places and Virtual Point) do not represent the true value. Any uncertainty in the estimation of the position or the direction of the measured input and output will lead to an inaccurate projection of the measured data into super-element and consequently may affect the estimation of super element's (*VP*) admittance.

1.3. Research question

Voormeeren *et al* [50] have shown that uncertainties in the interface point FRFs (i.g. Virtual Point) cause propagation of uncertainty in all of the FRFs of the assembled system. This arises the importance of having an accurate calculation of Virtual Point FRFs. As the main objective of this thesis I tried to understand:

How uncertainty in the position and direction of the measuring equipment propagates to the (calculated) frequency response function of super-element (so-called Virtual Point *VP*).

We have two choices to deal with the inaccurate estimation of the position and directions of measurement equipment:

- Efforts in order to find a better estimation of position and direction of sensors and impacts, to calculate a more accurate FRF at *VP*.
- Investigate to understand how these uncertainty propagates to *VP*'s FRF calculation and being aware of the consequences of the wrong estimations. This understanding can further give us

abilities to know where to find inaccurate results from the calculations.

In this thesis, I decided to chose the second approach. And, this study is an investigation to analyze how the uncertainty in the position and direction of measuring equipments propagates into the calculation of Virtual Point's FRF, by answering the following questions:

- **Which error at what amount is the most dominant error source?**
- **At which frequencies we can expect the less precisest?**

In this thesis the uncertainties on the measuring equipment are as follow:

- Impacts' Directional (Orientation) Uncertainty (IDU)
- Impacts' Positional Uncertainty (IPU)
- Sensors' Directional (Orientation) Uncertainty (SDU)
- Sensors' Positional Uncertainty (SPU)

1.4. Outline of content

This thesis consists of two main parts: Part. I is a literature survey about the theoretical background on Experimental Dynamic substructuring (EDS), and the sources of measurement uncertainties on EDS are reviewed. Part.II is studying how uncertainties on FRFs measurement propagates to super element (a single coupling point).

Section.2.2 of Part.I (literature review) discusses the Dynamic Substructuring (DS), its advantages, and the ways to model a component. Then the theoretical background on Experimental Dynamic Substructuring (EDS) is presented on section.2.3; such as frequency domains of system dynamics, component mode synthesized (CMS), the assumptions of EDS, the ways of practicing an experiment, and the challenges and difficulties of EDS. Section.2.4 reviews the challenges and difficulties of EDS, such as experimental errors, modal truncation errors, rotational DoFs, time delay. Section.2.5 discusses the sources of measurement uncertainties in EDS, particularly for sensors (output of system), for the input of the system, the effect of non-linearity, and nonphysical measurements. Section.2.6 discussed the classification of uncertainties and the methods to analyze the uncertainty propagation.

Sections.2.7 considers the methods to model the interface in DS and reviews the concept of a single coupling point, a super element, so-called Virtual Point (*VP*). Section.2.8 is a review of the quality indication methods super-element (Virtual Point *VP*). These methods are categorized into four main groups; decomposition techniques, coherency analysis, reciprocity, and driving point passivity.

Part.II focuses on how uncertainty propagates from measurement to a single coupling point's FRF (a super-element, so-called *VP*). These sources of these uncertainties are particularly the position and direction of force and response sensors.

Chapter.4 reviews how super element's (Virtual Point's) FRF is calculated, and how each component of calculation works through computation. Moreover how uncertainty affects the way each component contributes to the computation of *VP*'s FRF.

First, it is shown how the intended uncertainties affect the measured FRF themselves, which is the subject of section.4.3.

Applying an exact amount of positional and directional error (uncertainty) on the sensor and impact in an experiment is challenging, and obtaining the true experiment is almost impossible. For this reason, this study uses simulation to mimics an experiment.

Four types of uncertain scenarios are considered; impacts positional uncertainty (IPU), impacts directional uncertainty (IDU), sensors positional uncertainty (SPU), and sensors directional uncertainty (SDU). Each scenario contains just one type of uncertainty.

In chapter.5 three approaches are investigated, analytical approach, numerical approach, and Monte Carlo simulation. Both numerical simulation and Monte Carlo are applied to a complex finite element model.

In Section.5.2 each scenario is analytically analyzed. Then on Sections.5.3 a complex modal-based model is introduced for numerical approach. Sections.5.4 discussed how Monte Carlo simulation is used to bring random errors on each variable (still for each scenario).

Chapter.6 indicates the results of the numerical approach for case IDU, Impacts Directional Uncertainty. In Section.6.1 the IPU case is simulated on a complex modal-model, for a well-defined amount of error. Then a Monte Carlo simulation is used to bring random errors on each variable (still for each scenario). In the discussion part of chapter.6, the results of simulations are compared with each other and then compared with the expectations from the analytical analysis.

1.5. Contribution

The contribution of this these to the field of Experimental Dynamic Substructuring is as follows:

- **The most dominant error source**

Based on the local mode shape motion of measurement area, and using the Component Mode Synthesized method; expectations can be made on the inputs' or outputs' DOF with dominant effect on error generation for a particular mode shape.

- **Frequencies with less precise expectations**

This thesis shows analytically and confirms with numerical results that the error generation of a particular error (for example, a specific error direction for positional uncertainty in an impact) is mode shape- and frequency-dependent. Moreover, the propagated errors into Virtual Point admittance are also mode shape- and frequency-dependent.

- **The amount of the error propagation caused by dominant error source**

By studying the error generation caused by incorrect and inaccurate transformation operators, we obtain the amount of the influence of each dominant error source on the calculation of the forces and responses of Virtual Point, on both rotational and translational forces and responses. Table.5.2.11 summarizes all the errors on the calculation of forces and responses (for both rotational and directional kind of error).

- **Error Cancellation**

The *direction* of the generated errors on rotational part (rotational responses or moments) is depending on the *sign of error direction*, and on the *sign of the relative distance* of the error source to VP (*sign* of $\delta\theta$ and r_x). Further, the *amount* of generated errors on rotational parts (rotational responses or moments) is depending on the distance of measure point to VP, and the amount of uncertainty.

Altogether, there is a possibility for an error cancellation, where the generated errors with different signs can *cancel* each other.

- **Maximum error generation**

It is numerically shown that if all the generated errors, including dominant ones, have the same direction, then these errors will be added on top of each other, and the maximum error can be generated.

- **Error generation in percentage value:**

In case of directional error, the *portion* of replaced modal value remains constant for a certain amount of directional error. This leads to greater *percentage change on FRF* for measuring point with primary low modal value.

- **Comparing the uncertainty propagation on impacts; IPU VS IDU**

We compared the deviations on the VP's admittance caused by both types of impact's errors,

IPU, and IDU, separately for all types of mode shapes. We observed from numerical results that a directional uncertainty of 5 degrees on impacts may cause higher error generation on the VP 's admittance than a 2 mm positional uncertainty on impacts. This comparison is based on the worst-case scenario when no error cancellation can happen.

- **Comparing the uncertainty propagation, sensors VS impacts**

In the presence of uncertainty on impacts, we are expecting the highest deviations (on absolute value) on the cross-functions on a same *row of admittance*. This(ese) row(s) corresponds to response DoF(s) with the highest response and motion of that particular mode shape.

Further, if a sensor has a mounting error, then we expect to see the most deviations on the cross-functions on the same *columns of admittance*. These columns correspond to force DoF(s) with the highest modal values.

- **Error propagation on higher numbers of each mode shape type**

An analysis is done to find the relation between the distance of measure point (and VP) to the stand node. The numerical results also confirms that; smaller the distance between the measuring point (and VP) to stand node, the higher the error propagation into VP 's admittance. In other words, higher the number of a certain type of mode shape, higher the error generation and propagation.



part I

2

Literature survey

2.1. Introduction

This chapter is reviewing the literature regarding the Dynamic Substructuring, Experimental Substructuring, error sources of an experiment and the effect of each error on the measured data.

In section.2.2 the Dynamic Substructuring (DS), its advantages and the ways to model a component is discussed. Section.2.3 reviews the theoretical background on Experimental Dynamic Substructuring (EDS); such as different domains of system dynamics (particularly the frequency domain), component mode synthesised (CMS), the crucial assumptions of EDS, and the possible ways to operate a measurement. Then on Section.2.3.5 the challenges and difficulties of EDS is discussed; such as experimental errors, modal truncation errors, rotational DoFs, time delay.

Section.2.5 the sources of the measurements inaccuracies in EDS is obtained. These sources categorized into four groups, accelerometers as error source, force sensors as error source, nonlinearity and nonphysical measurement. Each category discussed the possible kind of errors it can generates.

Section.2.7 considers the possible ways of modeling the interface, and explains the concept of a single coupling point so called *Virtual Point*. Since the goal of this thesis is to understand how measurements errors propagation into a single coupling point (the *Virtual Point*), the transformation (from measurement into single couple point, *VP*) is discussed in details.

Section.2.8 reviews the methods to indicate the quality of Virtual Point. These methods are categorized into four type of techniques; decomposition techniques, coherency analysis, reciprocity and the driving point passivity.

At the end, based on the literature survey the scope of this thesis is clarified.

2.2. Dynamic substructuring (DS)

Dynamic sub-structuring techniques is decomposing the system domain into sub-domains [26]. These subdomains are simpler to analyse dynamic context these sub-domains are called substructures. One of the very strengths of dynamic substructuring is the ability to predict structural-dynamic behaviour of the assembly based on the dynamics of its components. For dynamics modeling, the reduction of the substructures complexity will lead to increase the efficiency.

Advantages of DS

Performing the dynamic substructuring analysis has some important **advantages** over global methods

[26]:

- It gives the ability to evaluate the dynamic behaviour (both numerically and experimentally) of very large and/or complex structures as a whole.
- Identifying the local problems (and operating local optimization in case of numerical domains) due to easier analyzing the local dynamic behavior rather than the entire system. Also, the capability to eliminate the local subsystem that have no significant impact on assembled system may cause a reduction on analysis time.
- It allows combining analytically modeled parts with experimentally identifying components, enabling a hybrid modelling approach.
- Ability to Share and combine substructures from different projects or departments.

2.2.1. Principal conditions for DS; Interface conditions

Dynamic substructuring is the collection of methods to describe large/complex systems by using the models of its substructures. This approach assumes that the dynamics of each substructure is enclosed in a so called super element at interface DoF. This means that only the dynamics that are displayed at the interface are of relevance to the substructure assembly. Modeling domains that engage condensed dynamic information like admittance FRFs in the frequency domain, are therefore particularly suited for substructuring [49].

As the dynamics of the interface is relevant for the assembly, it's crucial that the DoFs at the interface represent the same motion for both connecting substructures. To have the same motion at the connection points (interface) between two or more substructures, two **interface conditions** must always be satisfied:

- **Compatibility condition** at matching pairs of DoFs; which means the displacement of each interface DoF of each substructure must have the same value and sign as its pair on the other substructure. However, in practice the coupling between the subsystems can be modeled as:
 - **exact joint** in which the displacement of both sides are exactly the same.
 - **linear flexible joint** in which one introduces a stiffness representing the coupling stiffness between the coupling DoFs of both components. This stiffness matrix is added during the coupling procedure. This matrix can include some frequency independent elements in the case of a frequency-dependent flexible joint [13].
Also efforts are made to develop nonlinear models to account for a nonlinear behaviors [23].
- **Equilibrium condition** at interface: means a force equilibrium between matching interface DoFs must be satisfied.

2.2.2. Component modeling

Analytical modeling

The mechanical behaviour of a component can be modeled by a handful of **analytical equations**. As these equations require some degree of continuity, a lot of simplifications are needed to model a structure in a primitive system like masses-springs and beams. The task of analytical modelling involves a process of conceptual steps to get from the actual structure to an analytical description to understand just a few degrees of freedom [49]. Analytical solutions are limited to relatively simple cases.

Numerical Modeling

Another approach to analyze a structure's behavior is the Finite Element Method (FEM), which is actually a **numerical method** for solving differential equations generated by theories of mechanics such as elasticity theory and strength of material. To solve the problem, it subdivides a large system of equations into smaller, simpler parts that are called finite elements. The simple equations that model these finite elements are then assembled into a larger and more complex system of equations that models

the entire problem. Then FEM uses calculus variational methods (using small changes in functions and functionals to find the maxima and minima of functionals) to approximate a solution by minimizing as associated error function [30].

In some engineering areas like automotive and air space the numerical modeling is very adequate to model structures with homogeneous material properties. However in modeling the parts with different materials, mechatronic components and in the interaction between parts (connected by welds, bolts or adhesion), the numerical approach shows its limitations. Also, in practice, lots of internal mechanism are not taking in account during the numerical analysis due to their complex geometry and kinematics, however they do contribute to the global dynamics in a very complicated way [49].

Experimental Modeling

In the Experimental Dynamic Substructuring the subparts are characterized by their experimental behavior. In other words the subdomain(s) are described by using the experimentally obtained information instead of mathematical description of the domains.

Development in digital data acquisition and the discovery of the Fourier Fast Fourier Transformation (FFT) by Cooley and Tukey in 1965 [12] gave the possibility to do a modal test and (almost) immediately obtain frequency response function (FRFs). These FRFs can be used directly to build an experimental model of the component to characterize the dynamics of the system. This experimental test based model is potentially as powerful as any numerical model, and can be employed for purposes like dynamic substructuring, transient simulation and transfer path analysis.

In fact, if the experimental measurements are carefully performed, accurate results could be obtained in multi-kHz range where a numerical model would already fail to produce reliable result. However, to guarantee for a such a level of accuracy, the measurements need to be done carefully, and with deep understanding of the component's dynamics [49].

2.3. Experimental dynamic substructuring

The experimental sub-structuring uses the experimentally obtained information to describes subdomain(s).

Domains of system dynamics

Structural dynamic are commonly modelled in five different domains [49] and can be derived from either numerical modeling or experimental testing;

- physical
- modal
- frequency
- time
- state-space

The main focus of this study will stay on frequency and modal domain.

Considering a discrete dynamic system, the second order differential equilibrium can be written between inertia, viscous damping, elasticity and the external applied force

$$\mathbf{M}\ddot{\mathbf{u}}(t) + \mathbf{C}\dot{\mathbf{u}}(t) + \mathbf{K}\mathbf{u}(t) = \mathbf{f}(t) \quad (2.1)$$

Where \mathbf{M} , \mathbf{C} and \mathbf{K} represent the linearized system matrices for respectively mass, damping and stiffness. \mathbf{u} and \mathbf{f} are respectively the displacement and external applied force for all n degree of freedom (DoFs).

Frequency domain

In the frequency domain representation, one assumes a synchronous response to an harmonic load, such that the *time-dependency* of the coordinates and loads can be replaced by *frequency-dependency*. By applying the Fourier transformation on the coordinates and force vector, we can convert the dynamic equilibrium of Eq.2.1 as a function of excitation frequency ω . By knowing that $\dot{\mathbf{u}} = j\omega\mathbf{u}$ and $\ddot{\mathbf{u}} = -\omega^2\mathbf{u}$, the terms on the left hand side can be gathered, Eq.2.2, and calling it $\mathbf{Y}(\omega)$, Eq.2.3.

$$\begin{aligned} \mathbf{M}\ddot{\mathbf{u}}(\omega) + \mathbf{C}\dot{\mathbf{u}}(\omega) + \mathbf{K}\mathbf{u}(\omega) &= \mathbf{f}(\omega) \\ [-\mathbf{M}(\omega^2) + j\omega\mathbf{C}(\omega) + \mathbf{K}]\mathbf{u}(\omega) &= \mathbf{f}(\omega) \end{aligned} \quad (2.2)$$

$$\mathbf{Y}(\omega) = \frac{\mathbf{f}(\omega)}{\mathbf{u}(\omega)} \quad \text{with} \quad \mathbf{Y}(\omega) = [\mathbf{M}(-\omega^2) + j\omega\mathbf{C}(\omega) + \mathbf{K}] \quad (2.3)$$

$\mathbf{Y}(\omega)$ is called *receptance*, or in general *admittance* matrix which is a complex-valued frequency-dependent function, yields a clear interpretation of a structure's dynamic behaviour. The elements of $\mathbf{Y}(\omega)$ are also called Frequency response functions (FRFs) and describe the displacement response as a result of a unit force. The column of $\mathbf{Y}(\omega)$ governs the global response of all DoFs as a result of an excitation at one particular DoF.

Modal domain

According to wave theory, for a dynamic system, a mode is a standing wave state of excitation, in which all the component of the system will be affected sinusoidally under a specific fixed frequency. Because no real system can perfectly fit under the standing wave framework, the mode concept is taken as a general characterization of specific states of oscillation. It means treating the dynamical system in a linear fashion in which **linear superposition of states** can be performed [7].

So, the most general motion of the system is the superposition of its **normal modes**. The modes are normal in the sense they can move independently, and therefore an excitation of one mode will never cause excitation of a different mode. In mathematical terms, normal modes are orthogonal to each other.

Modes(or resonances) are the inherent properties of a structure, and are determined by the material properties (like mass, stiffness properties) and boundary conditions of the structure. Each mode is defined by natural frequencies, modal damping (added to incorporate some damping effect) and mode shape.

Modes are used as a simple and efficient means of characterizing resonant vibration. The majority of the structures are resonant in behaviour. Resonant vibration is caused by the interaction between the inertia and elastic properties of the material within the structure [46]. To better understand any structural vibration problem, the resonances of the structure need to be identified and quantified. Finding modal parameters of the structure is a common way to doing this.

From all the modes of a dynamical system, the normal mode or the dominant mode of a system will be the mode storing the minimum amount of energy for a given amplitude of the modal variable. Or equivalently, for a given stored amount of energy, will be the mode imposing the maximum amplitude of the modal variable.

For linear and proportionally-damped structure, normal modes or eigenmodes are vibration shapes at a fixed frequency for which (in the absence of damping) the inertia forces are in harmony with the elastic force. The eigenmodes ϕ_r and their corresponding eigenfrequencies ω_r can be calculated by solving the:

$$(K - \omega_r^2 M)\phi_r = 0 \quad r = 1, \dots, n \quad (2.4)$$

Where r is the number of mode shapes, and n is the number of DoFs. Typically the eigenmodes ϕ_n^r of each mode r are stored in the columns of a modeshape matrix Φ . The subscript r shows the mode shape number and superscript n denotes the DoF's number.

$$\Phi = \phi_r^n = \begin{bmatrix} \phi_1^1 & \phi_2^1 & \phi_3^1 & \dots & \phi_r^1 \\ \phi_1^2 & \phi_2^2 & \phi_3^2 & \dots & \phi_r^2 \\ \vdots & \vdots & \vdots & \dots & \vdots \\ \phi_1^n & \phi_2^n & \phi_3^n & \dots & \phi_r^n \end{bmatrix} \quad (2.5)$$

Modes are further characterize as their **rigid body modes** or **flexible body modes**. The rigid body modes are the modes for which the solution of Eq.2.4 is $\omega_r = 0$. All structures can have up to 6 rigid body modes, three translational modes and three rotational modes.

2.3.1. Component Mode Synthesis (CMS)

As the modes with lowest eigenfrequency are in general the most accurate in an FE model and relevant to typical dynamic analysis, we can limit the full displacement field \mathbf{U} a subspace of size m , where m are the number of first natural modes ($m \ll n$ in successive order). As a consequence the modeshape matrix will be reduced to the reduced modeshape matrix $\mathbf{R} = [\phi_1, \dots, \phi_m]$, which can extremely reduce the effective dimension of the original problem [26] [49]. It is good practice to include eigenfrequencies up to twice the highest frequency of interest in summation [49].

The admittance FRFs can then be synthesised using a superposition of single-DoF modal solutions. The rigid body modes (if present) need to be treated differently as they have an eigenfrequency $\omega_r = 0$ and no damping ratio related to frequency. The superposition for admittance, i.g. displacement at DoF(i) over force at DoF(j) reads as follow:

$$Y_{ij}(\omega) \approx -\frac{1}{\omega^2} \sum_{m_{RB}}^1 \phi_r^i \phi_r^{jT} + \sum_{m_{RB}+1}^m \frac{\phi_r^i \phi_r^{jT}}{-\omega^2 + 2j\omega\zeta_r\omega_r + \omega_r^2}$$

$\underbrace{\hspace{10em}}_{\text{rigid body modes}}$

$\underbrace{\hspace{10em}}_{\text{vibration modes}}$

The nominator only comprises the spatial or modal part of the response which remains constant over frequency. The denominator controls the spectral part, adding a resonance frequency for each mode r , namely for $\omega = \omega_r$.

Note that FRFs for velocities or accelerations are obtained by multiplication of $Y(\omega)$ with $j\omega$ and $-\omega^2$, respectively.

2.3.2. Experimental modal analysis

The admittance FRFs can be obtained from experimental testing, and directly used in frequency based substructuring or for experimental modal analysis (EMA). The goal of Experimental modal analysis is identifying the vibration modes from measured response data, resulting in the series of mode shapes with associated frequency and damping parameters, which are called modal parameter estimation and can be understood as the inverse action of mode synthesis.

The Experimental modal analysis is a system identification techniques. The system is a 'black box' that needs to be decoded. The traditional approach is to provide the 'black box' with a known input, measure the output and continue with the identification. For the measurement the force is used as an input so that the frequency response function can be derived from the force and response information. frequency response functions, FRFs, is a frequency domain representation of a system's dynamic characteristics. The excitation force can be random, sinusoidal, periodic, or impacts ones. Theoretically, the type of force does not matter as FRF is the ratio between the response and force. The force must have sufficient energy and frequency component to to excite all vibration modes of interest [19].

2.3.3. Assumptions of EDS

Linearity of the tested structure is one of the essential assumption to achieve accurate FRF measurements. To prove the linearity of the structure, we should be able to control the force level, then we multiple the force input level and observe the repeatability of the FRF data. If the linearity assumption does not follow exactly, the normal modal analysis from the measured FRF data may only represent a linearized mathematical model for the structure.

Reciprocity property of the structure is other essential assumption. This assumption is also not difficult to verify.

Time-invariant structure is required to succeed the FRF measurements. Time-invariant structure means that the dynamic properties of a structure does not vary during the measurements.

A modal analysis on a subsystem might not always be possible as the substructure might have

- too high damping
- frequency dependent dynamic stiffness
- too high modal density

In such a cases, direct coupling with the measured FRF data is the best option, as the residual terms are naturally included in the data [26]. For more information about direct coupling see [26].

2.3.4. Practice

For obtaining the test based experimental model and study the dynamics of a substructure in the frequency domain an admittance measurements needs to be done. This measurements include measuring the vibration of a substructure when it is excited (by hammer or shaker). Modern day experimental dynamic substructuring systems are composed of 1) sensors, 2) data acquisition system, and 3) a host PC to view data and analyze it.

The frequency response function, **FRF**, is a fundamental measurement to characterize the dynamics of the system. The FRF describes the input-output relation between two point as a function of frequency range. A FRF is a measures how much displacement, velocity or acceleration response a structure has at an output DoF, per unit of excitation force at an input DoF. FRF is the ratio of the Fourier transformation of an output response $X(\omega)$, divided by the Fourier transformation of the input force $F(\omega)$ that caused the output.

The structural dynamic measurements involves measuring the elements of FRF matrix for the structure. This model represents the dynamics of the structure between all pairs of input and output DoFs. FRF matrix columns correspond to input, and rows correspond to outputs.

The classical approach is single-input,multiple-output (SIMO), which is one excitation point and measuring the resonance at many different points. It's also possible to fix an accelerometer and excite the (sub)structure with a hammer in many positions, which called multiple-input,single-output (MISO). Mathematically, due to the principle of reciprocity the MISO and SIMO are identical. Reciprocity is discussed on section ?? . Recently multi-input,multi-output is becoming more practical, as by using partial coherence analysis, which gives a possibility to observe which part of resonance comes from which excitation source.

Sensors

The use of triaxial accelerometers has become standard practice in experimental testing [4]. Triaxial accelerometers are piezoelectric accelerometers which are converting the mechanical motion into an electrical signal. Piezosensitive accelerometers are preferred in high shock applications. In the capacitive accelerometers the silicon micro-machined is the sensing element, and their performance is superior in the low frequency range. In the field of dynamic substructuring the triaxial sensors are mostly used. In Section 2.5.1 the limitations and challenges of using accelerometers are discussed.

Excitation Tool

Typical tools to excite a (sub)structure for vibration analysis are a shaker or impact hammer.

Impact hammer is a hammer with a load cell and a variable tip, to excite and measure impact forces on structures. It excites the structure by a short impulse, which mimics an impulse response, creating excitation energy well distributed for a large frequency band. The load cell on the tip of the hammer measures the stimulus force.

A variety of tips supplied with each hammer permit the energy content of the force impulse to be tailored to suit the requirements of the item under test. The tip of the hammer determines the impulse shape (both amplitude and duration) and the bandwidth of excitation. In Section 2.5.1 the limitations and challenges of using hammer impacts are discussed.

Shakers are the voice coils where a thin stick is attached, called the stringer. Stringer is connected to the structure with a force gauge, and excites the structure in for frequency of interest. In the case of shaker, using a single shaker may not effectively excite all the modes of the (sub)structure, where multiple shakers distribute the energy to the system in more uniform way over the (sub)structure [6].

2.3.5. Challenges and difficulties of DS

Like all methods, effective and reliable use of Dynamic substructuring requires a solid understanding of its limitations. Experimental DS is highly sensitive to the experimental errors and the origin of all experimental DS analysis errors lies on the inability to properly measure [49]. The list of main difficulties in DS are as follows [26]:

- **Experimental Errors**

- Challenges regarding **sensors**: sensor placement, cross-axial error, mass loading, low frequency accuracy
- Challenges regarding **impact hammer**: Accuracy to placement, force dependency, choice of hammer tip, local flexibility, energy limit, double pulse

- **Modal truncation errors** means that not all the modal degrees of freedom, describing the subsystem's dynamics, are contained in the subsystem's description. If a subsystem is identified with Experimental Modal Analysis (EMA) and is afterwards used in DS calculation the inclusion of for example residual flexibility is essential. If the residual flexibility is not included, the substructure will behave more stiff as it has less degrees of freedom to deform in [21] and a shift in resonance frequency of the total coupled system can be expected [26].

- **Rotational degree of freedoms** are very important in the mobility coupling application, and their absence in the formulation causes faulty predictions [17]. In [29] the importance of the RDoFs FRFs of each substructure on the coupled system is discussed by looking to the generated error in the "coupled system". The study suggests to look at the significance of each RDoF in the FRF coupling analysis.

In the higher frequency range, the rotational motions are bigger than the translational ones [17]. The measurements of structures at joints have to be carefully made in order to avoid errors at these coordinates. The RDoFs are normally neglected in experimental modal analysis due to their difficulty to measure [17]. In practice, the measurements of these rotations and the application of torque to excite them is very difficult. The influence of neglected rotational information strongly depends on the component's interface flexibility [10]. Different approaches exist to tackle the RDoF issues [26]:

- measuring RDoFs
- expand translational data to reconstruct the RDoF information [41] [38]
- If the interface has only local rigid body motions, the response of the interface can be constructed from a minimum of six coupling DoF at three nodes [26]. This leads to good results up to a frequency where local deformation between the interface nodes starts to take place.

- **Interface modeling** is a challenge in DS, as in fact the interface is a continuous surface, and the measurements can usually be performed on a small discrete number of points.

- **Rigid body modes** information is the essential to successfully couple the structures with component modal synthesis method [39]. A modal identification procedure is required to extract all the modal properties of the available rigid body modes.

The main difficulty associated with these methods is that not all the rigid body modes can be simultaneously excited during an experimental test [5].

- Dynamics of joints can cause a nonlinear coupling mechanism

- **Time delay** is a bottleneck of real-time DS which is caused by the inherent dynamics of actuators used for structural testing [22]. The time delay can cause instability during the experiment. In real-time DS, a hybrid model of the complete system can be created, by combining the experimental substructure with numerical substructure. This technique is useful when dealing with nonlinear structures. The nonlinear dynamic behavior can be extracted experimentally by including the substructure in the real-time substructuring loop [26].

The main focus of the present study is to **identify the measurement errors, their exact sources and how they propagate during modal analysis**, which is going to be discussed broadly in the coming chapters and sections.

Further treatment of other uncertainty sources and their influence on measurements is out of the scope of this study.

2.4. Measurements inaccuracies in Experimental DS

Experimental modeling has some advantages over numerical modeling. But it requires a very accurate measurement. In experimental dynamic substructuring the origin of all analysis errors lies on the inability to properly measurement [49].

To study the measurements inaccuracies in experimental DS, first the sources of measurement uncertainties in DS are analyzed. Section 2.5.1 and 2.5.2 reviews respectively the how impacts and sensors can be a sources of uncertainty. Section 2.5.3 examines how non-linearity can cause errors during measurements. Section 2.5.4 consider cases where measured data has no physical interpretation. Section 2.6.1 reviews the uncertainties classification and introduces methods to analyze the uncertainty propagation.

2.5. Sources of measurements uncertainties in DS

Errors in FRF measurements and in the modal parameters extracted from them can arise from a number of sources, and this can have a dramatic effect on dynamic substructuring predictions. Allen et al [2] reviewed the uncertainty in experimental/analytical substructuring predictions from litterateurs, and categorize them in a few subcategories:

- measurements inconsistencies
- Cross-axis errors
- non physical measurements.

In this thesis the same categories are adapted and analyzed what kind of uncertainty they can generate.

In this section impacts and sensors are consider as the uncertainty sources and discussing the type of uncertainty they can produce.

2.5.1. Sensors (output of system) as a source of uncertainty

Cross-axis sensitivity

The piezoelectric accelerometer sensors that are most frequently used for modal test are known to register vibrations from other directions than the intended one, a phenomena called cross-axis sensitivity [2].

Similarly, there is always uncertainty regarding the **direction of the input** applied to the structure, which results to overestimating the response of the structure [2].

Cross-axis error can have an important effect on the substructuring prediction. In [32] and [3] the cross-axis errors are thought to be responsible for artificially high level of axial motion in the bending response of a simple beam.

Nicgorski and Avitabile introduce a method called VIKING (Variability Improvement of Key Inaccurate Node Groups) to use the measurements to tune an approximate FEM model for the substructure to eliminate cross-axis error.

Sensors Mass loading

As the sensors have mass, they influence the measurements. Rixen [45] shows the sensor mass loading results in spurious peaks in the DS analysis where the location of these peaks depend on where

the sensor is placed on the structure. Their suggestion is to handle the sensors as substructures that are coupled to substructure during measurements and decouple them afterwards.

Sensors accuracy on low frequency

The triaxial sensors data sheets typically claim they can sense the motion from 1 Hz upward for ICD sensors with typical sensitivity 100mVg^{-1} or 10mVg^{-1} , and a 50 g peak. While this range of frequency is acceptable, the noise level can be too high and the gain seems to be affected in impact testing [37].

Adhesion material

Sensors are mostly glued to the substructure. The adhesion material has also an influence on sensor measurement. Adhesion material with high energy absorption can lead to unreliable measurements. The rigidity of the adhesion between the sensor and structure have an influence on the accuracy of the sensor on high frequencies; a stiff adhesive creates a better read out of high frequency. Experimental results of Qnig *etal* [44] revealed that an increase in adhesive thickness alters the electromechanical impedance and the resonant frequency of the piezoelectric elements as well as the amplitude of the sensor signal.

2.5.2. Impacts (input of system) as a source of uncertainty

The study of Brown *etal* [8] discussed the possible errors generated by impacts during impacts testing, which are double(multiple) impacts, overloading, impact hammer calibration, force and response window, force input location and direction or direction, reducing external noise and nonlinear effect.

1. Averaging

In the roving 'hammer test', where the sensors are fixed on the structure and a hammer hits the structure in different places, every impact hits the structure slightly different. This inconsistency leads to slightly different Frequency Response Functions (FRF). In practice it is common to take an average of multiple impacts that have high coherence with respect to each other. In averaging one do not look to the correctness of the impacts, but look to consistency of them, which is debatable if the averaging processes yields to the true FRF.

2. Improper Excitation during measurement

(a) Accuracy on Impacts positioning (direction and orientation)

Inaccuracy in the location or the direction of force input is caused by the users laps of attention or experience or extreme difficulty of access to a particular input location. Different authors looked into the effect of variation on the impacts location on the FRF [31] [8] [14]. de Klerk [14] studied the effect of the small errors in the orientation and location of the impacts hammer during a roving hammer test, and showed a very small error can have an important effect on FBS prediction.

In [14] the **impacts location** were changed, and the offset on anti-resonances was observed. In [8] they show an error on **impacts location** on just one impact causes dramatic effect on coherency between the impacts in frequency range. The reduction in coherence is more visible at anti-resonances.

In [49] the author looked into the slight random error on all **impacts orientation**, and changes in the coherency between them. The calculated coherence for this study is not a direct coherence, while the impacts are first projected to a so called Virtual Point and then project back to the original point, and then compare these (so called filtered) with the ones before any projection. More details of this coherence analyses can be found on 2.8.2.

(b) Overload

Overload happens when too high energy is put to the structure. The overloads are causing distortion errors in measured FRFs in most digital data acquisition systems [8]. Figure.2.1 shows the differences at antiresonance of both phase and magnitude. Point B shows the phase loss instead of phase gain due to overloading.

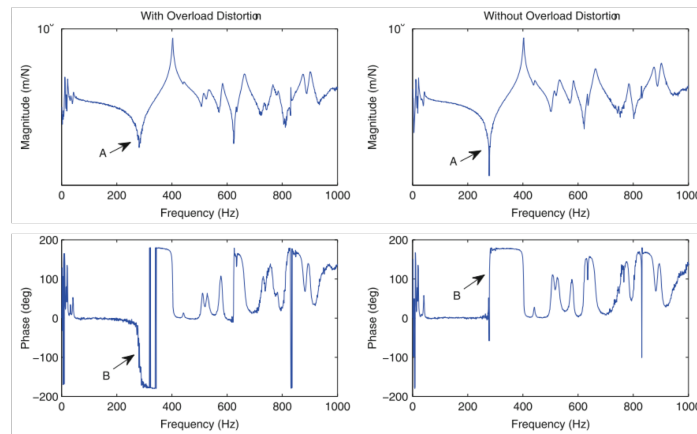


Figure 2.1: FRF measurements exhibiting overload distortion, adopted from [8]

(c) **Too little energy**

The structure needs to excite by enough energy to reach the response at higher frequencies. If the hammer impulse does not hit with proper energy, the resulted FRF is not reliable.

(d) **Double or multiple Hits**

The double or multiple impacts are visible as both magnitude and phase distortions in the frequency domain. By using a force window we can maybe eliminate the second impulse from the measured data, but not the actual energy that is applied to the structure and not from the response signal [8]. For these reasons the resulting FRF is unreliable.

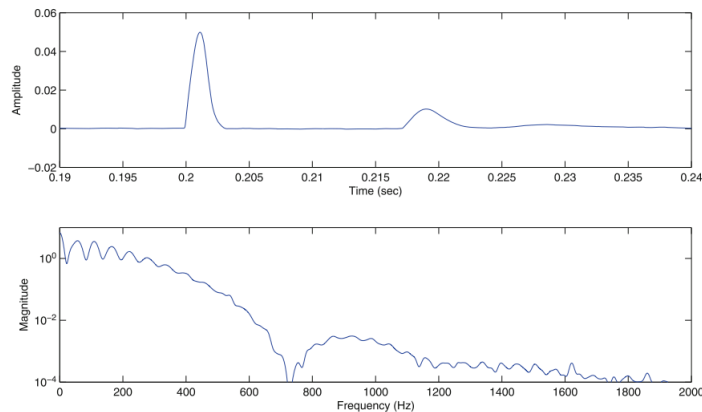


Figure 2.2: force spectrum to double impact, adopted from [8]

3. Hammer tip

The correct tip of hammer will ensure structure get enough energy to excite all the modes of structure. In [31] authors show the effect of different impact tips on the frequency response function (FRF), Figure.2.3. The same study shows a soft tip, like a rubber hammer tip, can not excite all the modes of interest. Reasoning is the same as the locally deformation of structure; the pulse duration is too long which leads to reduction on the usable frequency range of the input spectrum. In contrast, the iron hammer tip has a shorter duration of impulse Figure.2.3 which has higher frequency content Figure.2.4.

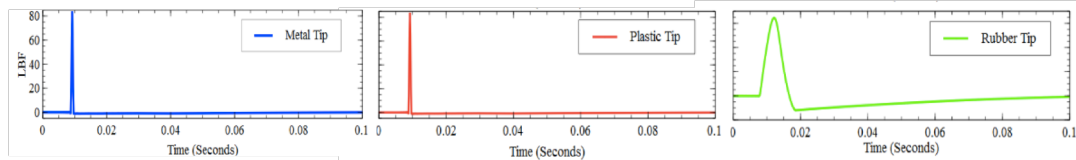


Figure 2.3: Force pulse with the different impact tips on the impact hammer, adopted from [31]

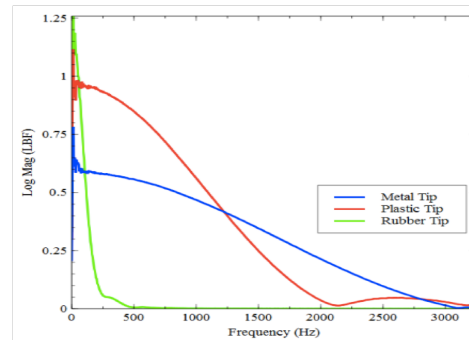


Figure 2.4: Force spectrum with different impact tips on the impact hammer, adopted from [31]

Impacts calibration

As mentioned impact hammers involved a load cell that is assembled in the head of the hammer. The force measured by the load cell is not the same as the external force acting on the tip of the hammer during impact. Therefore impacts needs to be calibrated. The incorrect calibration leads to incorrect data recording.

2.5.3. Non-linearity

- **Local deformation and flexibility of structure**

Hitting the flexible part of the structure results in a local and large deformation in that area, which leads to local absorption of the impact energy. This large deformation effectively lengthens the duration of the impact, thereby reducing the usable frequency range of the input spectrum. In this case it's not anymore possible to put energy to the structure to reach the higher frequencies and as a consequence the bad FRF estimation [9].

- **Non-linearity in joints**

An impact is not a practical excitation for characterizing non-linearity's because the force level can not be precisely controlled for every impact [9].

Segalman [47] and Allen *etal* [1] have shown if there is a small non-linearity, for example due to bolted joints, on each loading a microscopically slip may happen which leads to having a shift on natural frequency from one experiment to the next.

2.5.4. Nonphysical measurements

Sometimes errors in FRF measurements can be detected when they cause FRFs that exhibit phenomena which are not possible for physical systems [2].

1. **Negative imaginary value at driving point**

since the mode shapes appears as squared quantities at drive point, at driving point the imaginary part of the accelerance response must always be positive. Carne and Dohram [11] found the spurious peaks can appear in substructuring prediction if this feature is violated, and introduce a technique called Decomposition Data filtering (DCD) to address it. This method found to be successful to remove some spurious peaks from FBS predictions for a quite complicated system.

2. Negative Mass after Substructure Uncoupling

Kanda et al. [25] found that the mass matrix sometimes is not positive definite after uncoupling and removing a mass from a substructure, in the modal domain. The same authors in [3] and [32] observe the negative mass matrix when substructuring one flexible structure from another. They point this non-physical result as an errors in the modal scale factors and adjusted them with experimentally determined value until the mass matrix became positive definite as expected.

2.6. Uncertainty propagation

Voormeeren, de Klerk and Rixen show on [15] and [50] how the uncertainties in each substructure FRF propagate to the (built-up) structure assembly, here they use the linear term in Tylor series expansion of the substructure equation. In [50] they found the uncertainty on the connection point FRF produces uncertainty in all elements of FRF of assembled system, while uncertainties on points away from connection point do not affect by the FRF of the assembled system.

Considering the frequency based substructuring approach, at each frequency the FRFs of the coupled system are computed from the FRFs of the subcomponents at the same frequency, so those regions of the frequency band may become resonances of the built-up structure, greatly amplifying measurement errors [2].

The study of Imregun, Robb and Ewins from 1987 [24] for the FBS method (frequency based substructuring method), shows that very large errors might exist in coupled system predictions due to relatively small (5%) errors in the subcomponent FRFs.

Yang, Adams et al. [51] introduce the **Embedded Sensitivity approach**, which is based on linear approximation for the FRF sensitivity. Under mild assumption one can compute the sensitivity of FRF to small mass or stiffness modification, using the measured FRF alone. It is called embedded because it is the explicit structure properties like mass, stiffness and damping are not required. They introduce a formula for numerical model to calculate the changes in frequency response function (FRF) when a small mass δm is added to the system on a certain node. As this method considers the problem linearly, it can be used just for small modification, where non-linearity is absence. For more detail see [51].

This section reviews the general classification of uncertainty. Section 2.6.2 studies the Methods to analyze uncertainty propagation by categorizing them as Non-probabilistic and probabilistic methods and further sub-categorizing them to statistical probabilistic methods and analytical probabilistic methods. In Section 2.6.3 the Monte Carlo simulation and the evaluation of correctness of that is reviewed.

2.6.1. General classification of uncertainties

During a measurement two kind of errors can be made, random errors and systematic errors [48]:

1. **Random errors** are always present in measurements. Random errors in experimental measurements are caused by unknown and unpredictable changes in the experiment. These changes may occur in the measuring instruments or in the environmental condition. Random errors have often Gaussian distribution, and in such a case the statistical methods may be used to analyze the data. The mean m of a number of measurements of the same quantity is the best estimate and that quantity, and the standard deviation s of the measurements indicates the estimation validation.

Random errors are errors in measurements that lead to values being inconsistent when repeated. Random errors in DS are signal fluctuations, which are most of the time caused by the measurement environment and can be evaluated through statistical analysis. In general, random errors are due to factors that cannot be controlled.

2. **Systematic or bias errors** are errors that are not determined by chance but are introduced by an inaccuracy (involving either the observation or measurement process) inherent to the system [33]. Examples of bias errors in experimental DS are errors in the **positioning and the direction of**

sensors and hammer impacts, imperfect **calibration** of measurement equipment's, **constant environmental influences**, **leakage**, **neglecting rotational DoF**, **mass loading**, **unmeasured side forces in the shaker's excitation** [15]. The difficulty of systematic errors is that they are not observable and can't be removed from the system.

2.6.2. Methods to analyze uncertainty propagation

Different approaches exist to investigate the uncertainty propagation from a number of inputs to an output. In general, they can be classified according to [18]:

- **Non-probabilistic methods** are used when little is known about the input variables. A non-probabilistic approach is usually based on an interval analysis.
- **Probabilistic methods** can be used when the probability distributions of the input variables are known, hence regarding them as stochastic variables. Two types of probabilistic methods exist:
 - **Statistical probabilistic approaches**
use a large number of random input values and calculate repeatedly the output values. Statistical properties of the output are thereafter calculated. The classic example of such a method is the Monte Carlo simulation [34].
 - **Analytical probabilistic approaches**
Take an analytical approach to determine the uncertainty of the output variables based on the input uncertainties. Examples are the 'moment' and 'stochastic differential equation' methods [40].

2.6.3. Monte Carlo Simulation

One of the most straightforward way to study the effect of uncertainty is through Monte Carlo Simulation. In physical-related problems Monte Carlo methods is used for solving the problems with many coupled degree of freedom. Monte Carlo is also used for modeling and predicting a system or phenomena with significant uncertain inputs [43].

This method use different random values for the uncertain system parameters to repeating the sub-structure predictions. Then, the statistics can be performed on response and robustly quantify the effect of the built up system's response.

The characteristic of high quality Monte Carlo simulation are listed by Sawilowsky [27] and are as follow

- There are enough samples to ensure the accurate results
- The proper sampling technique is used
- The algorithm used is proper for what is being modeled
- The (pseudo-random) random value generator pass the tests for randomness
- The (pseudo-random) number generator has certain characteristics (e.g., a long "period" before the sequence repeats)

2.7. Interface Modeling in DS

This section considers briefly the discrete and continuous interface, then reviews two discrete methods to model the interface, EMPC and Virtual Point. In Section ?? we consider the Virtual Point transformation by looking to displacement and force reduction of the interface. In Section ?? different methods for quality indication of the *Virtual Point Transformation* are considered.

In general there are two categories of connectivity between substructures:

- **Discrete connection nodes**, where the connection points behave rigidly in the area near the interface. Up to a certain frequency these nodes permitted to displace with respect to each other

which allows the significant deformation in the structure. In discretized interfaces the deformation on connecting points are very small and do not contribute to the coupled vibration, see Figure.2.5(a).

- **Continuous line or surface interface**, where the deformation of the interface is strongly coupled to the internal vibration of structure and can not be discretized to a small number of nodes, Figure.2.5(b).

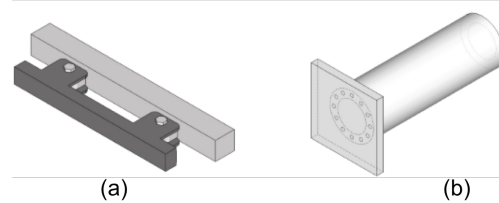


Figure 2.5: Substructure connectivity, (a) discrete interface points, (b) continuous interface surface, Adopted from [49]

2.7.1. Discrete interface modelling

The interface can be considered in different ways. Figure(2.6a) shows the continuous interaction in a bolted connection as the result of friction caused by pretension. Figure(2.6b) considers the same connection in case of using FEM model, a discrete coupling with coinciding nodes. In this case by coupling a sufficient number of nodes over a large area, any rotational coupling is implicitly accounted for.

One way to experimentally model the connection is considering the connection as **some single points (SPC)**. For doing that some measurement points need to be chosen, as close as possible to the connection point and mount the sensors at those places (e.g. triaxial accelerometers), and excite the (sub)structure at places near to sensors, in all directions. Then, obtain the FRF matrix, the response of each direction of each sensor to each excitation point. This method do accounts just for translational directions and does not account for rotations which are known to be essential in many substructuring cases [36].

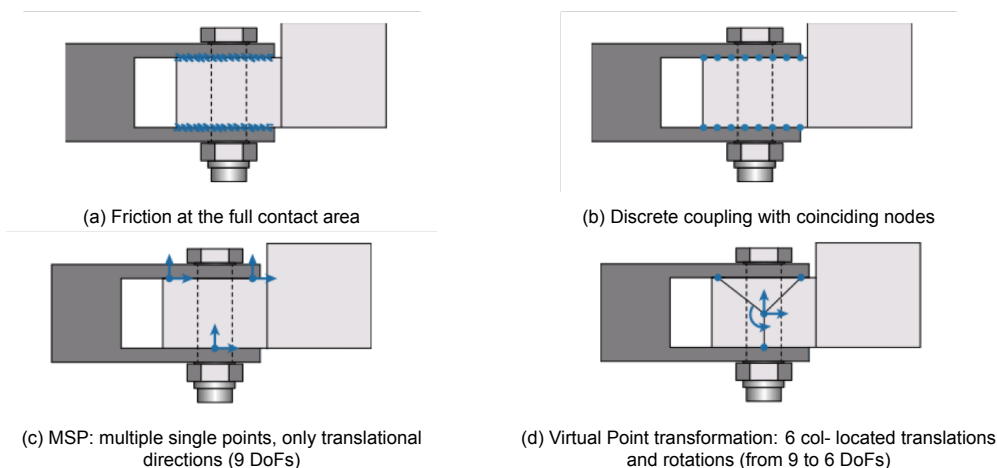


Figure 2.6: Ways Of considering interface problem, Adopted from [49]

In the experimental modeling it's not possible to measure the response of the whole connection area in all rotational and transnational directions. Literature propose two methods to accounts for rotational DoFs by using just the translational sensors, 1)Equivalent Multiple-Connection point (EMCP) and 2)Vir-

tual Point.

Equivalent Multiple-Connection point (EMCP)

A method called Equivalent Multiple-Connection point (EMCP) [42] accounts for rotations implicitly, by coupling the transnational FRFs of multiple points in the proximity of the interface, Figure(2.6c). A set of minimum 3 not in line triaxial accelerometers are sufficient to couple all translational and rotational directions, resulting in total 9 DoFs at connection point.

A common problem of mentioned methods is the practical difficulty to collect applied forces with measured displacements/acceleration. One can never excite exactly at the point where a sensor is located, which is required to measure a true driving point FRF.

Virtual Point

Another approach is the Virtual Point Transformation, see Figure(2.6d), which reduces the interface connectivity to a single point. Virtual Point Transformation projects all the *translational* displacements and forces of multiple-connection points into all 6 DoF (3 translational and 3 rotational) of a **single-connection point**, called Virtual Point (VP).

2.7.2. Virtual Point transformation

The equilibrium and compatibility condition at interface requires that substructures have the collocated (driving-point) DoFs at their interface which is shared by both side of structures. Experimentally it is difficult to measure displacement and load (for both translation and rotation) at these shared points, however Virtual Point Transformation gives a possibility to describe them.

The Virtual Point Transformation relies on the spacial reduction of coordinates, so called **Interface Displacements Modes filtering (IDMs)** [20] [16] [26]. This point is called Virtual Point as no actual measurement is at that location. The location of the Virtual Point can be chosen anywhere in proximity of the interface.

To obtain the Virtual Point Transformation first the displacements and forces at the interface need to be reduced.

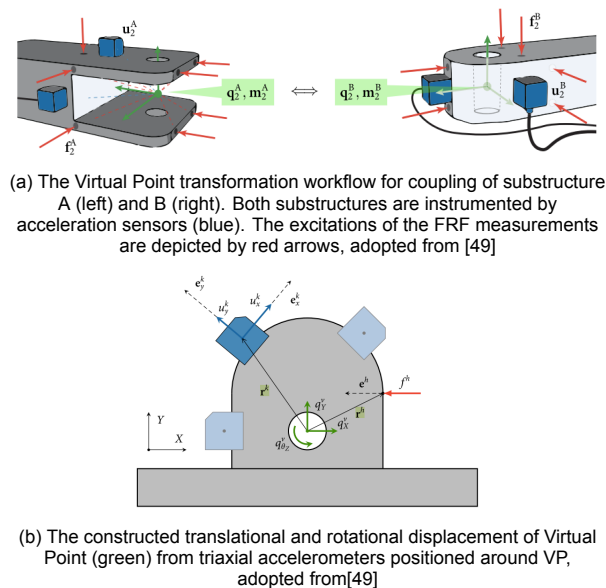


Figure 2.7: Ways Of considering interface problem, Adopted from [49]

Interface Displacement Reduction

To obtain the displacements at each Virtual Point, each VP of each substructure is surrounded by (often) 3 not-in-line triaxial accelerometers, registering a total of 9 translational displacement (At least 3 sensor is needed to gain the not-in-line condition). The IMD matrix \mathbf{R}^{kv} translates the local frame displacements of each sensor \mathbf{u}^k to 6 Virtual Point translations and rotations, gathered in vector \mathbf{q}^v , plus a residual $\boldsymbol{\mu}^k$. This residual captures all displacements not in the subspace of IDMs, which is normally the "flexible" motion or caused by measurement errors.

$$\mathbf{u}^k = \mathbf{E}^k \mathbf{R}^{kv} \mathbf{q}^v + \boldsymbol{\mu}^k \quad (2.6)$$

$$\begin{bmatrix} u_x^k \\ u_y^k \\ u_z^k \end{bmatrix} = \begin{bmatrix} e_{x,X}^k & e_{x,Y}^k & e_{x,Z}^k \\ e_{y,X}^k & e_{y,Y}^k & e_{y,Z}^k \\ e_{z,X}^k & e_{z,Y}^k & e_{z,Z}^k \end{bmatrix} \begin{bmatrix} 1 & 0 & 0 & 0 & r_z^k & -r_y^k \\ 0 & 1 & 0 & -r_z^k & 0 & r_x^k \\ 0 & 0 & 1 & r_y^k & -r_x^k & 0 \end{bmatrix} \begin{bmatrix} q_x^v \\ q_y^v \\ q_z^v \\ q_{\theta x}^v \\ q_{\theta y}^v \\ q_{\theta z}^v \end{bmatrix} + \begin{bmatrix} \mu_x^k \\ \mu_y^k \\ \mu_z^k \end{bmatrix} \quad (2.7)$$

Where \mathbf{E}^k determines the orientation of the sensor k by its three measured directions, specified as orthogonal unit vectors:

$$\mathbf{E}^k = [e_x^k \ e_y^k \ e_z^k] \quad (2.8)$$

The distance from the sensors to the Virtual Point is given by vector \mathbf{r}^k . For a typical configuration of 3 sensors per Virtual Point, these \mathbf{R}^{kv} matrices needs to be diagonally stacked in matrix \mathbf{R} .

$$\mathbf{u} = \mathbf{R}_u \mathbf{q} + \boldsymbol{\mu} \quad (2.9)$$

Interface Force Reduction

To obtain the translational and rotational forces and moments of each Virtual Point at each substructure, the substructure needs to be excited in more than 6 not-in-line excitation points in proximity at the Virtual Point. The following relation can be written for a set of Virtual Point forces and moments \mathbf{m}^v as a result of a single applied excitation \mathbf{f}^h ;

$$\mathbf{m}^v = \mathbf{R}^{hvT} \mathbf{f}^h \quad (2.10)$$

$$\begin{bmatrix} m_x^v \\ m_y^v \\ m_z^v \\ m_{\theta x}^v \\ m_{\theta y}^v \\ m_{\theta z}^v \end{bmatrix} = \begin{bmatrix} 1 & 0 & 0 \\ 0 & 1 & 0 \\ 0 & 0 & 1 \\ 0 & -r_z^h & r_y^h \\ r_z^h & 0 & -r_x^h \\ -r_y^h & -r_x^h & 0 \end{bmatrix} \begin{bmatrix} e_x^h \\ e_y^h \\ e_z^h \end{bmatrix} \mathbf{f}^h \quad (2.11)$$

The Virtual Point forces and moments are direct result of applied the forces, hence there is no need to add a residual. The system for the complete the set of DoFs is;

$$\mathbf{m} = \mathbf{R}_f^T \mathbf{f} \quad (2.12)$$

Virtual Point transformation

The Virtual Point admittance describes the relation between the displacements (both translational and rotational) and forces/moments at the Virtual Point. To obtain a VP admittance matrix \mathbf{Y}_{qm} , the actual FRF describing the relation of sensors and impacts to the VP needs to be pre-multiplied and multiplied by displacement transformation matrix \mathbf{T}_u and force transformation matrix \mathbf{T}_f .

$$\mathbf{Y}_{qm} = \mathbf{T}_u \mathbf{Y} \mathbf{T}_f^T \quad (2.13)$$

where transformation matrices \mathbf{T}_u and \mathbf{T}_f can be computed from IDM matrices \mathbf{R}_u and \mathbf{R}_f ;

$$\mathbf{T}_u = (\mathbf{R}_u^T \mathbf{W}_u \mathbf{R}_u)^{-1} \mathbf{R}_u^T \mathbf{W}_u \quad , \quad \mathbf{T}_f = \mathbf{W}_f \mathbf{R}_f (\mathbf{R}_f^T \mathbf{W}_f \mathbf{R}_f)^{-1} \quad (2.14)$$

The \mathbf{W}_u and \mathbf{W}_f are weighing matrices. In [49] these are assumed to be identity matrices.

2.8. Methods for quality indication of VP

The methods for quality indications can be categorized in as follows; Decomposition techniques, Coherency analysis, Reciprocity, Driving point passivity.

2.8.1. Decomposition techniques

- **Contribution analysis (CMIF)**

Complex Mode Indicator Function, CMIF, is an algorithm that applies **SVD** (singular value decomposition) to a FRF matrix for every frequency. It is a method to identify closely spaced or repeated modal frequencies, and it can be use in modal parameter estimation. CMIF reveals the dynamic mode shapes that build up the FRFs, and shows which are the most dominant for every frequency.

CMIF CMIF can also be used to identify error in the measurement data, which can be investigated by two ways:

- At low frequency, far before the first elastic resonance frequency, the rigid body modes are the only modes that are acting, and no other dynamics is to be expected. An additional modes at those frequencies will be treated as non-physical modes. Non-physical modes and unexpected physics indicates some errors during measurements, caused for example by overshoots or bad sensors signals. As CMIF can extract all the available modes at each frequency, it can reveal if at low frequencies the nonphysical modes are present or not.
- Another use of CMIF is **detecting a channel (sensor or impact) causing bad dynamics** [37], by inspecting the left and right vectors of the **significant singular values** at low frequency. The left vector \mathbf{U} and right vector \mathbf{V} reveal respectively the sensor and impacts signals and are orthogonal. The orthogonality property gives these vectors the opportunity to calculate the contribution matrix when squared.

$$\sum_i^m |U_{is}|^2 = 1 \quad \text{and} \quad \sum_i^n |V_{is}|^2 = 1 \quad (2.15)$$

The bad dynamics will cause a poor distribution of the mode shape, it means all available DOFs pointing on a certain direction do not have equally contribution to that DOF.

For example, if multiple sensor channels are pointed into the x-direction, and one of the singular value modes is a translation in x-direction, the contribution to that mode shape will be evenly distributed to all sensor channels in x direction. In contrast, 'bad' dynamics is often related to a single input or output. This results in a poor distribution of the mode shape, or in other words, all contribution concentrated onto one DoF.

- **Operational Deflection Shape (ODS)**

The Operational Deflection Shape (ODS) analysis is a method used to visualize the vibration pattern of a structure at a certain load-case. It animates the deflection of the sensors on the structure at a particular frequency The ODS is a very useful tool to assess the quality of the VPT by looking at the structure's motion associated with some virtual FRFs, and facilitating the identification of incorrect positioning of impacts and sensors.

- **SVD ODS; ODS of left and right vectors of SVD**

Visualizing the left and right vectors of SVD to identify alignment or positioning mistakes in the bookkeeping of sensor and impacts [37].

- **IDM polar Decomposition [37]**

Calculation of Virtual Point FRF, Y_{qm} , uses the transformation matrix T . T is a least square inverse, and as a consequence the values in the matrix are not intuitive and difficult to see which channels will contribute to which Virtual Point DoF.

Polar decomposition to the inverse IDM matrix, $T=QS$. (Q is orthogonal matrix, and S a symmetric matrix, for geometric transformation: Q is rotation, and S is scaling matrix). As Q is orthonor-

mal, the rows related to each DoF are normalized, and can be interpreted as contribution when squared. (This is similar to the CMIF contribution analysis approach) shows which measured DoF (u or f) contributed to which virtual DoF (q or m).

$$\sum_{k=1}^{n_k} |Q_{qk}|^2 = 1 \quad (2.16)$$

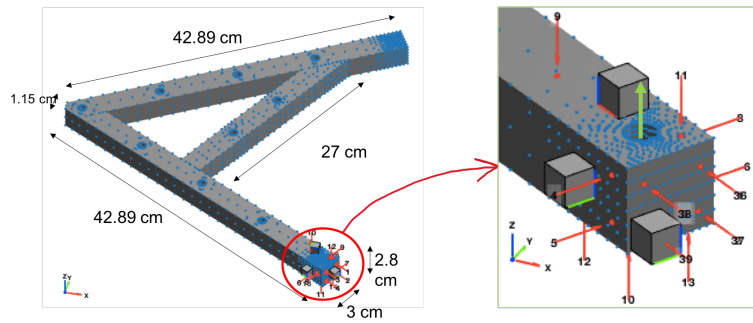
Where n_k is the number of impacts or channels, and q is the Virtual Point DoF. Where particular input (sensor channels or impacts) gives high contribution to certain DoF, the user can anticipate on it by either moving the input to another location, or making sure to operate careful measurements for this particular input.

The conditioning number of scaling matrix S give insight in the quality of T.

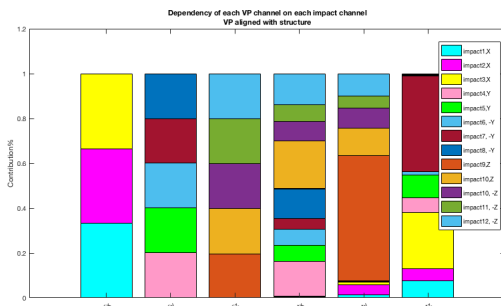
IDM decomposition indicates which part of the measurement data will contribute the most to Virtual Point DoF, is useful for set up the Virtual Point.

An example for this contribution analysis is illustrated on Figure.2.8, where impacts and VP DoFs share the same local coordinate system. Figure.2.8b illustrates the dependency of each VP's DoF on each impact, by comparing the Q_{qk}^2 value of DoF q of VP. This analysis is done for a FEM model illustrated on Figure.2.8a where 12 impacts are used to make a single VP. Figure.2.8c shows the contribution of each impact on VP.

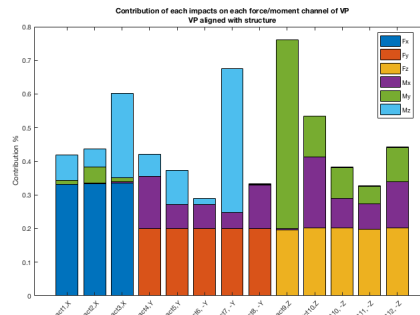
An example for this contribution analysis is illustrated on Figure.2.8, For a FEM model, where 12 impacts and 6 VP's DoFs share the same local coordinate system. Figure.2.8b illustrates the dependency of each VP's DoF on each impact, by comparing the Q_{qk}^2 value of DoF q of VP. Figure.2.8c shows the amount of contribution of each impact on each VP's DoF.



(a) FEM model, with 12 impacts (red arrows) and a Virtual Point with 6 DoFs (green arrows)



(b) Dependency of each VP's DoF (forces and moments) on each impact



(c) Amount of Contribution of each impact on the calculation of each force and moment DoF of VP

Figure 2.8: Polar decomposition analysis for a FEM model(a)

2.8.2. Coherence analysis

An important ability of the Virtual Point transformation is the ability to quantify the measurement consistency. There are two main consistency functions:

- **Sensor consistency**

Sensor consistency functions compare the measured responses \mathbf{u} with the responses after projection onto IDMs, $\tilde{\mathbf{u}}$. It was originally proposed in [16] as the **interface rigidity indication**. The sensor consistency can be shown in two forms

- **Overall sensor consistency**, compares the **norm** of both filtered and unfiltered responses, and yield a frequency dependent function bounded by one (full consistency) and zero (no consistency). If the value drops at a certain frequency, it is often an indication of the presence of a flexible interface mode.

$$\rho_{u_{i,j}}(\omega)^{overall} = \frac{\|\tilde{u}_{i,j}(\omega)\|}{\|u_{i,j}(\omega)\|} \quad (2.17)$$

- **Specific sensor consistency**, evaluates the consistency per measurement channel, by looking to the **spectral coherence** of two spectra. The coherence function compares two complex values with respect to their amplitude and phase, and again is bounded between one and zero. Specific consistency allows to evaluate the consistency of each measurement channel with respect to the full transformation. In this way, the problematic sensor can be identified.

$$\rho_{u_{i,j}}(\omega)^{specific} = \text{coh}(\tilde{u}_{i,j}(\omega), u_{i,j}(\omega)) \quad (2.18)$$

- **Impacts consistency**

Like sensors consistency, impacts consistencies can be obtained, as **overall impacts consistency** and **specific impacts consistency**, which is again the comparison between filtered forces $\tilde{\mathbf{f}}$ and unfiltered forces \mathbf{f} . The procedure for analysis is the same as for sensors consistency

Different types of coherency functions can be used to examine the relation between two signals or data set. In dynamic substructuring the previous works suggests the following methods, which are not going to be discussed here.

- **Regular Consistency** [49]
- **Log consistency** [37]
- **Multiple Coherence** [37]

2.8.3. Reciprocity

As sensor and impacts are not collocated (are not placed in the same locations), the measured admittance matrix is not reciprocal. Since Virtual Point forces and displacements are collocated, the reciprocity of Virtual Point admittance should be symmetric and can be verified. To do this, a frequency dependent coherency function can be used to evaluate the reciprocal elements of Virtual Point admittance matrix, $\mathbf{Y}_{i,j}$ and $\mathbf{Y}_{j,i}$, and indicate the level of similarity between them, which has a value between 0 and 1.

$$X_{i,j} = \text{coh}(\mathbf{Y}_{i,j}, \mathbf{Y}_{j,i}) \quad \mathbf{Y}_{i,j}, \mathbf{Y}_{j,i} \in \mathbf{Y}_{vp} \quad (2.19)$$

2.8.4. Driving point passivity

A complementary condition to reciprocity is passivity, which can be evaluate on the diagonal elements of the Virtual Point admittance matrix. In the context of driving point FRFs, the passive behavior means that the driving points FRFs (diagonal elements of matrix) need to be minimum-phase function. This implies that an applied force at DoF i must always result in a displacement in the same direction at that point. If the function is not minimum-phase, it indicates that energy is added after the impulse, which contradicts system passivity [28].

The diagonal elements of Virtual Point FRF are the only entries that must demonstrate minimum phase response:

$$\angle Y_{i,i} = \begin{cases} \in [-180, 0] & \text{for receptance FRFs} \\ \in [-90, 90] & \text{for mobility FRFs} \\ \in [0, +180] & \text{for accelerance FRFs} \end{cases} \quad Y_{i,i} \in Y_{vp} \quad (2.20)$$

2.9. Conclusion of literature survey

From the literature study on the field of Experimental Dynamic Substructuring and reviewing the challenges of the field, we have seen different methods are developed and used for quality indication of Virtual Point. However, we did not find any coherent study about the propagation of the inaccuracy of the location and the direction of sensors and impacts on the transformed recorded data to Virtual Point. Voormeeren *et al* [50] have shown that uncertainties in the interface point FRFs (i.g. Virtual Point) cause propagation of uncertainty in all of the FRFs of the assembled system. This arises the importance of having an accurate calculation of Virtual Point FRFs.

The second part of this thesis is an investigation to find an answer for the following question:

How an uncertainty on the position and direction of the force/accelerometers sensors affects the calculated frequency response function of Virtual Point.



Uncertainty propagation from measurements to Virtual Point (VP)

3

Introduction

In the previous part, we reviewed the literature to define the scope of this thesis and clarify the goals of it. The second part of this thesis is an investigation to analyze the uncertainty propagation to the calculation of Virtual Point frequency response function, caused by inaccurate estimation of sensors' and impacts' position and direction.

In Experimental dynamics, we need experimentally gained information recorded by sensors and roving impacts to build the FRF, to be able to calculate the Virtual Point transformed FRF. In all experiments, we almost always have some uncertainties, and achieving true experiment is almost impossible. Making errors while mounting the sensors and roving impacts is very plausible. This mounting errors can be **positional** as well as **directional**. Because of these uncertainties, we can never find the true transformation matrices.

To calculate the Virtual Point admittance (for further substructuring), the data from measurements will be transformed by using the projection matrices T_u and T_f . These transformation matrices are all described in Cartesian coordinate system, the theory from Section.4.2. These projection matrices use the *locational distances* $(r_x^{kv}, r_y^{kv}, r_z^{kv})$, $(r_x^{jv}, r_y^{jv}, r_z^{jv})$ and *directional differences* $(\theta_x^{kv}, \theta_y^{kv}, \theta_z^{kv})$, $(\theta_x^{jv}, \theta_y^{jv}, \theta_z^{jv})$ between measurements palces, sensor k and impacts j , and Virtual Point VP .

Existence of *directional and rotational uncertainty on sensors or impacts* can cause an error generation on the calculation of Virtual Point (VP) admittance (Y_{vp}).

The main goal of this study is to understand:

How an *uncertainty on the position and direction of the force/accelerometers sensors* affects the calculated frequency response function of Virtual Point.

This study investigates to understand how these types of measurement errors affect the calculation of VP 's FRF by answering the following questions:

- **Which error at what amount is the most dominant error source?**
- **At which frequencies we can expect the less precise?**

In the second part of the thesis, chapter.4 analyzes the problem by studying how a Virtual Point's FRF is calculated, and how each component of calculation works through the computation of Virtual Point' FRF, and how uncertainty affects the way each component contributes to the computation of VP 's FRF,

Section.4.2.

In section.4.3 the theory of component mode synthesized (CMS) is used to describe how uncertainty in an input or output can influence the admittance.

Based on the theory of component mode synthesized (CMS), we know that the frequency response function Y_{ij} at and around each resonance (ω_{rn}) between impact j and sensor i is governing by the modal values of input i and output j corresponds to that resonance. Since these values and their contribution is mode shape and frequency-dependent, the problem refines and focused on the resonances and their dominant mode shape motion. Then the relation between the error direction and mode shape is studied (for both positional and directional uncertainties), and based on that, the *dominant error sources* are identified. Furthermore, the amount of uncertainty propagation into the VP 's DoFs is quantified.

Applying an exact amount of positional and directional error (uncertainty) on the sensor and impact in an experiment is challenging, and obtaining the true experiment is almost impossible. For this reason, this study uses simulation to mimics an experiment.

Four types of uncertain scenarios are considered; impacts positional uncertainty (IPU), impacts directional uncertainty (IDU), sensors positional uncertainty (SPU), and sensors directional uncertainty (SDU). Each scenario contains just one type of uncertainty.

In chapter.5 three different approaches are considered analytical approach, numerical approach, and Monte Carlo simulation. Each method considers each of four uncertainty scenarios (IPU, IDU, SPU, and SDU) separately.

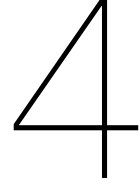
The analytical approach (section.5.2) considers a free end part of a beam, to mimic the coupling area. This method used the modal values and considered the effect of each of the four uncertainty scenarios on different mode shapes. Based on dominant modal values, the *dominant error directions* for each mode shape for each scenario is introduced. Moreover, an estimation is given on the changes of the (calculated) Virtual Point's forces and responses, caused by these dominant error sources.

In section.5.3 a complex modal based model (FEM) is introduced. Section.5.4 discussed how a Monte Carlo simulation is adopted on the complex modal based model to implement the random errors for each type of uncertainty for a massive number of times.

Chapter.6 shows and then discusses the results of the numerical approach. In Section.6.1 every scenario is simulated on a complex modal-model, for a well-defined amount of error. Then a Monte Carlo simulation is used to bring random errors on each variable (still for each scenario). In the discussion part of chapter.6, the results of simulations are compared with each other and then compared with the expectations from the analytical analysis.

The chapters of the second part of this thesis are as follows

- Section.4: Analyzing the problem
- Section.5: Methodology
- Section.6: Results and discussion
- Section.7: Conclusion



Analyzing the problem

To analyze the problem, first of all, we need to decompose the problem. The first section of this chapter, section.4.1 studies how a Virtual Point's FRF is calculated (on section.??), Furthermore, how (positional or directional) uncertainty affects the way each component contributes to the computation of Virtual Point' FRF. Section.4.2 discussed how uncertainty affects the accuracy of transformation matrices T_u and T_f , and how the inaccurate transformation matrices affect the Virtual Point's transformation. Moreover, based on the decomposition of the transformation matrices, a prediction is made to find the VP's cross-functions with higher sensitivity to the (positional and directional) inaccuracies of the measuring equipment.

Sections.4.3 uses the Component Mode Synthesis method to discuss how inaccuracy affects the measured FRF, for both positional and directional uncertainties and both input and output. Section.?? debates why this uncertainty is mode shape and frequency-dependent.

4.1. Decomposing the problem

The measured cross-functions (in the frequency domain) between all force channels (inputs) and sensors channels (outputs) are all gathered in an admittance matrix Y_{meas} . Transformation matrices T_u and T_f transform the measured FRFs to a single coupling point for further substructuring. This single coupling point is called Virtual Point (VP), which is a **collocated super-element** having both translational and rotational DoFs, the theory from section.2.7.2. Recalling the equation that computes the VP's FRF:

$$Y_{vp} = T_u Y T_f^T \quad (4.1)$$

Equation.4.1 shows that the computation of VP's FRF consists of :

- Displacement transformation matrix T_u .
- Measured frequency response function; Y .
- Force transformation matrix T_f .

The transformation matrices use the *locational distances* (r_x, r_y, r_z) and *directional differences* ($\theta_x, \theta_y, \theta_z$) between the measurements places and Virtual Point, to convert the measured data into a Virtual Point. This transformation matrices are all described in Cartesian coordinate system.

Since we never know the actual position and direction of sensors and impacts during the measurements, we can not accurately set up the projection matrices T_u and T_f . This uncertain estimation of

position and direction is the main reason to get the deviation on the calculation of VP 's frequency response function. In other words, as long as we *accurately compile the transformation matrices* T_u and T_f , we will end up to the same calculated FRF at VP (if we accomplish the linearity assumption), no matter where we excite or measure the response of the structure. Note that this is just valid under the local rigidity condition in the measuring area, meaning that the structure's deformation does not involve any shear, extension, or compression in the area where we excite or measure or set the Virtual Point.

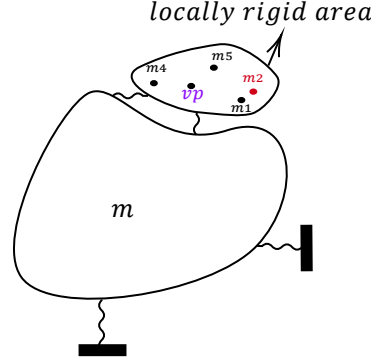


Figure 4.1: Local linearity and rigidity of the measured area, the main assumption of Virtual Point Transformation

In the presence of measurement's uncertainty on the positioning of the sensors or roving hammers, the measured FRF can be decomposed into two parts.

- Y_{true} : Measurement without any uncertainty.
- ΔY : A deviation on measured FRF from the true measurements, caused by uncertainty.

$$Y_{uncertain} = Y_{true} + \Delta Y \quad (4.2)$$

The uncertainty propagates during the transformation, and the *uncertain* VP 's FRF consequently can be written as follow:

$$\begin{aligned} Y_{vp,uncertain} &= Y_{vp,true} + \Delta Y_{vp} \\ &= T_u \cdot (Y_{true} + \Delta Y) \cdot T_f^T \end{aligned} \quad (4.3)$$

The deviated transformed admittance ΔY_{vp} is due to *inaccurate estimation* of transformation matrices T_u and T_f .

4.2. Transformation matrices T_u and T_f as an uncertainty amplification factors

If we are not accurately aware of the locational or directional changes, we will set up the displacement and force transformation matrices, T_u , and T_f , in an unappreciated and inaccurate way. Now we need to consider *how the uncertain transformation matrix affects the calculation of the VP 's admittance*.

In order to understand how the transformation matrices T_u and T_f has influenced the VP 's FRF calculation, first of all, we study in detail how these matrices are made, and then further how they transform data which are not entirely belong to them.

4.2.1. Setup of transformation matrices T_u and T_f

The displacement transformation matrix, T_u , is made of different displacement transformation matrices. Each of these sub-transformation matrices, T_u^{kv} , converts data from sensor k to a Virtual Point in the Cartesian coordinate system. Since each sensor has 3 DoFs, T_u^{kv} is a matrix and not a vector. Every sensor's displacement transformation matrix T_u^{kv} is decomposed of two parts. The **rotational**

projection matrix and translational projection matrix.

Recalling that each Virtual Point (VP) is a collocated super-element, having 6 Dofs on responses (3 translational and 3 rotational) and 6 DoFs on Forces (3 translational forces and 3 moments) on Cartesian coordinate system. It means that a VP's FRF at each frequency is a 6×6 matrix.

The transformation of measured responses (translational), $\mathbf{u}_{meas.}$, into VP's responses \mathbf{q}_{vp} (both translational and rotational) is as follows

$$\begin{aligned} \mathbf{q}_{vp} &= \mathbf{T}_u \mathbf{u}_{meas.} \\ \mathbf{u}_{meas.} &= \mathbf{R}_u \mathbf{q}_{vp} \end{aligned} \quad \text{where } \mathbf{R}_u = \mathbf{T}_u^{-1} \quad (4.4)$$

Since the first 3 rows of VP's admittance represent the displacement, the **transposed of translational** projection matrix is forming the **upper part** of transformation matrix \mathbf{T}_u^{kv} . And, the **transposed of rotational** transformation part creates the **bottom part** of displacement transformation matrix \mathbf{T}_u^{kv} .

$$\mathbf{R}_u^{kv} = \mathbf{T}_u^{kv^{-1}} = \begin{bmatrix} \mathbf{E}^{kv^T} & (\mathbf{r}^{kv} \times \mathbf{E}^{kv})^T \end{bmatrix} \quad \text{where } \Rightarrow \begin{cases} translation & : (\mathbf{r}^{kv} \times \mathbf{E}^{kv})^T \\ rotation & : \mathbf{E}^{kv^T} \end{cases} \quad (4.5)$$

The rotation part describes the **rotation matrix of Euler angles** (three angles). This Euler angle reflects the relative angle between the sensor and the VP coordinate system. The rotation matrix of sensor k with respect to Virtual Point is as follows:

$$\mathbf{E}^{kv} = \mathbf{R}_z(\alpha)\mathbf{R}_y(\beta)\mathbf{R}_x(\gamma) \quad (4.6)$$

Where α , β and γ are the angle differences between sensor k and VP, in z, y and x direction, respectively.

In fact, Each column i of displacement transformation matrix \mathbf{T}_u transform the displacement of channel i to translational and rotational displacement of Virtual Point, with relative direction vector \mathbf{e}_i^{kv} and relative distance vector \mathbf{r}_i^{kv} with respect to VP.

$$\mathbf{R}_u^{kv} = (\mathbf{T}_u^{kv})^{-1} = \begin{bmatrix} \mathbf{R}_z(\alpha)\mathbf{R}_y(\beta)\mathbf{R}_x(\gamma) \end{bmatrix} \begin{bmatrix} 1 & 0 & 0 & 0 & r_z^{kv} & -r_y^{kv} \\ 0 & 1 & 0 & -r_z^{kv} & 0 & r_x^{kv} \\ 0 & 0 & 1 & r_y^{kv} & -r_x^{kv} & 0 \end{bmatrix} \quad (4.7)$$

The same procedure is used to calculate the **force transformation matrix** \mathbf{T}_f , which transforms the forces from impacts $\mathbf{f}_{meas.}$ to forces and moments at Virtual Point \mathbf{f}_{vp} .

$$\begin{aligned} \mathbf{f}_{vp} &= \mathbf{R}_f^T \mathbf{f}_{meas.} \\ \mathbf{f}_{meas.} &= \mathbf{T}_f^{-T} \mathbf{f}_{vp} \end{aligned} \quad \text{where } \mathbf{R}_f = \mathbf{T}_f^{-1} \quad (4.8)$$

Note that in the calculation of VP's FRF, we use the *transposed* of force transformation matrix $(\mathbf{T}_f)^T$, which has 6 columns, and the number of rows is equal to the number of impacts.

In the transposed of force transformation matrix \mathbf{T}_f^T , each *row* j is responsible to transform the force of impact-channel j to force and moment of Virtual Point, with relative direction vector \mathbf{e}_i^{jv} and relative distance vector \mathbf{r}_i^{jv} with respect to VP. The force transformation matrix \mathbf{T}_f has two parts, the **translational** part and the **rotational** part, which are respectively building the **left part** and **right part** of transformation matrix.

$$\mathbf{R}_f^{jv^T} = (\mathbf{T}_f^{jv^T})^{-1} = \begin{bmatrix} \mathbf{e}^{jv^T} \\ (\mathbf{r}^{jv} \times \mathbf{e}^{jv})^T \end{bmatrix} \quad \text{where } \Rightarrow \begin{cases} translation & : (\mathbf{r}^{jv} \times \mathbf{e}^{jv})^T \\ rotation & : \mathbf{e}^{jv^T} \end{cases} \quad (4.9)$$

4.2.2. How inaccurate transformation matrices affects the VP 's calculation

Since the translational part of transformation matrices reflecting the relative distance between sensor/impact and VP , *their value is much smaller compared with the values of rotational part*, which has values between -1 and 1. As a consequence, if a measurement contains some uncertainty, the rotation part of projection matrices amplifies the uncertainty on the measured frequency response function (Y_{meas}) more than the translational part.

In order to understand how uncertain measurement propagates into VP 's FRF, we study the deviation of incorrect transformed FRF from its true value, ΔY_{vp} .

First, we consider the calculation part between T_u and ΔY . We have seen that the lower part of T_u (responsible for rotational transformation) has higher values comparing with the upper part of the matrix. As a consequence, the product of $T_u * \Delta Y$ has a **higher values on the lower part** of this product matrix.

Then we need to multiply the product of $T_u * \Delta Y$ with the transposed of force transformation matrix T_f^T . As discussed before, the **right part** of T_f^T was responsible for rotational transformation and **has relative higher values** comparing with translational part.

All these together we expect that the product of $T_u * \Delta Y * T_f^T$, which results in a 6×6 matrix (at each frequency), will have higher values on the **SE** (South-East) part of the VP 's admittance matrix.

We may conclude;

If during an operational measurement we measure the input and/or output with inaccurate position (location and/or direction), then the deviation on transformed admittance ΔY_{vp} which is a product of $T_u * \Delta Y * T_f^T$ will have higher values on its **SE** (South-East) part.

$$T_u = \begin{bmatrix} \text{Translation} \\ \text{Rotation} \end{bmatrix}, \quad \Delta Y = \begin{bmatrix} \text{Translation} \\ \text{Rotation} \end{bmatrix}, \quad T_f^T = \begin{bmatrix} \text{Translation} \\ \text{Rotation} \end{bmatrix}$$

$$\Delta Y_{vp} = T_u \Delta Y T_f^T = \begin{bmatrix} NW & NE \\ SW & SE \end{bmatrix}$$

4.2.3. Influence of relative distances and relative directions of all impacts to VP

We have seen that the projection matrices R_u and R_f are composed of all relative distances and relative orientations of every input and output to VP . During the transformation from the measured admittance to the VP 's admittance, we use T_u and T_f , which are the Pseudo inverse of these projection matrices R_u and R_f . As these two transformation matrices (T_u and T_f) are the inverse, all of the relative distances and relative orientations (of inputs and outputs with respect to VP) will influence the values of each entry of these transformation matrices.

The effect of dominant impacts and sensors is not just depending on their relative distances and orientation with respect to VP , but also the distance and orientation of other impacts and sensors matters and contributes to the error propagation. This means that any inaccurate estimation on location or direction propagates to the whole transformation matrix (T_u or T_f).

4.3. How uncertainty affects the measured Frequency Response Function

In the previous section, we discussed how the decomposition of transformation matrices (T_u and T_f) could amplify the measurement uncertainties, and consequently causes that the VP 's rotational/rotational cross-functions become least precise.

We need to understand which measured cross-functions containing higher deviations, in order to define which entries of that least precise part of VP 's admittance (SE part or rotational/rotational cross-functions) do contain the highest error generation.

In this section, the Component Mode Synthesis (CMS) is used to understand how positional or directional uncertainty changes a measured frequency response function. First, the case of positional uncertainty is discussed and then directional uncertainty.

Component Mode Synthesis (CMS)

As discussed in section.2.3.1 the admittance FRFs can be synthesized using a superposition of single-DoF modal solutions (natural modes). Recalling the formula from section.2.3.1, the frequency response function $Y_{ij}(\omega)$ of output i and input j reads as follows:

$$Y_{ij}(\omega) = \sum_{n=1}^k \frac{\phi_{i,n}\phi_{j,n}}{-\omega^2 + 2\zeta_n\omega_n\omega + \omega_n^2} \quad (4.10)$$

$$= \frac{\phi_{i,1}\phi_{j,1}}{-\omega^2 + 2\zeta_1\omega_1\omega + \omega_1^2} + \frac{\phi_{i,2}\phi_{j,2}}{-\omega^2 + 2\zeta_2\omega_2\omega + \omega_2^2} + \dots + \frac{\phi_{i,k}\phi_{j,k}}{-\omega^2 + 2\zeta_k\omega_k\omega + \omega_k^2}$$

Where k is the total considered modes in the calculation, n is the number of mode, and ω_n is the eigenfrequency of that mode number. ϕ_i^n and ϕ_j^n are representing the modal-value of output (or response) i and modal-value of input (or force) j at mode number n .

4.3.1. Mode and frequency dependency on uncertainty propagation to VP 's FRF

Each decomposed part of Equation.4.10, is governing the general behaviour of frequency response function *at and around its corresponding eigenfrequency* ω_n . By slightly changing the measurement setup (slightly changing the position or the direction of sensor or impact), we are not changing the structure (ignoring the changes due to sensors mass and its influences), and consequently, the resonance frequencies (ω_n) are remaining the same. It means changes in the position or direction of input or output do not change the *denominator part* of each decomposed part of mode synthesized.

However, in the presence of positional uncertainty (of the measuring equipment(s)), we actually measure the response of a node (or discretized mass), which is placed just next to the *true node*. The recorded data are not any more accurately representative of how that targeted node (true node) of structure responds to an excitation.

It means, in the presence of positional uncertainty in a measurement, the modes synthesized admittance is not anymore reflecting the modal values of true-positioned input or output. The presented modal values are belonging to a place just next to the true position.

$$Y_{ij}(\omega) = \sum_{n=1}^k \frac{\phi_{i,n} \phi_{j,n}^T}{-\omega^2 + 2\zeta_n \omega \omega_n + \omega_n^2} \quad (4.11)$$

contribution of mode n : $\frac{\phi_{i,n} \phi_{j,n}^T}{-\omega^2 + 2\zeta_n \omega \omega_n + \omega_n^2}$

On each decomposed part of Equation.4.13, the denominator $(-\omega^2 + 2\zeta_n \omega \omega_n + \omega_n^2)$ defines at which frequency a peak occurs, where the nominator $(\phi_i^n \phi_j^n)$ determine the value of the amplitude. Therefore, by changing the modal value vector (ϕ_i^n) , the eigenfrequencies remain the same, so the structure will still resonate at the same frequencies. However, the value of the amplitude will change. It means, in the presence of positional (or directional uncertainty), the portion of the contribution of each normal mode on the composed end-product Y_{ij} will change, and the amount of contribution of these changes is depending on the frequency.

In order to find the dominant error sources, in the next chapter, on analytical approach (section.5.2), we discuss in details the effective factors influencing the *amount* of the changes on the modal value $\delta\phi_i$ or $\delta\phi_j$. These factors are; the amount of uncertainty, the direction of uncertainty, relative distance of measuring point to VP , and the relative distance of measuring point to stand node (number of each mode shape).

4.3.2. Directional uncertainty in measuring equipment

In this section, the propagation of the second type of measurement uncertainty is investigated, namely the Directional uncertainty of input or/and output.

Since the modal value of non-dominant directions of that mode shape is significantly smaller, the contribution of their corresponding normal mode on mode synthesized is also small. As a consequence, the amplitude of frequency response function at and around that specific resonance is small with no peaks.

In the presence of directional uncertainty, the modal values extracted from measurements are not anymore representing the modal value of the direction assigned to the projection matrix, and consequently, measured data will incorrectly be projected to VP .

In the mode synthesized form, a part of the modal value will be replaced by the modal value of another direction. If the new added direction has the same direction as the mode shape motion, then the added modal value is a portion of high value, and consequently, the modal value for that natural mode will increase significantly. If it happens, some peaks will appear at frequencies corresponds to that mode shape.

Figure.4.2 illustrates two FRFs, one in blue and one in green, where each of them corresponds to one channel of a sensor. The sensor is mounted in such a way that each channel is just bale to record the motion of one type mode-shape (for example, one can just record lateral bending and one just vertical bending). Since each channel can just record one of the motions, each cross-function contains one peak at a frequency corresponds to one mode shape.

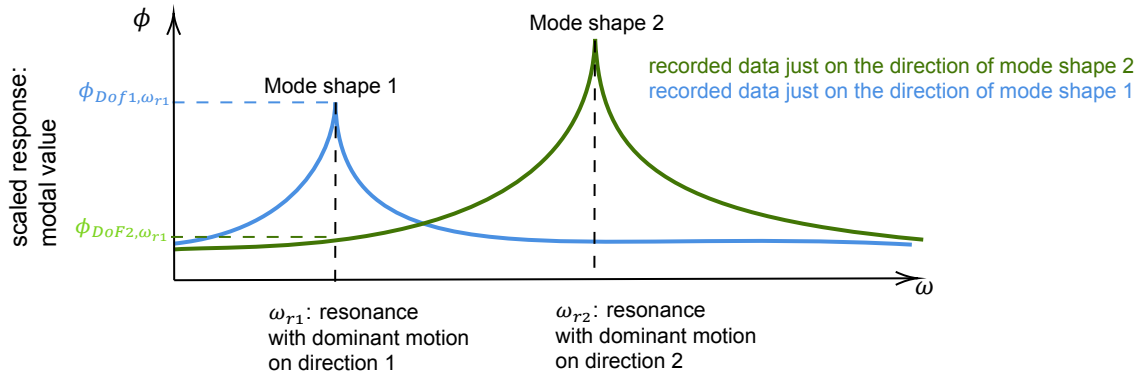


Figure 4.2: FRF directional1

If the sensor has some *directional uncertainty*, in such a way where one channel is recording the motion of other direction, then we expect to observe a spurious peak at resonances corresponds to new added direction, which are not belong to the true direction. Figure.4.3 illustrates this new FRF which is called a multi directional recorded data.

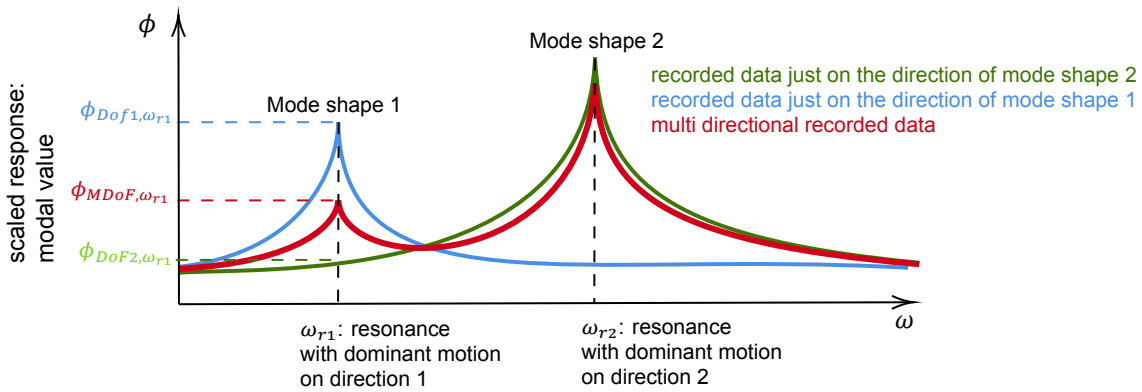


Figure 4.3: FRF directional2

At each frequency, the *amount* of the contribution of each DoF on the Multi directional (MDoF) recorded data is depending on the *amount of the response* of each direction, and the *amount of contribution* of each direction

If a force is a multiple-directional load (exciting a structure on more than one (local) DoF), then the *modal vector of that output* (reference i) becomes a multi-DoF modal value ϕ_{iMD} , which is a combination of the eigenvectors of both directions, so each direction gets a portion on the final modal vector for reference i :

$$\phi_{iMD} = \alpha_i \phi_{ix} + \beta_i \phi_{iy} \quad (4.12)$$

Where α and β denotes the portions of the components of each eigenvectors (for each DoF) for that reference i .

In the presence of multi-directional (MD) modal vector of reference i , the synthesized FRF is becoming as follows:

$$Y_{ij} = \sum_{n=1}^k \frac{\phi_{iMD}^n \phi_j^n}{-\omega^2 + 2\zeta \omega_{rn} \omega + \omega_{rn}^2} = \sum_{n=1}^k \frac{(\alpha_i \phi_{ix}^n + \beta_i \phi_{iy}^n) \phi_j^n}{-\omega^2 + 2\zeta \omega_{rn} \omega + \omega_{rn}^2} \quad (4.13)$$

In this case the force (input i) is decomposed of two directions, f_{ix} and f_{iy} . Components α and β have the following relation with f_{ix} and f_{iy} :

$$\frac{f_{ix}}{f_{iy}} = \frac{\alpha_i}{\beta_i} \quad (4.14)$$

Based on the CMS method, every modal value of input and output has a contribution in the calculation of the cross function. The amount of the contribution of each of them depends on the frequency. In the case of multi-directional input or output (with respect to local coordinate), the modal parameters of each reference (input or output) are the decomposition of different modal values of a different direction for that reference. By changing the direction of the input or output, the portion of each modal parameters at that reference will change, which means change on values of α and β .

In the presence of *directional uncertainty* on input or output, the *values of both α and β are becoming uncertain*. Moreover, the values of the modal parameters of different directions are becoming error amplification factors. The amount of generated deviation on FRF depends on the modal parameters of both directions (or in general all directions).

It means any changes on the component of modal value ϕ_x or ϕ_y with higher value will amplify the error more than a one with smaller value. Furthermore, since the components of each eigenvector have different values, and each component becomes dominant around its corresponding eigenfrequency, the *generated error on synthesized FRF is the frequency and mode dependent*.

5

Methodology

5.1. Introduction

Applying an exact amount of positional and directional error (uncertainty) on the sensor and impact in an experiment is challenging, and obtaining the true experiment is almost impossible. For this reason, this chapter uses analytical analysis and FEM to mimics an experiment and the consequences of the measuring equipment's directional uncertainties and positional uncertainties on the determination of Virtual Point (VP).

Four types of uncertain scenarios are considered; impacts positional uncertainty (IPU), impacts directional uncertainty (IDU), sensors positional uncertainty (SPU), and sensors directional uncertainty (SDU). Each scenario contains just one type of uncertainty.

In this chapter, three different approaches are considered analytical approach, numerical approach, and Monte Carlo simulation. Each method considers each of four uncertainty scenarios (IPU, IDU, SPU, and SDU), separately.

The analytical approach (section.5.2) considers a free end part of a beam, to mimic the coupling area. This method used the modal values and considered the effect of each of the four uncertainty scenarios on different mode shapes. Based on dominant modal values, the *dominant error directions* for each mode shape and for each scenario is introduced. Moreover, an estimation is given on the changes of the (calculated) Virtual Point's forces and responses, caused by these dominant error sources.

In section.5.3 a complex modal based model (FEM) is introduced. Section.5.4 discussed how a Monte Carlo simulation is adopted on the complex modal based model to implement the random errors for each type of uncertainty for a massive number of times.

5.2. Analytical approach

In the analytical approach, We simplify the coupling area into a free-end part of a structure, in order to mimic the area of measurement and transformations into VP . We decide to study a part of a structure with a *free-end*, since the end purpose of this study is meant for substructuring and coupling using a Virtual Point Transformation, and in the most cases the coupling area of the substructure is a free-end part of substructure (at least locally).

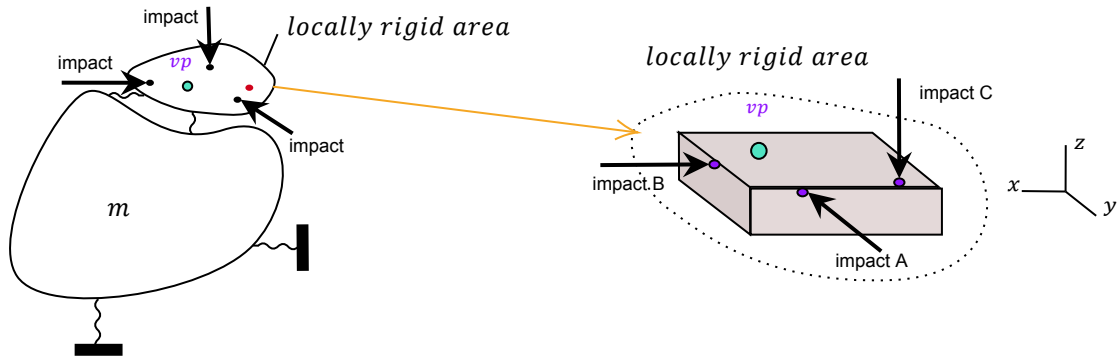


Figure 5.1: Simplification of coupling area into a free-end part of a beam

Then, we study the *changes on measured admittance* (ΔY) when the location and direction of the inputs and outputs (sensors/impacts) are varying, separately for two types of bending (vertical and lateral bending). Then we compare the changes on the modal value of VP and based on that error directions with higher sensitivity for each mode; shapes are introduced and summarized.

In the analysis of ΔY , we are considering the following questions:

- Does it matter in which direction we make a positional error on measuring equipment?
- How the main direction of the impact (or sensors) containing positional uncertainty affects the measurements?
- How distance between measure point to stand node can influence the uncertainty generation?

5.2.1. Error sensitivity as a function of error direction

Since the frequency response function can be described by the normal modes of the inputs and outputs (CMS method), we are interested in the changes in the normal mode of inputs and outputs when the position or direction of them is changing. Since the responses and modal values are frequency- and mode-shape-dependent, we are considering the effect of positional and directional uncertainty in different mode-shapes.

The following section investigates to explain the different sensitivity of impacts and sensors to positional and directional uncertainty and introduce the dominant error sources.

Figure.5.2 is an illustration of the first lateral and first vertical bending of our free-end beam. This part of the beam is considered to be the area between the end-node and the *first stand-node* (of that particular mode shape). We consider one impact at each surface of our free end part, impacts A, B, and C, in order to study the effect of the impact's primary direction.

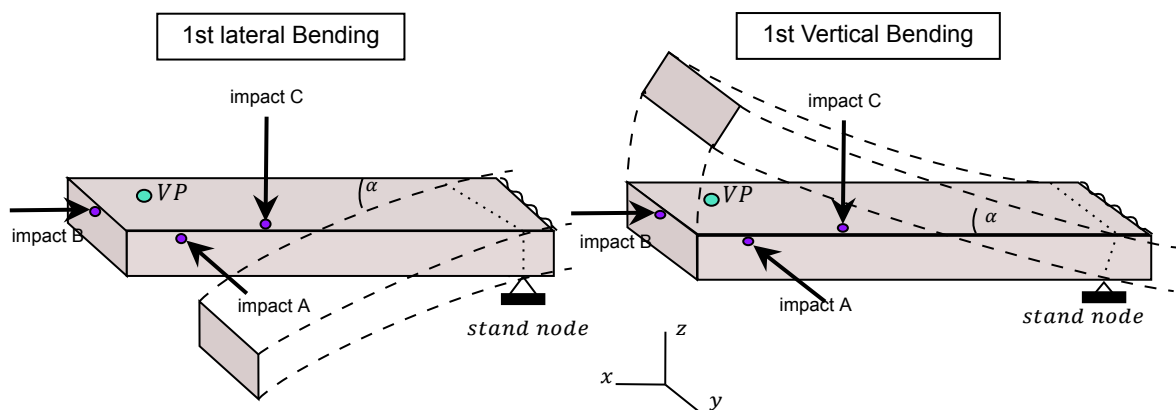


Figure 5.2: Deformation of beam in vertical bending and lateral bending. The dominant motion on vertical bending is along z-axes, and the dominant motion on lateral bending is along y-axes.

In order to mimic a positional uncertainty for an impact (or sensor), we consider two node x_1 and x_2 representing the *true* position and the *actual* position (with uncertainty), respectively. x_1 is in distance r_x , a_x , and δr_x from VP , stand-node, and node x_2 .

Vertical Bending

Figure.5.3 is a 2-D illustration of nodes x_2 and x_1 with their corresponding *modal value*, ϕ_{x1} and ϕ_{x2} , at first vertical bending (bending a motion along y axes).

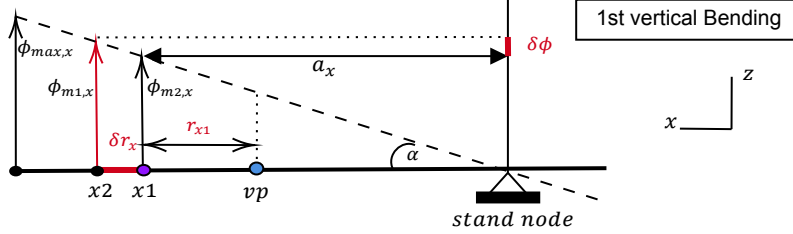


Figure 5.3: 1st mode-shape 2D

Since measuring equipment (inputs and outputs) acts and is mounted on the surface of the structure; its positional uncertainty could have components on two directions.

Figure.5.4 expands the model into a 3 – D model, in order to be able to introduce node x_3 , which is in distance δr_y (along y axes) from node x_1 . The amount of δr_x and δr_y are the same.

This figures compares the changes on modal values in the presence of positional uncertainty, where once x_1 is displaced along x axes to x_2 (Figure.5.4(a)), and Once displaced along y axes to x_3 (Figure.5.4(b)).

In Figure.5.4(a) a positional error along x axes will cause changes on the modal value (of z direction); however the same amount of positional along y will have no effect on the modal value.

We can conclude that the positional uncertainty of input or output has different directional sensitivity, which is mode-shape and frequency-dependent. It means that at each mode shape, the same amount of positional error does not introduce the same amount of changes on modal value.

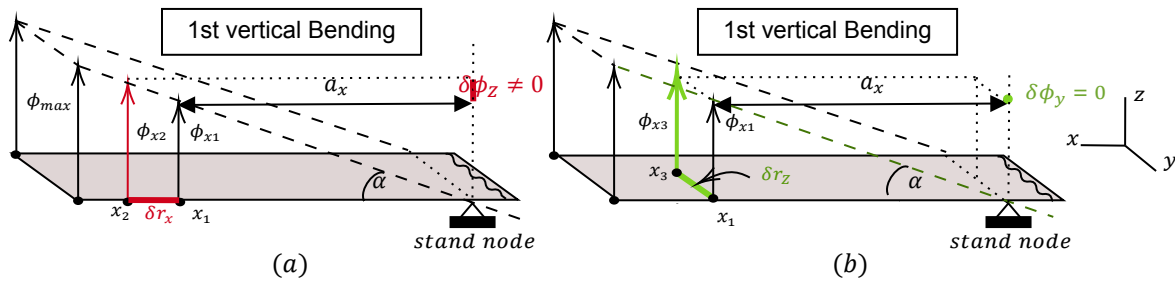


Figure 5.4: 2modes

As mentioned before the component mode synthesised method is one of the ways to compute the frequency response function, which uses the natural vibration modes. The admittance can be synthesised by the superposition of the natural modal solutions. The superposition of the admittance of input i to

output j , i.g. displacement over force reads as follows;

$$Y_{ij}(\omega) = \sum_{n=1}^k \frac{\phi_{i,n} \phi_{j,n}^T}{-\omega^2 + 2\zeta_n \omega \omega_n + \omega_n^2} \quad (5.1)$$

$$= \frac{\phi_{i,1}^1 \phi_{j,1}^1}{-\omega^2 + 2\zeta_1 \omega \omega_1 + \omega_1^2} + \frac{\phi_{i,2} \phi_{j,2}^T}{-\omega^2 + 2\zeta_2 \omega \omega_2 + \omega_2^2} + \dots + \frac{\phi_{i,k} \phi_{j,k}^T}{-\omega^2 + 2\zeta_k \omega \omega_k + \omega_k^2}$$

Where the r is the mode number, $\phi_{i,r}$ and $\phi_{j,r}$ are the modal value of nodes corresponds to input i and output j at mode number r .

This superposition means that each natural mode has a governing and dominant role in describing FRF around and especially at its natural frequency. As a matter of fact, changes on each of modal values ϕ_i or ϕ_j is just limited to that particular natural mode, and just change the frequency response function locally, at resonances corresponds to that natural mode. Now the question is that how the motion of structure at each mode shape can influence the changes of modal value corresponds to that mode shape.

In the previous section, we discussed that in the presence of uncertainty on the location of input or output, we record data that correspond to an additional node that differs from the true node. In the mode synthesized method, this dis-positioning is reflecting by replacing the modal value corresponds to the true position by the modal value corresponds to the measured position. Further, We have seen that the changes made on modal value are depending on the motion and mode shape. From this, we can expect that a certain error on position does not generate the same differences in other mode shapes, as the direction of displacement does not remain the same. It means that the changes in modal value $\phi_{i,r}$ is not the same for all natural modes r . Which results in different deviations of each natural mode. It means if we have some uncertainty on the position of input or output, we expect different deviation around each resonance, since the $\phi_{i,r}$ does not change the same for all mode shapes.

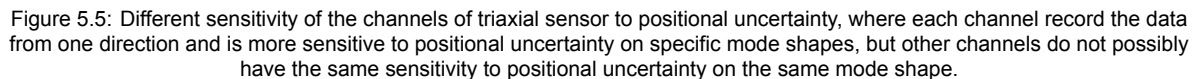
$$\Delta Y_{ij}(\omega) = \sum_{n=1}^k \frac{(\phi_{i-REF}^n - \phi_{i-with error}^n) \phi_j^n}{-\omega^2 + 2\zeta \omega_{rn} \omega + \omega_{rn}^2} = \sum_{n=1}^k \frac{(\delta \phi_i^n) \phi_j^n}{-\omega^2 + 2\zeta \omega_{r,n} \omega + \omega_{r,n}^2} \quad (5.2)$$

Since we are assuming that we accomplish the linearity assumption, the relation between $\delta \phi$, δr , $\phi_{measure}$, ϕ_{true} , a_x (changes on modal values, amount of error, measured response, true response, and distance to stand node can be written as follows:

$$\frac{\delta \phi}{\delta r} = \frac{\phi_{measure}}{a_x + \delta r} = \frac{\phi_{true}}{a_x} \quad (5.3)$$

Lateral Bending

Now we are considering another mode shape, *lateral bending*, of the same model (the free-end model which was illustrates on Figure.5.2), and applying the same positional errors on both possible directions, δr_x and δr_y .



In practice, people often use the triaccelerometers, which records the response of three perpendicular directions of the same node. It means that by having a positional error on sensor placement, depending on the mode shape, different channels may have different sensitivity to positional uncertainty. This is also shown on Figure.5.5

Since we need at least three impacts which each of them acts on one of the (local) directions, we need to know how the (main) direction of impact is influencing the changes on measured FRF if the input contains directional uncertainty.

Figure 1 consists of two schematic diagrams illustrating the experimental setup. (a) 3D view: A rectangular beam is shown with three impact points labeled A, B, and C. Impact B is at the left end, impact C is at the top surface, and impact A is at the bottom surface. A coordinate system (x, y, z) is shown at the bottom right, with the beam resting on a 'stand node'. The beam is labeled '1st lateral Bending'. (b) 2D view: A cross-section of the beam is shown. Impact B is at the left end, impact C is at the top surface, and impact A is at the bottom surface. A coordinate system (x, y) is shown at the bottom right, with the beam resting on a 'stand node'. The beam is labeled '1st lateral Bending'. The diagram shows the beam's deflection and the impact points relative to the beam's axis.

Figure 5.6: Lateral Bending.

Since in lateral bending (this part of) structure does not have any motion along z axes, the modal value corresponds to impact C is zero, and slightly changes on the position of this impact does not change its modal value.

Moreover, the modal value corresponds to impact B (for lateral bending) is very small, and the lightly changes in the position of impact B will cause minimal changes in modal value. However, these tiny changes on modal value are more when we have positional changes along y -axes than along x -axes.

5.2.3. FRF's error generation as a function of distance to stand node

In this section, we study the changes in the modal values as a function of mode-shape *number*. In the presence of positional uncertainty, the distance of the reference position of input or output to the *stand node* influences the amount of generated error, Equation. 5.3.

Figure.5.7 compares two situations, where both have the same *type* of mode shape, and the difference is on their *number* of mode shape, one illustrates the first vertical bending and the other one the second vertical bending. Again, r_x is the (dominant) positional error, and a_x is the distance from the measuring point to stand node corresponds to this mode shape.

When we are approaching higher *numbers* of a certain mode-shape, the distance of measure point to stand node, a_x , will change. It mean, a certain positional error δr_x on input (or output) do not cause the same changes (value) on the admittance for *different number* of a certain mode shape type.

If the measured point is still on the same side of stand node for different numbers of a mode shape, a certain amount of positional error δr_x will cause *higher error generation* on higher frequencies for the *higher number* of a particular mode shape.

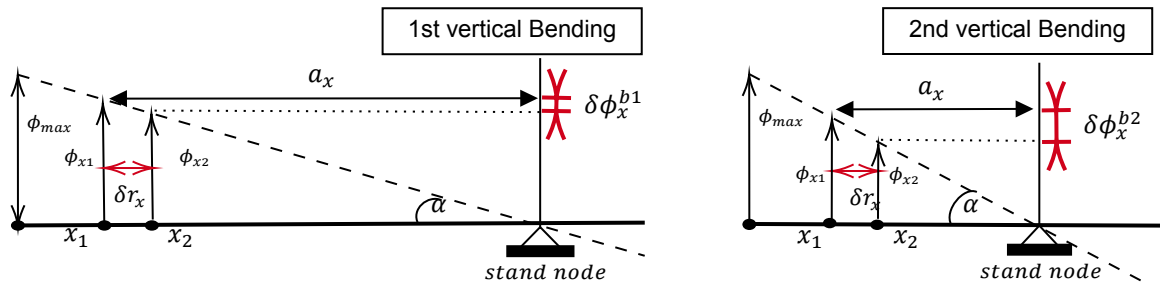


Figure 5.7: together-modeshapes

Figure.5.8 shows that the influence of the number of mode-shape on error generation is just valid for dominant positional error (in our example δr_x), and not for non-dominant error sources (in our example δr_y).

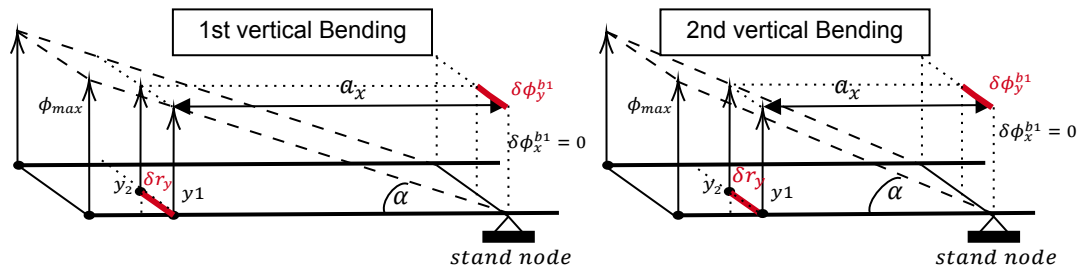


Figure 5.8: For non-dominant positional errors, the number of mode-shape does not influencing the error generation

5.2.4. Uncertainty propagation into VP's FRF

From the previous section, we have seen that how the direction of the uncertainty and the main direction of impact and distance to stand node are influencing the modal value and, consequently, on the measured FRF. In this section, we study; how the positional and directional errors propagate into Virtual Point admittance.

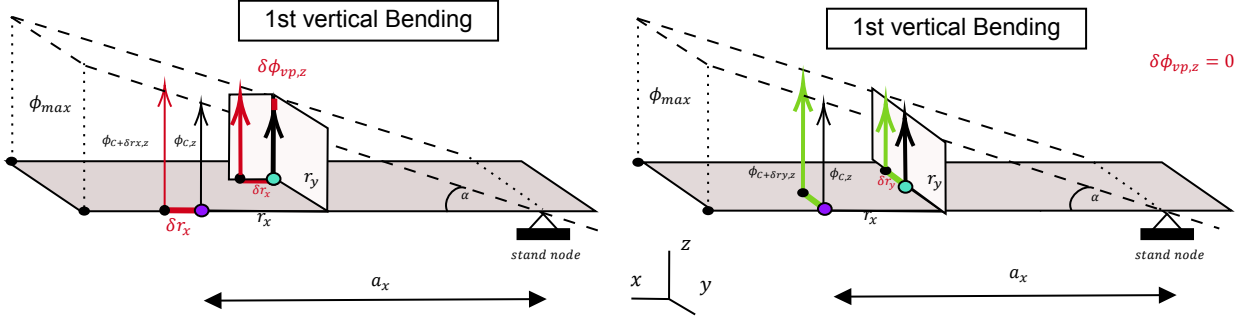


Figure 5.9: Mode shape and frequency dependency of VP

By assuming the linearity condition, the changes on modal value of inputs (impacts) or responses (sensors) are the same as the error generation on modal value of VP. With one difference, in the calculation of VP we actually average the positional errors of *all* inputs and *all* outputs.

Figure 5.10 illustrates the error generation during the projection, at the 1st vertical bending. This figure shows that in the presence of uncertainty on the position of input or output, the incorrect projection matrices will cause to calculate the FRF belongs to another point, which is in the distance δr_x of VP.

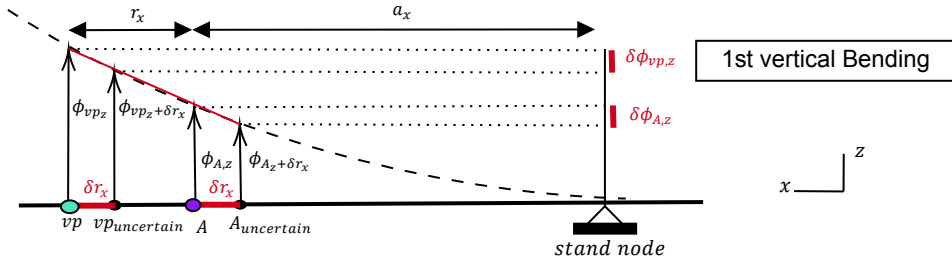


Figure 5.10: verticalBndingWithVP

Since the motion in the area of projection is assumed to be **linear**, and the amount of error on position of input (or output) and VP is the same ($\delta r_{x,A} = \delta r_{x,VP}$), the *amount of changes on modal values* of measured point A and VP are the same;

$$\delta \phi_{A,z} = \delta \phi_{VP,z} \quad (5.4)$$

This relation (same changes on the *amount* on modal value at measurement point and VP) is valid for *translational transformation*, and *does not* depending on the distance between measured position and Virtual Point, r_x , and their distance to stand node, a_x .

In short, the *placement* of inputs/outputs to VP does not have an influence on the amount of error propagation on translational transformation into VP's FRF, as long as they remain on the linear area.

5.2.5. Uncertainty propagation into VP's FRF, absolute value VS percentage value

Since the modal value of A and VP do not have the same value, $\phi_{A,z} \neq \phi_{VP,z}$, the **percentage changes** on their modal value (and consequently on FRF) is not the same.

$$\frac{\delta\phi_{A,z}}{\phi_{A,z}} \neq \frac{\delta\phi_{VP,z}}{\phi_{VP,z}} \quad (5.5)$$

The percentage changes on modal value of VP (which consequently affects its FRF), $P_{VP} = \frac{\delta\phi_{VP,z}}{\phi_{VP,z}}$, is surely depending on both r_x , a_x , and a_x , which are respectively the distance between measured point and VP , measured point to stand node, and VP to stand node.

- **Effect of r_x (distance between measure point and VP) on percentage modal changes of VP**

In a case both A and VP locating on the same side of stand node, higher the value on r_x (more distance between A and VP), higher the differences between the modal value of A and VP , which leads to higher the difference between the percentage changes on their modal values ($\Delta P = \frac{\delta\phi}{\phi}$).

$$\uparrow r_x \Rightarrow \uparrow \Delta P \quad \text{where} \quad \Delta P = P_{VP} - P_A = \frac{\delta\phi_{VP}}{\phi_{VP}} - \frac{\delta\phi_A}{\phi_A} \quad (5.6)$$

For example for a situation illustrates on Figure.5.10 (a positional error on input), the percentage changes on VP 's modal values (and consequently VP 's FRF) is smaller than the percentage changes on modal values of A ;

$$\frac{\delta\phi_{VP,z}}{\phi_{VP,z}} > \frac{\delta\phi_{A,z}}{\phi_{A,z}} \quad \text{where} \quad \begin{cases} \delta\phi_{VP,z} = \delta\phi_{A,z} \\ \phi_{A,z} < \phi_{VP,z} \\ \delta r_{x,A} = \delta r_{x,VP} \end{cases} \quad (5.7)$$

By increasing the distance between A and VP , r_x , the difference between the percentage changes on their modal values (ΔP) will be greater.

- **Effect of a_x (distance between measure point and a stand-node) on percentage modal changes of VP**

Consider a case where we move both VP and A towards the stand node (where still VP is in distance r_x of A). Figure.5.11 illustrates this situation when the structure is locally under vertical bending.

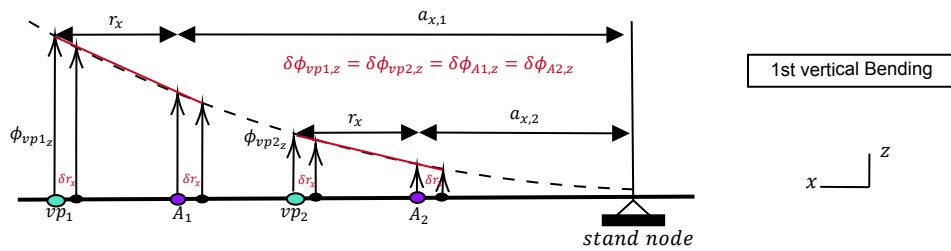


Figure 5.11: distance to Stand-node percentage Vertical Bending

Under the assumption of linearity for both set of measurement and VP , we obtain the percentage error generation for each Virtual Points, $P_{VP} = \frac{\delta\phi_{VP,z}}{\phi_{VP,z}}$. Comparing these two percentage changes shows:

$$\frac{P_{VP2}}{P_{VP1}} = \frac{\frac{\delta\phi_{VP2}}{\phi_{VP2}}}{\frac{\delta\phi_{VP1}}{\phi_{VP1}}} = \frac{\frac{\delta\phi_{VP2}}{a_{x2}+r_x}}{\frac{\delta\phi_{VP1}}{a_{x1}+r_x}} = \frac{a_{x1}+r_x}{a_{x2}+r_x} \quad \text{where} \quad \begin{cases} \frac{\phi_{VP2}}{\phi_{VP1}} = \frac{a_{x2}+r_x}{a_{x1}+r_x} \\ \delta\phi_{VP1} = \delta\phi_{VP2} \end{cases} \quad (5.8)$$

Since the measured point $A1$ is placed on a longer distance to stand-node than $A2$, $a_{x1} > a_{x2}$, the percentage error generated on $VP1$ (which is P_{VP1}) is higher than the percentage error generation for the same amount of positional error on $VP2$ (which is P_{VP2}).

$$P_{VP1} > P_{VP2} \quad \text{for} \quad a_{x1} > a_{x2} \quad (5.9)$$

• **Effect of b_x (distance between VP and stand node) on percentage modal changes of VP**

For more general form we write the relation between percentage errors P_{VP1} and P_{VP2} as a function of distance of these two Virtual Points to the stand-node corresponds to that mode shape, $b_{VP1,x}$ and $b_{VP2,x}$.

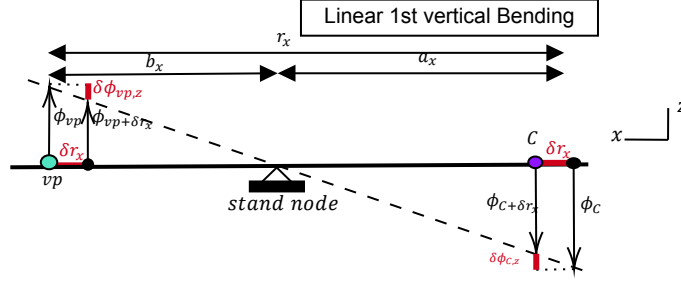


Figure 5.12: ax bx

This adjustment is made to give a more general form of how the distance between VP and stand-node plays a role on determination of percentage error generation on VP , regardless of the decision of putting the measured point A on the left-hand side of VP or on the right-hand side of that, as long as their distance r_x remains the same and both stay on linear regime. Then Equation.5.8 becomes as follow:

$$\frac{P_{VP2}}{P_{VP1}} = \frac{\frac{\delta\phi_{VP2}}{\phi_{VP2}}}{\frac{\delta\phi_{VP1}}{\phi_{VP1}}} = \frac{b_{x1}}{b_{x2}} \quad \text{where} \quad \begin{cases} r_{x1} = r_{x2} \\ b_x = a_x \pm r_x \end{cases} \quad (5.10)$$

It means, for a set of measurement points and VP , and for a certain type of mode shape, on *higher number of a mode shape type*, we have a reduction on the $b_{x,VP}$. And, based on Equation.5.10 we expect less percentage error on VP (P_{VP}) for higher number of that type of mode shape.

$$\uparrow b_x \Rightarrow \uparrow P_{VP} \quad (5.11)$$

5.2.6. Non-linearity and uncertainty propagation to VP 's FRF

In theory, if we accomplish the linearity assumption, the r_x (distance between the uncertain measurement point and VP) does not influence the amount of generated error on translational cross-functions of VP , at its *absolute value*. (The effect of this uncertainty on rotational cross-functions is the subject of next sections).

Absolute error

In case of local nonlinearity (on the region where the measuring equipment and VP are placed), the generated error (on its absolute value) on modal value $\delta\phi$ for both A and VP are not anymore the same, left figure of Figure.5.13.

Since we need to be sure measuring equipment and VP are placed on the linear region; it is a good practice to locate the measurement equipment as close as possible to VP , minimizing r_x , to make sure that we accomplish the linearity assumption.

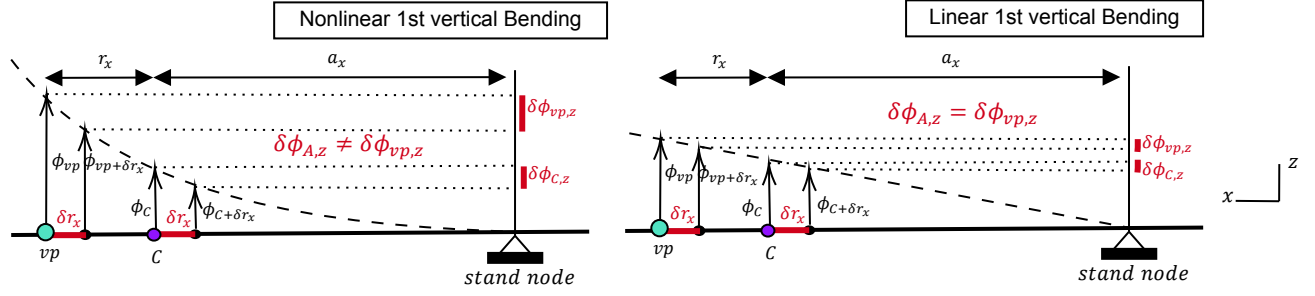


Figure 5.13: nonlinear deflection

Percentage error

As discussed before, locating the measuring equipment close to the VP (in order to decrease the r_x , r_y and r_z) will *not* change the generated error on the VP 's FRF in both *percentage value* and in *absolute value*, for transnational DoFs.

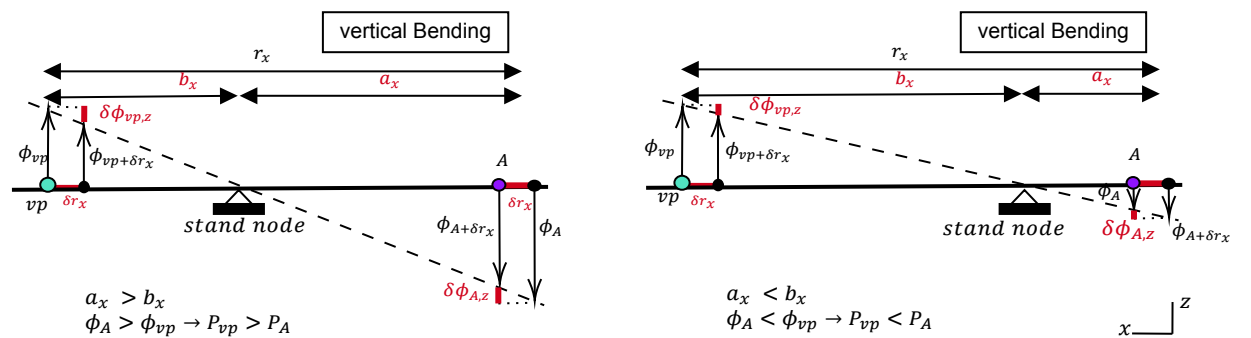
If we are not on the linear regime, then the calculated FRF at VP is much smaller than the real values at that point. Also, the amount of error generation in nonlinear regime in a real case is much higher than the linear case. It means, in nonlinear regime, the error propagation is higher than the linear regime for both absolute and percentage values.

In non-linear regime, as long as $b_{VP,x}$ (distance between VP and stand node) is smaller than a_x , the generated percentage error on VP (P_{VP}) is smaller than the measurement point.

5.2.7. Relation of a_x and b_x and their influence on P_{VP}

The relation between a_x and b_x is also influencing the *percentage* error propagation to Virtual Point. a_x and b_x are representing the distance of measure point to stand-node for a certain mode shape and the distance of VP to stand-node, respectively. Figure.5.14 summarizes these relations and their affects on the error propagation.

This figure concludes that if the VP is closer to the stand node than the measure point ($b_x < a_x$), then the percentage error generation on modal value of VP is bigger than the measure point ($P_{vp} > P_A$), left illustration of Figure.5.14. And, if the measure point is closer to the stand node than the VP , then the percentage error generation on VP is smaller than the percentage error generation in an experiment, right illustration of Figure.5.14.

Figure 5.14: Relation a_x and b_x and their influence on *percentage* error on VP (P_{VP}), unless they are on the same side of stand-node or not

Guide line: If it is possible, place VP more close to stand node (than the measured point to stand node)

to reduce the percentage error.

5.2.8. Positional Uncertainty: Mode shape and frequency dependency of error propagation into VP

In this section, we consider two bending types, vertical- and lateral bending, in order to define the impacts directions and uncertainty directions with a dominant effect on error propagation into VP . First, we consider the locational error and then the directional error.

Vertical Bending and locational uncertainty

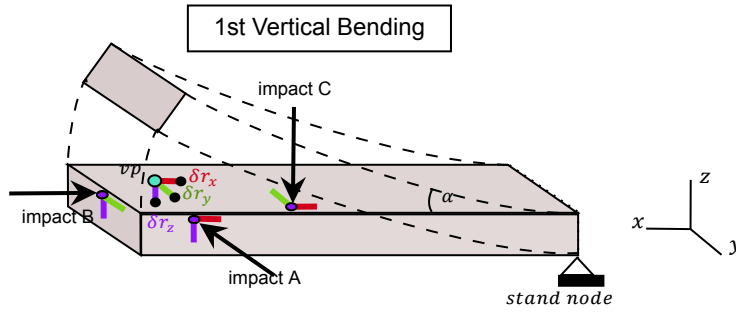


Figure 5.15: Mode shape and frequency dependency of VP at its vertical bending

Figure.5.9 illustrates all projection errors on vertical bending. A rough estimation on the generated uncertainty on modal values of Virtual Point $\delta\phi_{VP}$ caused by each error direction δr read as follow:

$$\delta r_{x,VP} : \begin{cases} \delta\phi_{z,VP} \neq 0 \\ \delta\phi_{x,VP} \approx 0 \\ \delta\phi_{y,VP} = 0 \end{cases} \quad \delta r_{y,VP} : \begin{cases} \delta\phi_{z,VP} = 0 \\ \delta\phi_{x,VP} \approx 0 \\ \delta\phi_{y,VP} = 0 \end{cases} \quad \delta r_{z,VP} : \begin{cases} \delta\phi_{z,VP} = 0 \\ \delta\phi_{x,VP} \approx 0 \\ \delta\phi_{y,VP} = 0 \end{cases} \quad (5.12)$$

At and around frequencies corresponds to *vertical bending* (according to coordinate choice of this study), the VP is more sensitive to errors which cause the highest changes on modal value of z direction (which is in the same direction as vertical bending), which here is δr_x .

Lateral Bending and locational uncertainty

Figure.5.16 illustrates a Lateral Bending of the same free-end beam, and looked to the changes on modal values of VP at this mode shape.

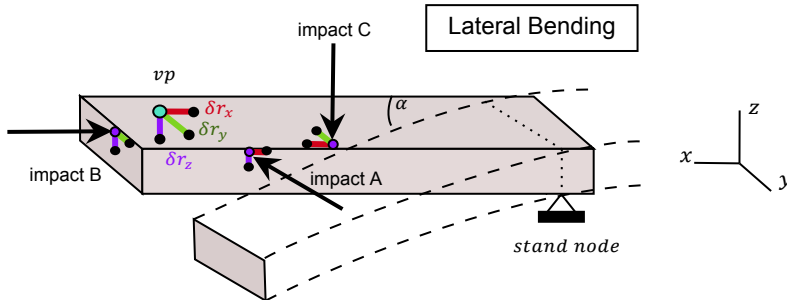


Figure 5.16: Lateral Bending of a free-end beam, changes of modal value of VP

Again, a rough estimation on the changes on the modal value of VP , $\delta\phi_{VP}$, caused by different (positional) error direction δr_{VP} is as follows:

$$\delta r_{x,VP} : \begin{cases} \delta\phi_{z,VP} = 0 \\ \delta\phi_{x,VP} \approx 0 \\ \delta\phi_{y,VP} \neq 0 \end{cases} \quad \delta r_{y,VP} : \begin{cases} \delta\phi_{z,VP} = 0 \\ \delta\phi_{x,VP} \approx 0 \\ \delta\phi_{y,VP} = 0 \end{cases} \quad \delta r_{z,VP} : \begin{cases} \delta\phi_{z,VP} = 0 \\ \delta\phi_{x,VP} \approx 0 \\ \delta\phi_{y,VP} = 0 \end{cases} \quad (5.13)$$

At and around frequencies corresponds to *Lateral bending* (again, according to coordinate choice of this study), the VP is also more sensitive to errors on x direction δr_x . However, this error direction causes the highest changes on the modal value of y direction (which is in the same direction as Lateral bending).

5.2.9. Positional uncertainty; Error in the estimation of VP 's forces and responses

In the presence of positional uncertainty of an impact or a sensor, we will have deviation(s) on the relative distance between the measured point and VP (comparing with true measurement). If we do not adjust this deviation on the transformation matrices R , then we will project the measured data into a point which is not VP , which we call it $VP_{uncertain}$.

In this section we compare the *true transformation* matrix, R_{true} , with *uncertain transformation* matrix, $R_{uncertain}$, in order to calculate the deviation on the calculation of forces, (δF_{VP}), and moments (δM_{VP}) (or translational (δu_{VP}) and rotational responses ($\delta\theta_{VP}$)) between VP_{true} and $VP_{uncertain}$.

Consider positional uncertainty δr_x , since we have shown that this positional uncertainty (PU) is a *dominant positional error source* (for both lateral and vertical bending).

In our example (Figure.5.2) two impacts A and C can include this positional uncertainty. Figure.5.17 illustrates these errors and the amount of error in force and moments they generate.

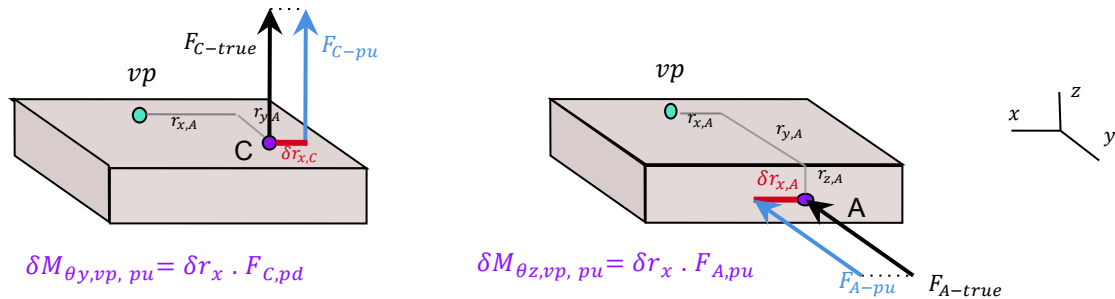


Figure 5.17: Impacts with possibility to contain positional uncertainty (PU) along x axes are dominant error source for both vertical and lateral bending. These impacts have highest sensitivity to positional error along x axes, and the amount of the error they generate is depending on the impact direction and the amount of error δr_x .

For more general estimation of error generation, we calculate the δR . Recall the relation between measured responses (u) and transformed responses to VP (q):

$$u = R_u q + \mu = [e_u^T \quad (r_u \times e_u)^T] q + \mu \quad (5.14)$$

In order to see the changes on transformation matrix, we add uncertainty δr_x to the relative distances vector r_u , and compare the transformation matrices.

$$\delta R_u = R_{uncertain} - R_{true} \quad (5.15)$$

Since we assume that the linearity assumption is accomplished, the residual is considered to be zero ($\mu = 0$). The deviated response between VP and $VP_{uncertain}$ is obtained by calculating the δR_u^{-1} :

$$\delta \mathbf{R}_u^{-1} = \frac{1}{\delta r_x} \begin{bmatrix} 0 & 0 & 0 \\ 0 & 0 & 0 \\ 0 & 0 & 0 \\ -\sin\theta_y & \cos\theta_y \sin\theta_x & -\cos\theta_x \cos\theta_y \\ -\cos\theta_y \sin\theta_z & \cos\theta_x \cos\theta_z - \sin\theta_x \sin\theta_y \sin\theta_z & \cos\theta_z \sin\theta_x + \cos\theta_x \sin\theta_y \sin\theta_z \end{bmatrix} \quad (5.16)$$

Based on Equation.5.16 we can write our expectation of the changes on translational and rotational responses at VP , when the dominant positional error sources δr_x is present :

$$\text{Translational: } \begin{cases} \delta q_{x,VP} = 0 \\ \delta q_{y,VP} = 0 \\ \delta q_{z,VP} = 0 \end{cases} \quad \text{Rotational: } \begin{cases} \delta q_{\theta_x,VP} = 0 \\ \delta q_{\theta_y,VP} = \frac{u_x \sin\theta_y - u_y (\cos\theta_y \sin\theta_x) - u_z (\cos\theta_x \cos\theta_y)}{\delta r_x} \\ \delta q_{\theta_z,VP} = \frac{-u_x (\cos\theta_y \sin\theta_z) + u_y (\cos\theta_x \cos\theta_z - \sin\theta_x \sin\theta_y \sin\theta_z) + u_z (\cos\theta_z \sin\theta_x + \cos\theta_x \sin\theta_y \sin\theta_z)}{\delta r_x} \end{cases}$$

In the case that the sensor is perfectly aligned with VP ($\theta_x = 0, \theta_y = 0$ and $\theta_z = 0$), the positional uncertainty of measured point (PU) will cause no changes on the VP 's forces. However, it changes the calculated rotational responses, $\delta q_{\theta_y,VP}$ and $\delta q_{\theta_z,VP}$.

$$\delta \mathbf{R}_u^{-1} = \begin{bmatrix} 0 & 0 & 0 \\ 0 & 0 & 0 \\ 0 & 0 & 0 \\ 0 & 0 & -1/\delta r_x \\ 0 & -1/\delta r_x & 0 \end{bmatrix} \Rightarrow \begin{bmatrix} \delta q_x \\ \delta q_y \\ \delta q_z \\ \delta q_{\theta_x} \\ \delta q_{\theta_y} \\ \delta q_{\theta_z} \end{bmatrix} = \begin{bmatrix} 0 & 0 & 0 \\ 0 & 0 & 0 \\ 0 & 0 & 0 \\ 0 & 0 & -1/\delta r_x \\ 0 & -1/\delta r_x & 0 \end{bmatrix} \begin{bmatrix} \delta u_x \\ \delta u_y \\ \delta u_z \\ \delta u_{\theta_x} \\ \delta u_{\theta_y} \\ \delta u_{\theta_z} \end{bmatrix} \quad (5.17)$$

Table.5.1 shows the error generation on VP 's responses, for both vertical- and lateral bending, for dominant positional error source δr_x .

Table 5.1: Properties and dimensions of the substructure

Mode-shape	Error type	Dominant error source	Response direction	$\delta \mathbf{q}_{VP}$	=	$\mathbf{q}_{VP} - \mathbf{q}_{VP,PU}$
vertical-lateral bending	positional	δr_x	Z	$\delta \mathbf{q}_{z,VP}^{PU, \delta r_x}$	=	$[0 \ 0 \ 0 \ 0 \ \delta u_z / \delta r_x \ 0]^T$
vertical-lateral bending	positional	δr_x	X	$\delta \mathbf{q}_{x,VP}^{PU, \delta r_x}$	=	$[0 \ 0 \ 0 \ 0 \ 0 \ 0]^T$
vertical-lateral bending	positional	δr_x	Y	$\delta \mathbf{q}_{y,VP}^{PU, \delta r_x}$	=	$[0 \ 0 \ 0 \ 0 \ 0 \ \delta u_y / \delta r_x]^T$

Where $\mathbf{q}_{VP,PU}$ denotes the vector containing the translational and rotational response at VP in the presence of positional uncertainty PU .

We can conclude from Table.5.6 that, in the presence of positional errors on sensors, more significant the response u_y or u_z , the less amount of error generation on VP 's, for both absolute and percentage value!

Positional Uncertainty on Impacts

We recall the relation between the inputs(forces), denotes by $\mathbf{f} = [f_x \ f_y \ f_z]^T$ in Cartesian coordinate system, force transformation matrix \mathbf{R}_f , and forces and moments at Virtual Point \mathbf{m}_{VP} , for both *true* and *uncertain* positioning of input (for dominant positional error source δr_x).

$$\mathbf{m}_{VP} = \mathbf{R}_f^T \mathbf{f} = \begin{bmatrix} \mathbf{e} \\ [\mathbf{r} \times \mathbf{e}] \end{bmatrix} \mathbf{f} \quad , \quad \mathbf{m}_{VP,uncertain} = \mathbf{R}_f^T \mathbf{f} = \begin{bmatrix} \mathbf{e} \\ [(r_x + \delta r_x) \ r_y \ r_z] \times \mathbf{e} \end{bmatrix} \begin{bmatrix} f_x \\ f_y \\ f_z \end{bmatrix} \quad (5.18)$$

Again, *changes on the force transformation matrix* $\delta \mathbf{R}_f^T$ gives us the amount of generated error on the calculation of forces and moments of *VP*.

$$\delta \mathbf{R}_f^T = \delta r_x \begin{bmatrix} 0 & 0 & 0 \\ 0 & 0 & 0 \\ 0 & 0 & 0 \\ 0 & 0 & 0 \\ -\sin\theta_y & \cos\theta_y \sin\theta_x & -\cos\theta_x \cos\theta_y \\ -\cos\theta_y \sin\theta_z & \cos\theta_x \cos\theta_z - \sin\theta_x \sin\theta_y \sin\theta_z & \cos\theta_z \sin\theta_x + \cos\theta_x \sin\theta_y \sin\theta_z \end{bmatrix} \quad (5.19)$$

The changes on the *VP*'s forces and moments reads as follow:

$$\text{Forces: } \begin{cases} \delta m_{x,VP} = 0 \\ \delta m_{y,VP} = 0 \\ \delta m_{z,VP} = 0 \end{cases} \quad \text{Moments: } \begin{cases} \delta m_{\theta_x,VP} = 0 \\ \delta m_{\theta_y,VP} = -f_x \sin\theta_y + f_y (\cos\theta_y \sin\theta_x) - f_z (\cos\theta_x \cos\theta_y) \\ \delta m_{\theta_z,VP} = -f_x \cos\theta_y \sin\theta_z + f_y (\cos\theta_x \cos\theta_z - \sin\theta_x \sin\theta_y \sin\theta_z) + f_z (\cos\theta_z \sin\theta_x + \cos\theta_x \sin\theta_y \sin\theta_z) \end{cases}$$

As we expected, the *VP*'s forces are not prone to positional uncertainty of inputs (impacts). The amount of the changes on the moments (δM_y and δM_z) is depending on the direction of the impact (F_x, F_y or F_z) and its relative angle to *VP* (θ_x, θ_y or θ_z).

In case of directional alignment of impacts with *VP*, ($\theta_x = \theta_y = \theta_z = 0$), the error generation on *VP*'s moments by dominant error direction for each impact is shown on Table.5.2.

For example, for impact *C* which acts along *z* axes ($f_x = f_y = 0$) and has high sensitivity to positional uncertainty along *x* axes, we will expect an error generation on moments around *y* axes, with amount of $\delta M_y = \delta r_x f_z$. By comparing the projection matrix we can see what is the influence of changing the position of each impact on *VP*.

Table 5.2: Properties and dimensions of the substructure

Mode-shape	Error type	Dominant error source	Impact	Force direction	$\delta \mathbf{m}_{VP}^{PU, \delta r_x} = \mathbf{m}_{VP} - \delta \mathbf{m}_{VP}^{PU, \delta r_x}$
vertical-lateral bending	positional	δr_x	C	$F_C = f_{C,z}$ $f_{C,x} = 0, f_{C,y} = 0$	$\delta \mathbf{m}_{z,VP}^{PU, \delta r_x} = [0 \ 0 \ 0 \ 0 \ \delta r_x \cdot f_z \ 0]^T$
vertical-lateral bending	positional	δr_x	B	$F_B = f_{B,x}$ $f_{B,y} = 0, f_{B,z} = 0$	$\delta \mathbf{m}_{x,VP}^{PU, \delta r_x} = [0 \ 0 \ 0 \ 0 \ 0 \ 0]^T$
vertical-lateral bending	positional	δr_x	A	$F_A = f_{A,y}$ $f_{A,x} = 0, f_{A,z} = 0$	$\delta \mathbf{m}_{y,VP}^{PU, \delta r_x} = [0 \ 0 \ 0 \ 0 \ 0 \ -\delta r_x \cdot f_y]^T$

5.2.10. Directional Uncertainty

In this section, we consider the directional uncertainty of measuring equipment, in order to find the dominant error sources for each mode shape and the amount of generated error on the forces and responses (rotational and translational) of Virtual Point.

Figure.5.18 illustrates a part of structure under (local) vertical bending, where impacts *A*, *B* and *C* contain directional uncertainties. The directional uncertainty of each impact is decomposed of two components. For example, directional uncertainties for impact *C* (which its *true direction* is along *z* axes) could be:

- Rotating around *y* axes, by the amount of $\delta \theta_y$, which causes a reduction on the contribution of force on *z* direction, and (instead) exciting the structure also on *x* direction.
- Rotating around *x* axes, by the amount of $\delta \theta_x$, which leads to exciting the structure also on *y* axes, and reducing the portion of force on *z* direction.

We expect that each directional error which leads to a contribution of force or responses with the same direction as the dominant motion of mode shape, becomes a significant error contributor at- and around

frequencies corresponds to that type of mode shape.

We also expect to observe some spurious peaks on some FRFs, where *directional* errors on measuring equipment made them able to measure some motions of other DoFs.

Vertical Bending and directional uncertainty

In our example, on (local) vertical bending, the dominant motion is along z direction, and all the nodes have significantly higher modal value in this direction. Modal value of other directions are significantly lower and are almost the same ($\phi_x \approx \phi_y$):

$$\phi_x \approx \phi_y \ll \phi_z \quad (5.20)$$

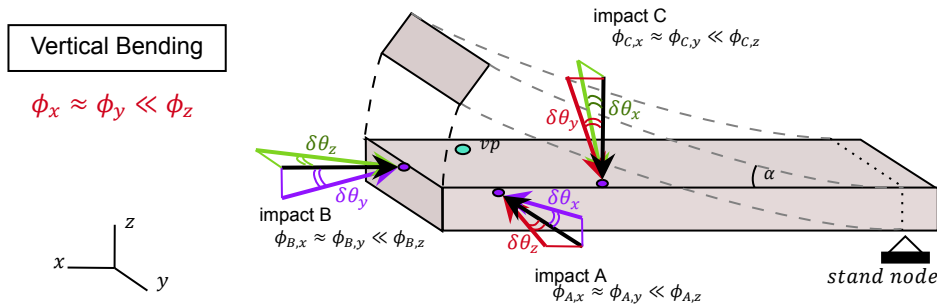


Figure 5.18: vertical Bending UD

Since dominant motion at this vertical bending is on z direction, any error which leads to a contribution of force at z direction becomes a significant error contributor at and around frequencies corresponds to this type of mode shape.

Impacts A and B are able to contain some directional uncertainty which leads to the contribution of forces on z direction. This directional errors are due to error $\delta\theta_x$ on impact A , and $\delta\theta_y$ on impact B .

Table 5.3: Estimation of error generation, in order to find dominant *directional errors* and their *corresponding true directions*, for vertical bending

mode shape	impact	direction of error	modal value changes (approximation)
Vertical Bending	C	$\delta\theta_x$	$\delta\phi_{C,z} = 0$
		$\delta\theta_y$	$\delta\phi_{C,z} \approx 0$
Vertical Bending	B	$\delta\theta_z$	$\delta\phi_{B,x} = 0$
		$\delta\theta_y$	$\delta\phi_{B,x} \neq 0$
Vertical Bending	A	$\delta\theta_z$	$\delta\phi_{A,y} \approx 0$
		$\delta\theta_x$	$\delta\phi_{A,y} \neq 0$

Lateral Bending and directional uncertainty

We take the same procedure for lateral bending, in order to find the impacts with dominant directional error for frequencies at- and around resonances correspond to this type of mode shape.

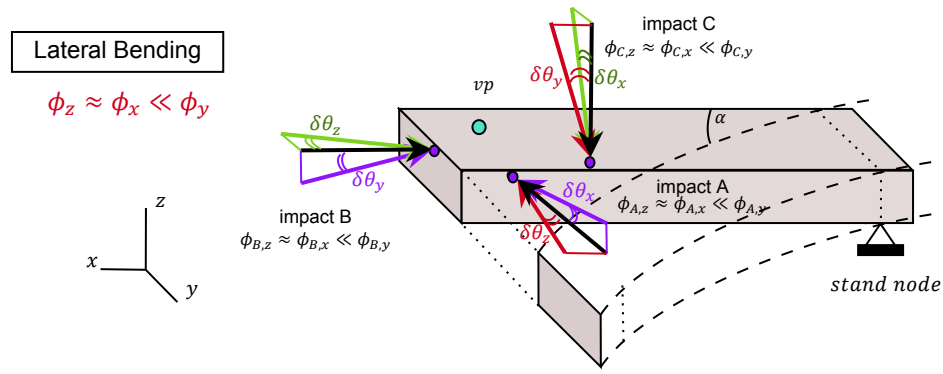


Figure 5.19: Lateralbending UD

Table.5.4 indicates (in red) the directional error sources ($\delta\theta$) with dominant effect on changing (or partially replacing) the modal value for each impact (true) direction. Directional uncertainty (DU) on impact *C* caused by rotation of this impact around its *x* axes, and DU in impact *B* caused by rotation of this impact around its *z* axes, are the dominant error sources, for this lateral bending.

Table 5.4: Properties and dimensions of the substructure

mode shape	impact	direction of error	modal value changes (approximation)
Lateral Bending	C	$\delta\theta_x$	$\delta\phi_{C,z} \neq 0$
		$\delta\theta_y$	$\delta\phi_{C,z} \approx 0$
Lateral Bending	B	$\delta\theta_z$	$\delta\phi_{B,x} \neq 0$
		$\delta\theta_y$	$\delta\phi_{B,x} = 0$
Lateral Bending	A	$\delta\theta_z$	$\delta\phi_{A,y} \approx 0$
		$\delta\theta_x$	$\delta\phi_{A,y} = 0$

5.2.11. Propagation of Directional Uncertainty into *VP*

In the previous section, we have seen that impacts with different main directions have different sensitivity to directional error. Moreover, if a directional uncertainty causes a contribution of force (or sensor) on the same direction as the direction of the mode shape motion, then this direction for uncertainty is a highly sensitive direction for error generation for that specific mode shape, at- and around frequencies of resonance correspond to that mode shape.

Figure.5.20 illustrates the dominant directional error sources for both vertical bending and lateral bending.

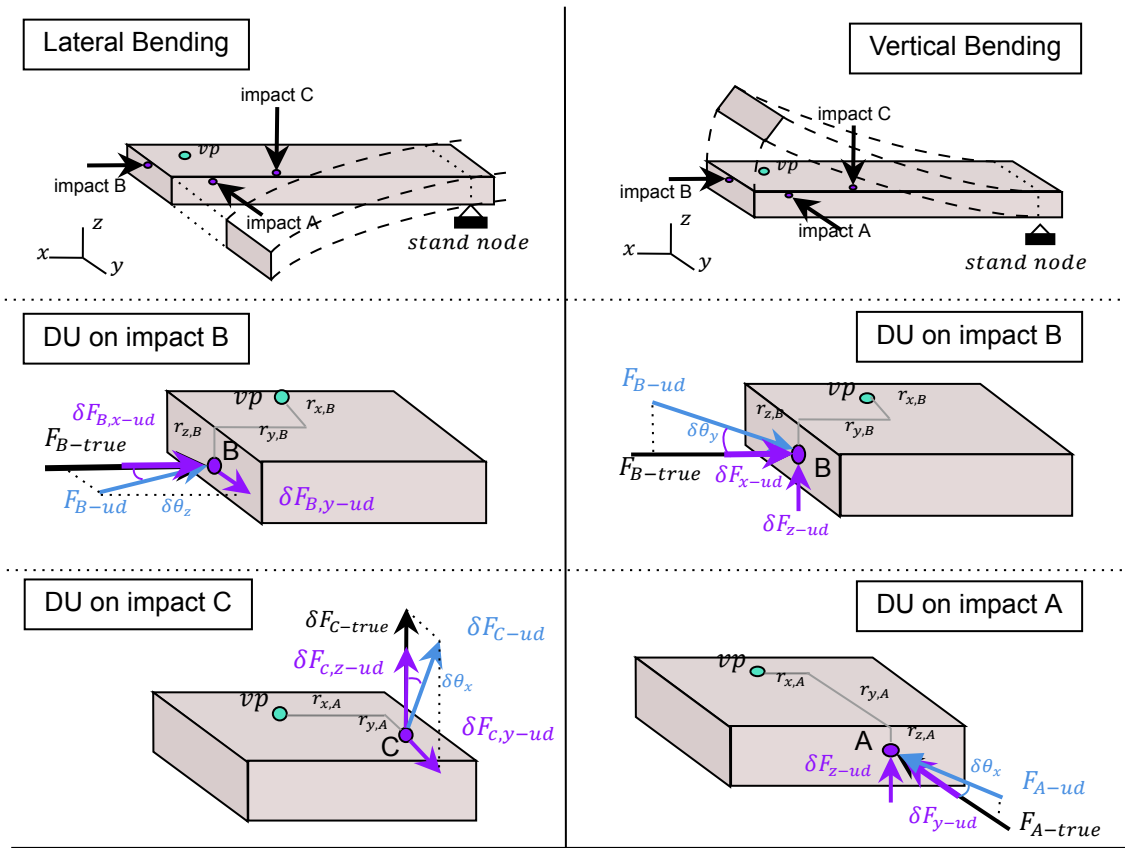


Figure 5.20: Vertical Bending

Figure 5.21: Dominant directional error sources for vertical and lateral bending, the (true) direction of each the impacts is aligned with one of the VP's DoFs

Table 5.5: Dominant *directional* error sources for lateral bending and vertical bending, and how each error will affect the direction of excitation, when measuring equipment and VP coordinates are aligned

mode shape	direction of error	modal value changes (approximation) and replacing by other values
Vertical Bending	$\delta\theta_{VP,y}$	$\delta\phi_{VP,z} = 0$ $\delta\phi_{VP,x} \neq 0$
Vertical Bending	$\delta\theta_{VP,z}$	$\delta\phi_{VP,y} \approx 0$ $\delta\phi_{VP,x} \approx 0$
Vertical Bending	$\delta\theta_{VP,x}$	$\delta\phi_{VP,z} = 0$ $\delta\phi_{VP,y} \neq 0$
Lateral Bending	$\delta\theta_{VP,y}$	$\delta\phi_{VP,z} \neq 0$ $\delta\phi_{VP,x} \neq 0$
Lateral Bending	$\delta\theta_{VP,z}$	$\delta\phi_{VP,y} = 0$ $\delta\phi_{VP,x} \neq 0$
Lateral Bending	$\delta\theta_{VP,x}$	$\delta\phi_{VP,z} \neq 0$ $\delta\phi_{VP,y} \approx 0$

Forces and Responses of VP, in the presence of DU, vertical bending

The supposed direction of impact *B* is along *x* axes. In the presence of directional uncertainty on this impact towards *z* direction, we will excite the structure on *z* direction. The amount of the contribution of the response of *z* direction depends on the amount of directional error, in this case, $\delta\theta_{B,z}$

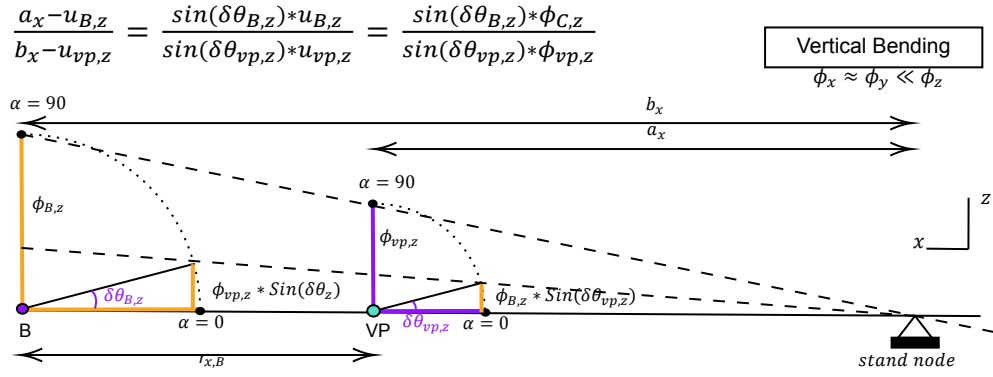


Figure 5.22: vertical bending UD 2D impact B delta theta_z

Now, the question is how the directional error (generated during a measurement) makes changes on the (calculated) FRF of VP . For answering this question, we consider two kinds of mode shape, vertical and lateral bending, separately, we chose an impact and a directional error with high sensitivity to directional error, and then we go through the transformation and the calculation of the FRF of VP .

$$\delta \mathbf{R}_u^T = \mathbf{R}_{u,uncertain}^T - \mathbf{R}_{u,true}^T \quad (5.21)$$

In the presence of directional uncertainty, to calculate the *true transformation matrix* we need to adjust the *Eulerian rotational matrix* in the transformation matrix.

For example, if we have directional uncertainty $\delta \theta_y$, and want to obtain the correct transformation matrix we need to adjust the rotational matrix corresponds to y axes on Eulerian rotation matrix, $\mathbf{R}_y(\beta)$, by replacing the β with $\delta \theta_y + \beta$. in this case the transformation matrix becomes:

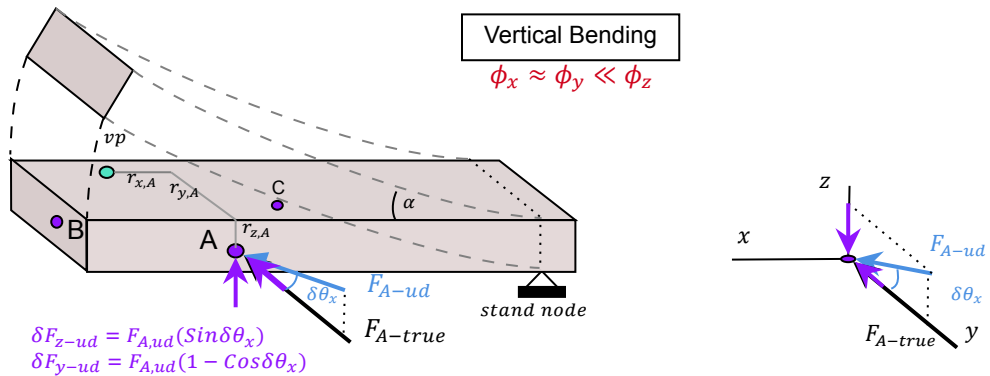
$$\mathbf{R}_u^{kv} = \mathbf{T}_u^{kv-1} = \begin{bmatrix} (\mathbf{r}^{kv} \times \mathbf{E}_{true}^{kv})^T \\ \mathbf{E}_{true}^{kvT} \end{bmatrix} = \quad \text{where} \quad \mathbf{E}_{true} = \mathbf{R}_z(\alpha) \mathbf{R}_y(\beta + \delta \theta_y) \mathbf{R}_x(\gamma) \quad (5.22)$$

Recall the relation between the forces on measured point and the forces and moments on VP :

$$\left. \begin{aligned} \mathbf{m}_{VP,true} &= \mathbf{R}_{f,true}^T \cdot \mathbf{f}_{meas} \\ \mathbf{m}_{VP,uncertain} &= \mathbf{R}_{f,uncertain}^T \cdot \mathbf{f}_{meas} \end{aligned} \right\} \Rightarrow \delta \mathbf{m}_{VP} = \delta \mathbf{R}^T \cdot \mathbf{f}_{meas}$$

The $\delta \mathbf{R}_f$ gives us the chance to track the changes on forces and moments of VP ($\delta \mathbf{m}$).

On vertical bending impact A with directional error on $\delta \theta_x$ is one of the dominant error sources.

Figure 5.23: UD vertical bending impact A $\delta \theta_x$

In order to obtain the $\delta \mathbf{R}_f$, we substitute the $\gamma + \delta \theta_x$ on rotational matrix around x axes (\mathbf{R}_x) of Equation

5.22, to obtain $R_{u,true}$ and then compare it with $R_{uncertain}$.

$$\delta R_f = \begin{bmatrix} 0 & 0,0 & \\ 0 & \cos(\delta\theta_x) - 1 & -\sin(\delta\theta_x) \\ 0 & \sin(\delta\theta_x) & \cos(\delta\theta_x) - 1 \\ 0 & r_z(1 - \cos(\delta\theta_x)) + r_y \cdot \sin(\delta\theta_x) & r_y(\cos(\delta\theta_x) - 1) + r_z \cdot \sin(\delta\theta_x) \\ 0 & -r_x \cdot \sin(\delta\theta_x) & r_x(1 - \cos(\delta\theta_x)) \\ 0 & r_x \cdot \cos(\delta\theta_x) - r_x & -r_x \cdot \sin(\delta\theta_x) \end{bmatrix} \approx \begin{bmatrix} 0 & 0 & 0 \\ 0 & 0 & \delta\theta_x \\ 0 & \delta\theta_x & 0 \\ 0 & \delta\theta_x \cdot r_y & \delta\theta_x \cdot r_z \\ 0 & -\delta\theta_x \cdot r_x & 0 \\ 0 & 0 & -\delta\theta_x \cdot r_x \end{bmatrix} \quad (5.23)$$

Since force of impact A has a true direction along y axes, we take the second column of δR to calculate the changes on the forces and the moments of VP in the presence of directional error $\delta\theta_x$ for impact A are becoming as follow:

$$\delta m_{VP} = (\delta R_{f(y \rightarrow y + \delta\theta_x)}^{A,VP})^T \cdot \begin{bmatrix} f_{x,A} \\ f_{y,A} \\ f_{z,A} \end{bmatrix}$$

$$\text{forces A: } \begin{cases} \delta f_{x,VP}^{DU,\delta\theta_x} = 0 \\ \delta f_{y,VP}^{DU,\delta\theta_x} = -F_y \cdot (1 - \cos\delta\theta_x) \\ \delta f_{z,VP}^{DU,\delta\theta_x} = -F_y \cdot \sin\delta\theta_x \end{cases} \quad \text{Moments: } \begin{cases} \delta M_{\theta_x,VP}^{DU,\delta\theta_x} = F_y [r_y \cdot \sin\delta\theta_x + r_z(1 - \cos\delta\theta_x)] \\ \delta M_{\theta_y,VP}^{DU,\delta\theta_x} = r_x \cdot F_y \cdot \sin(\delta\theta_x) \\ \delta M_{\theta_z,VP}^{DU,\delta\theta_x} = -r_x \cdot F_y \cdot (1 - \cos\delta\theta_x) \end{cases} \quad (5.24)$$

The same procedure is taken for another dominant directional error sources for both vertical bending and lateral bending, see Appendix.A.

Figure.5.24 illustrates and summarizes all dominant error sources, for both positional uncertainty and directional uncertainty, for both vertical- and lateral bending.

Table.5.2.11 gives the changes on the calculation of Virtual Point forces, moments, translational- and rotational response, for dominant error sources of each mode-shape (by indicating the dominant error direction) for both positional and directional uncertainties.

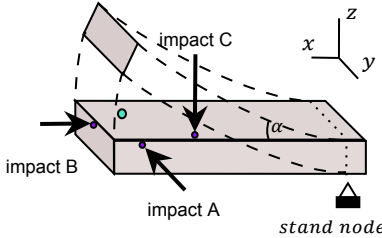
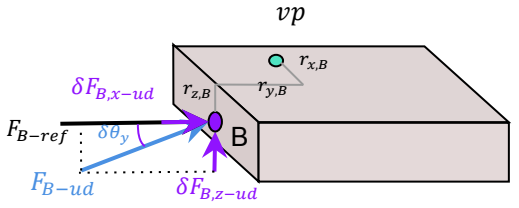
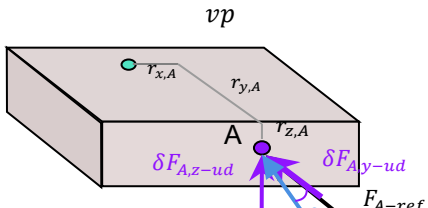
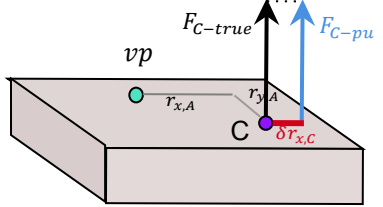
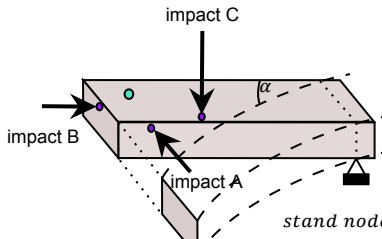
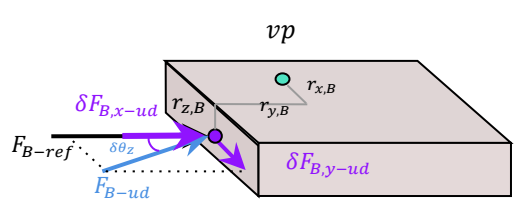
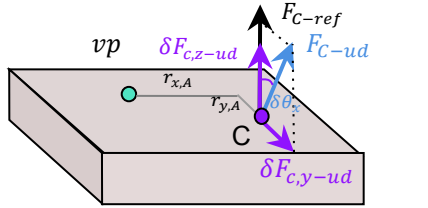
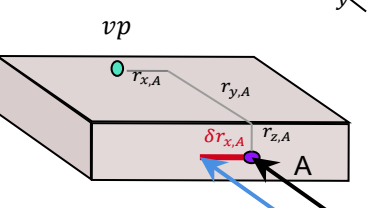
Mode Shape	Dominant error sources Directional Uncertainty		Positional Uncertainty
<p data-bbox="369 432 562 464">Vertical Bending</p> 	 $\delta F_{z-ud} = F_{B,ud}(\sin \delta \theta_y)$ $\delta F_{x-ud} = F_{B,ud}(1 - \cos \delta \theta_y)$	 $\delta F_{z-ud} = F_{A,ud}(\sin \delta \theta_x)$ $\delta F_{y-ud} = F_{A,ud}(1 - \cos \delta \theta_x)$	 $\delta M_{\theta y, vp, pu} = \delta r_x \cdot F_{C,pu}$
<p data-bbox="369 858 562 890">Lateral Bending</p> 	 $\delta F_{B,x-ud} = F_{C,ud}(1 - \cos \delta \theta_z)$ $\delta F_{B,y-ud} = F_{C,ud}(\sin \delta \theta_z)$	 $\delta F_{C,z-ud} = F_{C,ud}(1 - \cos \delta \theta_x)$ $\delta F_{C,y-ud} = F_{C,ud}(\sin \delta \theta_x)$	 $\delta M_{\theta z, vp, pu} = \delta r_x \cdot F_{A,pu}$

Figure 5.24: all errors illustration V2

Table 5.6: Dominant error sources and their influence on the calculation of vp

Bending	error type	Force	Dominant error	$\delta f_{x,vp}$	$\delta f_{y,vp}$	$\delta f_{z,vp}$	$\delta M_{\theta_x,vp}$	$\delta M_{\theta_y,vp}$	$\delta M_{\theta_z,vp}$	5.2. Analytical approach
Lateral	DU	$F_{B,x}$	$\delta\theta_z$	$-F_x(1 - \cos\delta\theta_z)$	$F_x.\sin\delta\theta_z$	0	$-F_x.r_z.\sin\delta\theta_z$	$F_x.r_z(1 - \cos\delta\theta_z)$	$F_x[r_y.(1 - \cos\delta\theta_z) + r_y.\sin\delta\theta_z]$	
Lateral	DU	$F_{C,z}$	$\delta\theta_x$	0	$-F_z(\sin\delta\theta_x)$	$F_z.(1 - \cos\delta\theta_x)$	$-F_z[r_y.(1 - \cos\delta\theta_x) + r_z.\sin\delta\theta_x]$	$F_z.r_x.(1 - \cos\delta\theta_x)$	$F_z.r_x(\sin\delta\theta_x)$	
Vertical	DU	$F_{B,x}$	$\delta\theta_y$	$-F_x.(1 - \cos\delta\theta_y)$	0	$-F_x.\sin\delta\theta_y$	$F_x.r_y.\sin\delta\theta_y$	$F_x[r_x.\sin(\delta\theta_y) - r_z(1 - \cos\delta\theta_y)]$	$-F_x.r_y.(1 - \cos\delta\theta_y)$	
Vertical	DU	$F_{A,y}$	$\delta\theta_x$	0	$-F_y.(1 - \cos\delta\theta_x)$	$-F_y.\sin\delta\theta_x$	$F_y[r_y.\sin\delta\theta_x + r_z(1 - \cos\delta\theta_x)]$	$r_x.F_y.\sin(\delta\theta_x)$	$-r_x.F_y(1 - \cos\delta\theta_x)$	
Vertical Lateral	PU	$F_{A,y}$	δr_x	0	0	0	0	0	$-\delta r_x.F_y$	
Vertical Lateral	PU	$F_{C,z}$	δr_x	0	0	0	0	$\delta r_x.F_z$	0	
	error type	Sensor	error	$\delta u_{x,vp}$	$\delta u_{y,vp}$	$\delta u_{z,vp}$	$\delta\theta_{x,vp}$	$\delta\theta_{y,vp}$	$\delta\theta_{z,vp}$	67
Vertical	DU	u_y	$\delta\theta_x$	0	$\frac{-(u_y)(r_y.r_z)}{\delta\theta_x(r_x^2+1)(r_x^2+r_y^2+r_z^2+1)}$	$\frac{-(u_y)(r_x^2+r_z^2+1)}{\delta\theta_x(r_x^2+1)(r_x^2+r_y^2+r_z^2+1)}$	$\frac{-(u_y)(r_y)}{\delta\theta_x(r_x^2+1)(r_x^2+r_y^2+r_z^2+1)}$	$\frac{-(u_y)(r_x)(r_x^2+r_z^2+1)}{\delta\theta_x(r_x^2+1)(r_x^2+r_y^2+r_z^2+1)}$	$\frac{(u_y)(r_x.r_y.r_z)}{\delta\theta_x(r_x^2+1)(r_x^2+r_y^2+r_z^2+1)}$	
Vertical	DU	u_x	$\delta\theta_y$	$\frac{(u_x)(r_x.r_z)}{\delta\theta_y(r_y^2+1)(r_x^2+r_y^2+r_z^2+1)}$	0	$\frac{(u_x)(r_y^2+r_z^2+1)}{\delta\theta_y(r_y^2+1)(r_x^2+r_y^2+r_z^2+1)}$	$\frac{(u_x)(r_y)(r_y^2+r_z^2+1)}{\delta\theta_y(r_y^2+1)(r_x^2+r_y^2+r_z^2+1)}$	$\frac{-(u_x)r_x}{\delta\theta_y(r_y^2+1)(r_x^2+r_y^2+r_z^2+1)}$	$\frac{(u_x)(r_x.r_y.r_z)}{\delta\theta_y(r_y^2+1)(r_x^2+r_y^2+r_z^2+1)}$	
Lateral	DU	u_z	$\delta\theta_x$	0	$\frac{(u_z)(r_x^2+r_y^2+1)}{\delta\theta_x(r_x^2+1)(r_x^2+r_y^2+r_z^2+1)}$	$\frac{(u_z)(r_z.r_y)}{\delta\theta_x(r_x^2+1)(r_x^2+r_y^2+r_z^2+1)}$	$\frac{(u_z)r_z}{\delta\theta_x(r_x^2+1)(r_x^2+r_y^2+r_z^2+1)}$	$\frac{-(u_z)(r_z.r_y)}{\delta\theta_x(r_x^2+1)(r_x^2+r_y^2+r_z^2+1)}$	$\frac{(u_z)(r_x)(r_x^2+r_y^2+1)}{\delta\theta_x(r_x^2+1)(r_x^2+r_y^2+r_z^2+1)}$	
Lateral	DU	u_x	$\delta\theta_z$	$\frac{-(u_x)(r_x.r_y)}{\delta\theta_z(r_z^2+1)(r_x^2+r_y^2+r_z^2+1)}$	$\frac{-(u_x)(r_y^2+r_z^2+1)}{\delta\theta_z(r_z^2+1)(r_x^2+r_y^2+r_z^2+1)}$	0	$\frac{(u_x)(r_z)(r_y^2+r_z^2+1)}{\delta\theta_z(r_z^2+1)(r_x^2+r_y^2+r_z^2+1)}$	$\frac{-(u_x)(r_y.r_z.r_x)}{\delta\theta_z(r_z^2+1)(r_x^2+r_y^2+r_z^2+1)}$	$\frac{-(u_x)r_x}{\delta\theta_z(r_z^2+1)(r_x^2+r_y^2+r_z^2+1)}$	
Vertical Lateral	PU	u_y	δr_x	0	0	0	0	0	$\frac{F_z}{\delta r_x}$	
Vertical Lateral	PU	u_z	δr_x	0	0	0	0	$\frac{-F_y}{\delta r_x}$	0	

5.3. FEM approach on an asymmetric structure (modal based) model

An asymmetric, complex modal based model (FEM) is used to study the *"propagation of directional and locational uncertainty on impacts and sensors to the calculation of VP"*, shown on Figure.5.25. The presented structure is considered to examine the correctness of *dominant error source corresponds to each mode shape*, which was discussed on the analytical approach in the previous chapter.

This structure has two legs and contains several holes to be able to couple to another structure. The head of one of these legs contains a hole, and this hole is chosen to be the coupling point. As a single coupling point, a 6Dofs Virtual Point (VP) is defined, which is placed exactly in the center of the hole. To determine the FRF for this VP, three accelerometers, and 13 impacts are placed on different surfaces around the hole, as closed as possible to the chosen VP.

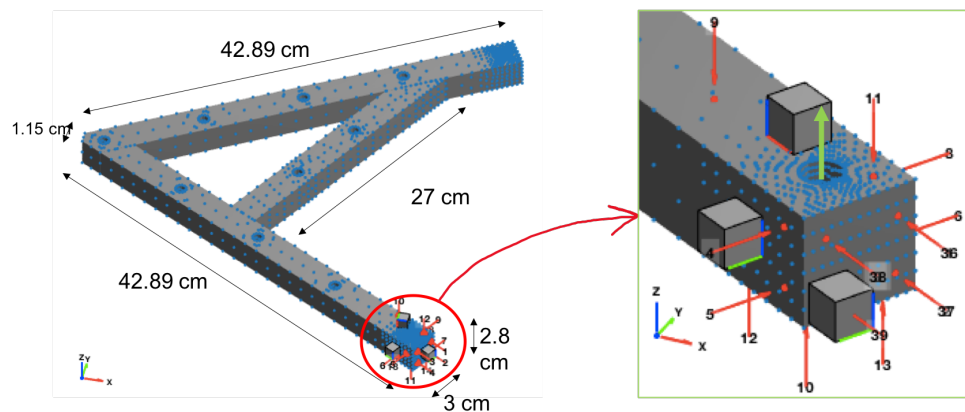


Figure 5.25: An asymmetric structure with one coupling point. The 3 sensors and 13 impacts are shown in gray cubs and red arrows, respectively. The Virtual Point DsFs are illustrated as green arrows centered in the hole of coupling point

Table 5.7: Properties and dimensions of the asymmetric substructure

substructure physical dimensions		
size		42.89x2.8x3 cm
weight		6.8530 kg
Substructure FE modeling		
Material density		2.7 g/cm ³
Young's modulus		70 GPa
number of nodes		8004
number of DOFs		24012
Simulated experimental setup		
sensors	type	triaxial accelerometers
	number of sensors	3
	sensors DOFs	9: 3X, 3Y, 3Z
excitation tool	type	impact hammer
	number of impacts	13
	impacts DOFs	13x1 = 13
Virtual Point	VP displacement DOFs	3 translational + 3 rotational
	VP force and moment DOFs	3 translational + 3 rotational

The free-free model of the asymmetric structure is made on ANSYS (properties are given on Table.5.7); further the \mathbf{M} and the \mathbf{K} matrices of the model are extracted and then imported to MATLAB. By using these two matrices, the eigenfrequencies and corresponding eigenvectors are calculated. By knowing the eigenvectors of each DoF of the system, we can select the eigenvalues of DoFs corresponding to

each sensor and each impact.

The modal synthesized frequency response function $Y_{i,j}(\omega)$ between each sensor's channel i and each impact j can be made by using the eigenfrequencies (ω_n), eigen-parameters ϕ_i and ϕ_j (modal vector corresponds to each impact j and sensor's channel i) and the modal damping parameter ζ .

We are assuming a constant modal damping parameter for all frequencies equal to $\zeta = 0.004$. This value is found from literature (which itself is extracted from experimental data for that chosen material) [35].

$$Y_{i,j}(\omega) = \sum_{r=1}^n \frac{\phi_{i,r} \phi_{j,r}}{-\omega^2 + 2\zeta\omega\omega_r + \omega_r^2} \quad (5.25)$$

Having 3 triaxial-accelerometers and 13 impacts get us 9 DoFs from sensors and 13 DoFs from impacts. The corresponding frequency response function ($Y_{i,j}(\omega)$) between all impacts and sensors *at each frequency* becomes a 9x13 matrix.

Knowing the *relative distance* and *relative angle* between VP and each sensor and each impact, the displacement projection matrix T_u (a 6x9 matrix) and a force projection matrix T_f^T (a 13x6 matrix) are set up. These projection matrices are used to transform the (numerically) measured FRF ($Y_{i,j}(\omega)$) to VP 's FRF ($Y_{VP}(\omega)$).

$$Y_{VP}(\omega) = T_u Y_{i,j}(\omega) T_f^T \quad (5.26)$$

The VP 's FRF is a frequency response function between all 6 DoFs (translational and rotational) forces and 6 DoFs (translational and rotational) responses of the coupling point.

5.3.1. Tracking the dominant *directional error source* for each mode shape

To track the dominant directional error source, each time a *single directional error* was applied on possible impacts, and then the frequency response function ($Y_{uncertain}$) was numerically computed. This uncertain FRF was compared (element-wise) with the true FRF (Y_{true}) to obtain the generated measurement error ΔY , which was caused by a specific uncertainty.

Then the deviated FRF, ΔY , (caused by a single directional uncertainty) was studied for type of mode shape.

The mode shape type is defined based on the type of the structure's motion at each resonance. For asymmetric model illustrated on Figure.5.25 the mode shapes are divided into four groups; 1)lateral bending, 2)vertical bending, 3)torsion and 4)mixed motions, which are presented on Table.6.1.

Table 5.8: Mode shapes and their corresponding resonances, for asymmetric model illustrated on Figure.5.25

Mode Shape	Dominant motion's direction	resonances [Hz]		
Lateral Bending	y	442	1647	2334
Vertical Bending	z	596		
Torsion	x,y	816	2583	
Torsion+Vertical bending	x,y+z	1340	1953	2145

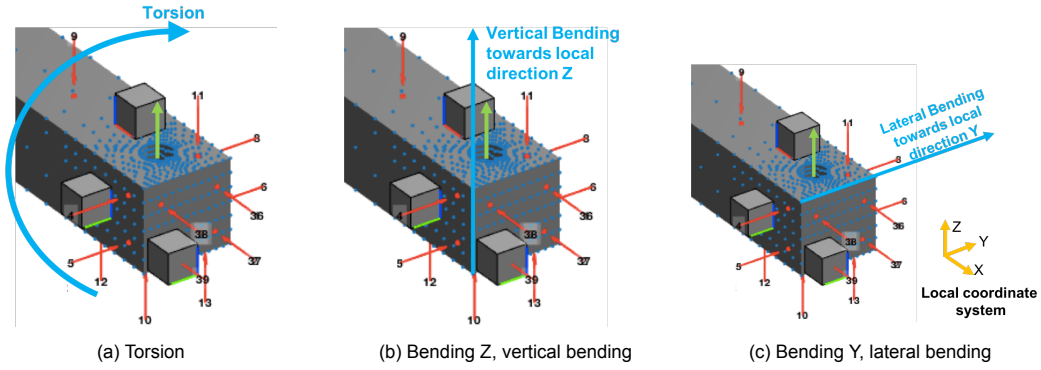


Figure 5.26: The type of the motions for each mode-shape group.

In order to *find the dominant directional error source for each mode shape*, we compare the ΔY s caused by different directional uncertainties *at specific frequency* (frequency which corresponds to that mode shape).

we decide to use *Heatmaps* to compare the absolute value of different entries of (deviation on) admittance, ΔY , at a specific frequency. A heatmap numerically and visually (by shades of a color) compares the values of a matrix. In our case, at each frequency, the $\Delta Y_{measure}$ is a 9×13 matrix and ΔY_{VP} is a 6×6 matrix. By using a heatmap we can see which impacts and in which extend cause a greater error and deviation on FRF (at a specific frequency).

The results from this numerical approach is presented on next chapter (chapter.6)

5.4. Monte Carlo simulation on an asymmetric structure (modal based) model

The most straightforward way to study the effect of uncertainty is through Monte Carlo Simulation [43]. A Monte Carlo simulation is used on our modal based asymmetric substructure (FEM) to simulate the propagation of directional and locational uncertainty on impacts and sensors to the calculation of VP . Monte Carlo is a computational algorithm that relies on repeated random sampling. In order to systematically generating errors, the following steps are taken:

1. Define the domain of possible input:

The varied variables in this thesis are as follows (wherein each simulation just one of these variables is changing).

- Sensors' Position (SP)
- Sensors' Direction (Orientation) (SD)
- Impacts' Position (IP)
- Impacts' Direction (Orientation) (ID)

2. Define the value of error on each case:

In the case of varying impacts' or sensors' positions, we defined a value equal to 1 mm (for each possible direction), where the center of sensor or the contact point of impact hammer with structure can vary around its true position, in each possible direction.

In the case of directional uncertainty, the amount of error on each direction is 5° .

3. Generate error vector:

- **Impacts'/sensors' Position (IP, SP):** To bring uncertainty on the location of sensors, each time, all sensors will move by error vectors around their true position. The error vector for each sensor is independent, and its components are generated randomly within a *defined value of error*. The component of the error vector is generated independently in all directions. As each sensor mounted on a surface, it can move in just 2 directions, as a matter of fact

the error vector has 2 non-zero values, $\Delta r = [\delta r_x \ \delta r_y \ \delta r_z]$. The error vector further will be multiplied by the rotation matrix to go from local coordinate to global coordinate. Then the sensor was moved from its true position by error vector. The same procedure is applied for bringing positional uncertainty on impacts.

- **Impacts'/sensors' direction (ID, SD):** To bring directional uncertainty on impact, first a directional error vector was generated, where its elements are randomly and independently are defined within a certain directional error value. Then this error vector was multiplied by impacts rotational matrix, to get the directional error vector on global coordinate which is become $\Delta \theta_{impact(i)} = [\delta \theta_{x(i)} \ \delta \theta_{y(i)} \ \delta \theta_{z(i)}]$. Further the direction of the impact is changed to $\theta_{impact(i)} = [\theta_{x(i)} + \delta \theta_{x(i)} \ \theta_{y(i)} + \delta \theta_{y(i)} \ \theta_{z(i)} + \delta \theta_{z(i)}]$. The same procedure is applied for bringing directional uncertainty on sensors.
4. **Calculating FRF (Y)**, mapping the cross-function between sensors and impacts where impacts or sensors have new location or new direction.
 5. **Calculating FRF at VP** ($Y_{VP} = T_u Y T_f^T$): we can calculate two VP's FRF, $Y_{certain}$ and $Y_{uncertain}$.
 - **$Y_{certain}$: Calculating VP's FRF with accurate transformation matrices T_u and T_f** means that at each run, the projection matrices are adopted with a new direction or orientation (of impacts) and will be changed at each run. It is not a surprise that using the actual projection matrices gives exactly the same VP's FRFs for all runs (illustrated in Figure.??).
 - **$Y_{uncertain}$: Calculating VP's FRF with a fixed T_u and T_f** , gives FRFs which are deviating from each other (illustrated on Figure.??). since we are trying to mimic the experiment, and obtaining the true experiment is almost impossible, we will never know the actual position and direction of sensors and impacts. For this reason, we fix the projection matrices T_u and T_f on the calculation of VP's FRF.

Results and Discussion

This thesis uses analytical and numerical approaches to study the effect of sensors and impacts' positional and directional uncertainty on the measurement and their influence on the VP ' frequency response function.

Previous chapter introduced these approaches. Further, the analytical analysis has done on a small part of a beam with a free. Component Mode Synthesised method is used to make expectations of the dominant error sources. Moreover, the previous chapter introduced an asymmetrical FEM model. Also, the Monte Carlo simulation is described.

This chapter studies an introduced asymmetric modal based model to investigate a numerical verification of the mode shape- and frequency-dependency of the uncertainty propagation to the VP 's FRF, caused by directional and locational uncertainty on impacts or sensors.

This chapter is split into two parts, Results and discussion. The results part presents the results from the 1)FEM approach and 2)Monte Carlo simulation. In the Discussion part, the results of two numerical approaches are compared and discussed, and further, a comparison is made between the numerical results and analytical expectations.

based on analytical analysis, two extreme cases are introduced. In one scenario, the maximum error generation is introduced, where all the errors are adding to each other. The second scenario describes a case where errors of different sources cancel each other.

6.1. Results 1: FEM, A Complex Modal Based Model

This chapter contains the numerical results of the IDU case (impacts directional uncertainty) on our asymmetric modal-based model (this FEM model is introduced in the previous chapter, and illustrated in Figure.5.25). Further, the VP 's cross-functions containing the highest propagated error are considered. For the results of other cases see Appendix.F, Appendix.C, Appendix.H.

Since we expect that the IDU error generation and its propagation to VP is mode shape- and frequency-dependent, we decide to study the propagated error to VP 's FRFs at resonances, in order to find the impacts with dominant error generation for each type of motion (mode shape). In the discussion part, we compare these numerical results with expectations from an analytical approach.

As discussed in previous chapter, the type of mode shape is defined based on the type of the structure's motion at each resonance. For our asymmetric model, the mode shapes are divided into four groups; 1)lateral bending, 2)vertical bending, 3)torsion and 4)mixed motions, which are presented on Table.6.1.

Table 6.1: Mode shapes and their corresponding resonances, for asymmetric model illustrated on Figure.5.25

Mode Shape	Dominant motion's direction	resonances [Hz]		
Lateral Bending	y	442	1647	2334
Vertical Bending	z	596		
Torsion	x,y	816	2583	
Torsion+Vertical bending	$(x,y)+z$	1340	1953	2145

To track the dominant directional error source, each time a *single directional error* was applied on possible impacts, and then the frequency response function ($\mathbf{Y}_{uncertain}$) was numerically computed. This uncertain FRF was compared (element-wise) with the true FRF (\mathbf{Y}_{true}) to obtain the generated measurement error $\Delta\mathbf{Y}$, which was caused by a specific uncertainty.

Then the deviated FRF, $\Delta\mathbf{Y}$, (caused by a single directional uncertainty) was studied for type of mode shape.

Dominant motion-direction of this FEM model at lateral bending is in y -direction. The first, second, and third Lateral bending happens at 443, 1648, and 2335 [Hz].

Without any directional uncertainty Impacts 1-3 excite the structure along x -direction, Impacts 4-8 excite the structure along y -direction and Impacts 9-13 excite the structure along z -direction.

we decide to use *Heatmaps* to compare the absolute value of different entries of (deviation on) admittance, $\Delta\mathbf{Y}$, at a specific frequency. A heatmap numerically and visually (by shades of a color) compares the values of a matrix. In our case, at each frequency, the $\Delta\mathbf{Y}_{measure}$ is a 9x13 matrix and $\Delta\mathbf{Y}_{vp}$ is a 6x6 matrix. By using a heatmap, we can see which impacts and, in which extend, cause a greater error and deviation on FRF (at a specific frequency).

6.1.1. Measured FRF: Mode shape- and frequency-dependent dominant error sources

Figure.6.1 considers the changes in measured FRFs at first, second, and third lateral bending (at 443, 1648 and 2335 [Hz]), in the presence of directional uncertainty. Every column of this figure shows the heatmap of *absolute value* of the deviation of measured FRF with its true value, $\Delta\mathbf{Y}_{measure}$, when a single directional error is applied on the (possible) impacts.

In this figure, column(a) represents the cases where impacts 1-4 and 9-13 have directional deviation on their primary direction, which causes that these impacts excite the structure also on y -direction. Column(b) is the case where impacts 4-8 and 9-13 have directional deviation, which causes these impacts to apply force also on x -direction. In Column(c), impacts 1-3 and 4-8 have directional deviation causes exciting the structure also on z -direction. Column(d) where all impacts 1-3, 4-8, and 9-13 have directional uncertainty on all possible directions. The amount of directional error in all cases is 5 degree.

In order to find the impacts with dominant (directional) errors, we compare the FRF's heatmap of all lateral bendings of the case (d) (all impacts have all directional errors) with other cases (with single directional error). We observe that at lateral bending (with a mode-shape motion on y -direction), any directional uncertainty which causes exciting the structure in the same direction as the mode shape motion-direction (y -direction) causes the most significant error and becomes a dominant error source, which is column(a).

In the presence of directional uncertainty, the error which leads to exciting the structure in the same direction as the mode shape motion-direction (here is y -direction) generates the most error significantly. This confirms the expectations from analytical analysis.

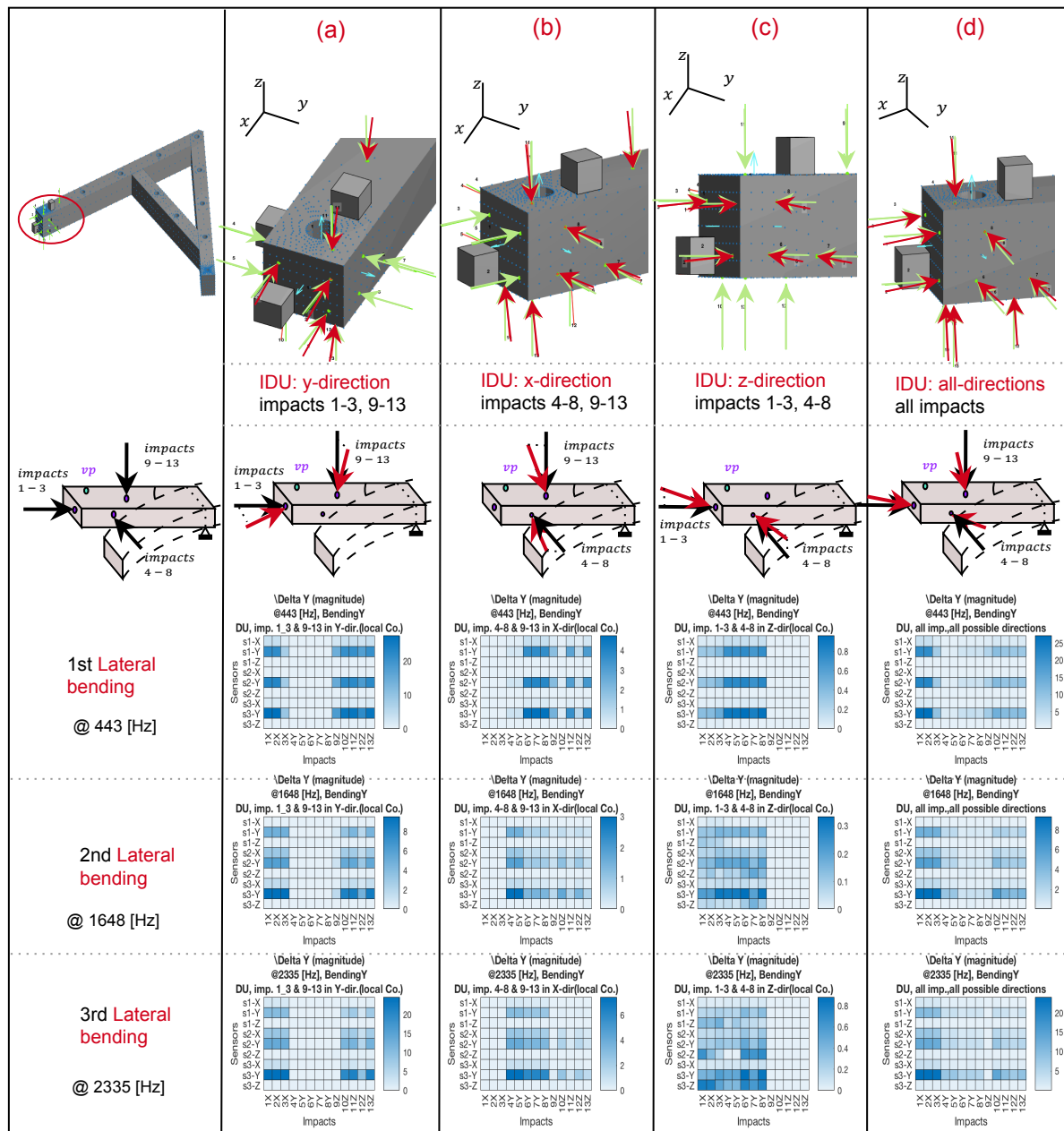


Figure 6.1: Dominant directional error source in lateral bending. The absolute value of ΔY at resonances with lateral bending motion, where error sources are as follows: single directional errors on column (a), (b), and (c), and (d) where all impacts have all possible error directions. Comparing the FRF's heatmap of all lateral bendings and case (d) with other cases (with single directional error) shows that at lateral bending (with a mode-shape motion on y-direction) any directional uncertainty which causes exciting the structure on the same direction as the mode shape motion-direction (y-direction) causes the most significant error, and becomes a dominant error source, which in this case is column(a).

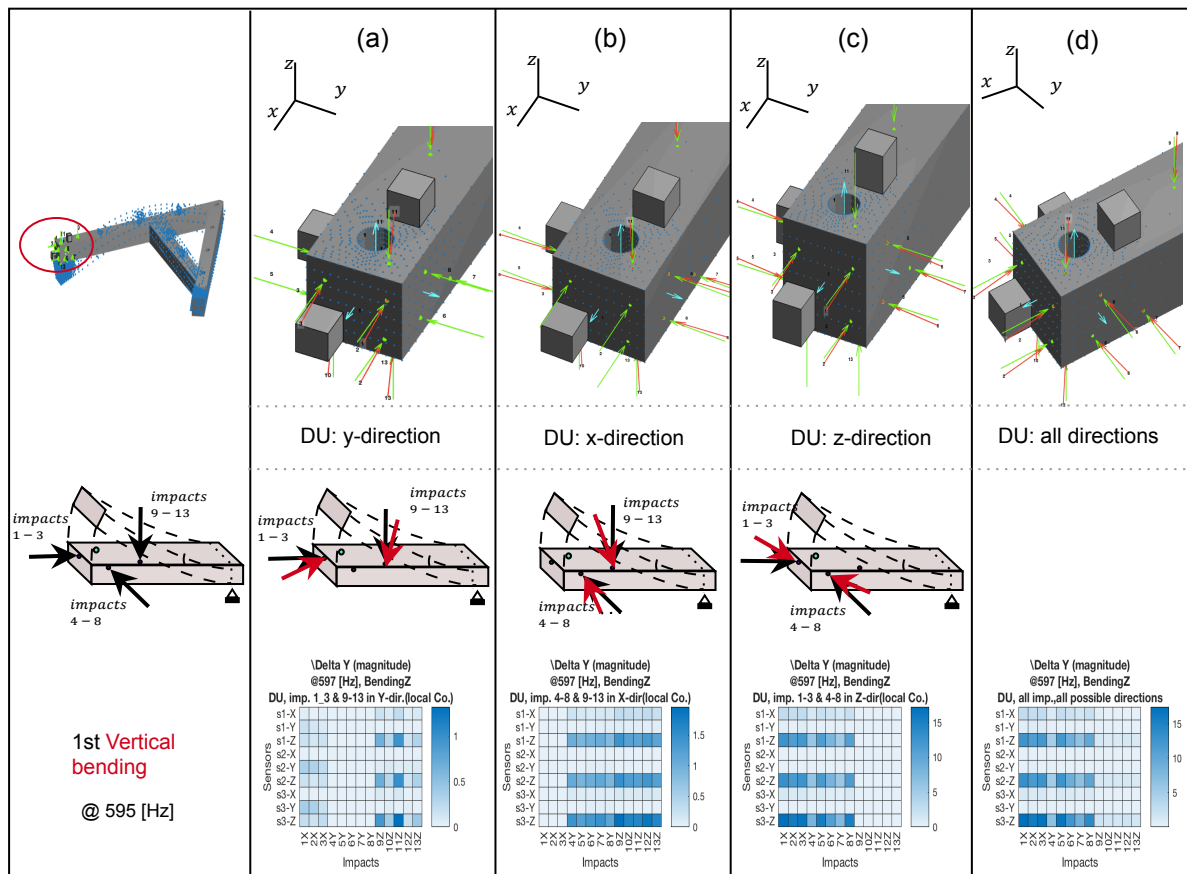


Figure 6.2: Directional error on impacts at first, vertical bending (at 595 [Hz]), where dominant direction of the mode shape motion is on z-direction. Column(c) is the case where impacts 1-3 and 4-9 have directional deviation which causes this impacts excite the structure also on z-direction. This directional error source is the most dominant error source.

Error generation in absolute value:

Figure.6.1 and Figure.6.2 also show that :

At each mode shape, the impacts acting in the same direction as the movement direction of the mode shape (MDMS) have the highest modal values, comparing with all other impacts directions.

If there is a directional deviation on these impacts, the portion of the contribution of these high modal value will decrease, and instead, some lower values will add.

On the other hand, the same directional deviation on other impacts (which their primary directions is not the same as the MDMS) have smaller modal value at that certain mode-shape.

A directional deviation, with the same direction as mode shape movement direction on these impacts, will increase the modal value of those impacts. A portion of these primary low modal values will be replaced by recently activated DOF with high modal value. Since these new added modal values are high, a portion of them is also high. Consequently, the FRF at- and around frequencies corresponds to that type of mode shape will deviate the most.

Guide line:

We can suggest if a certain mode shape of the structure is on interest, make sure the impacts acting perpendicular to that specific mode shape direction is hitting the structure as close as possible to the assigned direction.

Error generation in percentage value:

Since for the same amount of directional error, the *portion* of replaced modal value is the same, the percentage change on FRF is much greater for those ones where their *true* value was not so high.

The positive or negative value of the dominant directional error source is essential. This positive or negative value of the dominant error source becomes very crucial when we have more impacts with (in this case, directional) uncertainties. There are cases where the errors of different impacts can cancel each other. As a consequence, the propagated error to Virtual Point can decrease significantly. This is the subject of section.??.

6.1.2. VP transformation: Mode shape- and frequency-dependency of dominant error source

Since (in a measurement) the *exact* position and direction of sensors and impacts are unknown, there is some uncertainty on the transformation matrices T_u and T_f . These uncertainties leads to some FRFs' deviations (δY_{vp}) on the calculated Frequency Response Function of Virtual Point (coupling point) $Y_{vp,uncertain}$ from its true value $Y_{vp,true}$.

To find this deviation δY_{vp} , first we calculate the $Y_{vp,uncertain}$ (uncertain VP's FRF) using the transformation matrices corresponds to reference positions and directions ($T_{u,refIDM}$ and $T_{f,refIDM}$), and then we compare these FRFs with a $Y_{vp,true}$.

The reference transformation matrices ($T_{u,refIDM}$ and $T_{f,refIDM}$) are set up based on the reference position and direction of impacts and sensors. The reference position and direction means the location where the measurements *supposed* to be operated. $Y_{measure}$ is the FRF obtained from the measurement which sensors and (or) impacts are not necessarily mounted on reference position, and Y_{true} is the FRF if all sensors are mounted on the reference position.

The true VP's FRF, $Y_{vp,true}$, is calculated by true measurements Y_{true} and reference transformation matrices ($T_{u,refIDM}$ and $T_{f,refIDM}$). True measurements Y_{true} corresponds to a measurement when the sensors and impacts are on their reference position (which is achievable in a simulation).

$$Y_{vp,uncertain} = Y_{vp,true} + \Delta Y_{vp} \quad (6.1)$$

where

$$\begin{aligned} Y_{vp,true} &= (T_{u,refIDM}) \cdot Y_{true} \cdot (T_{f,refIDM}^T) \\ Y_{vp,uncertain} &= (T_{u,refIDM}) \cdot Y_{measure} \cdot (T_{f,refIDM}^T) \end{aligned} \quad (6.2)$$

Figure.6.3 considers the changes in measured FRFs at first, second, and third lateral bending (at 443, 1648 and 2335 [Hz]), in the presence of directional uncertainty. Every column of this figure shows the heatmap of deviation of measured FRF with its true value, $\Delta Y_{measure}$, when a single directional error is applied on the (possible) impacts.

In this figure, column(a) and column(b) are the cases where impacts 1-4 and 9-13 have directional deviation in their primary direction, respectively, which causes that these impacts excite the structure also on y -direction. Column(c) and column (d) are the cases where impacts 4-8 and 9-13 have directional deviation, which causes exciting structure also on x -direction. Column(e) and column(f) shows heatmaps of δY where impacts 1-3 and 4-8 have directional deviation which causes extra forces on z -direction. The most right column is the case where all impacts have directional uncertainty in all possible directions.

Figure.6.3, Figure.6.4, Figure.6.5, and Figure.6.6 show the heatmap of (absolute value) deviated Frequency Response Function of Virtual Point from its true value, (ΔY_{qm}), at resonances corresponds to lateral bending, vertical bending, torsion and mixed-Torsion-vertical Bending, respectively.

Figure.6.3 shows that at *all* lateral bendings, the absolute values of element [64] of VP 's admittance are the highest, this element is a cross-function of rotational response θ_z to moments M_z . The mode shape motion is along the y-direction.

This superposition of different directional error sources shows that directional error on impacts 9-13 which causes an extra DOF of this impact in the y-direction (which is the same direction as the mode shape motion) is the dominant error source.

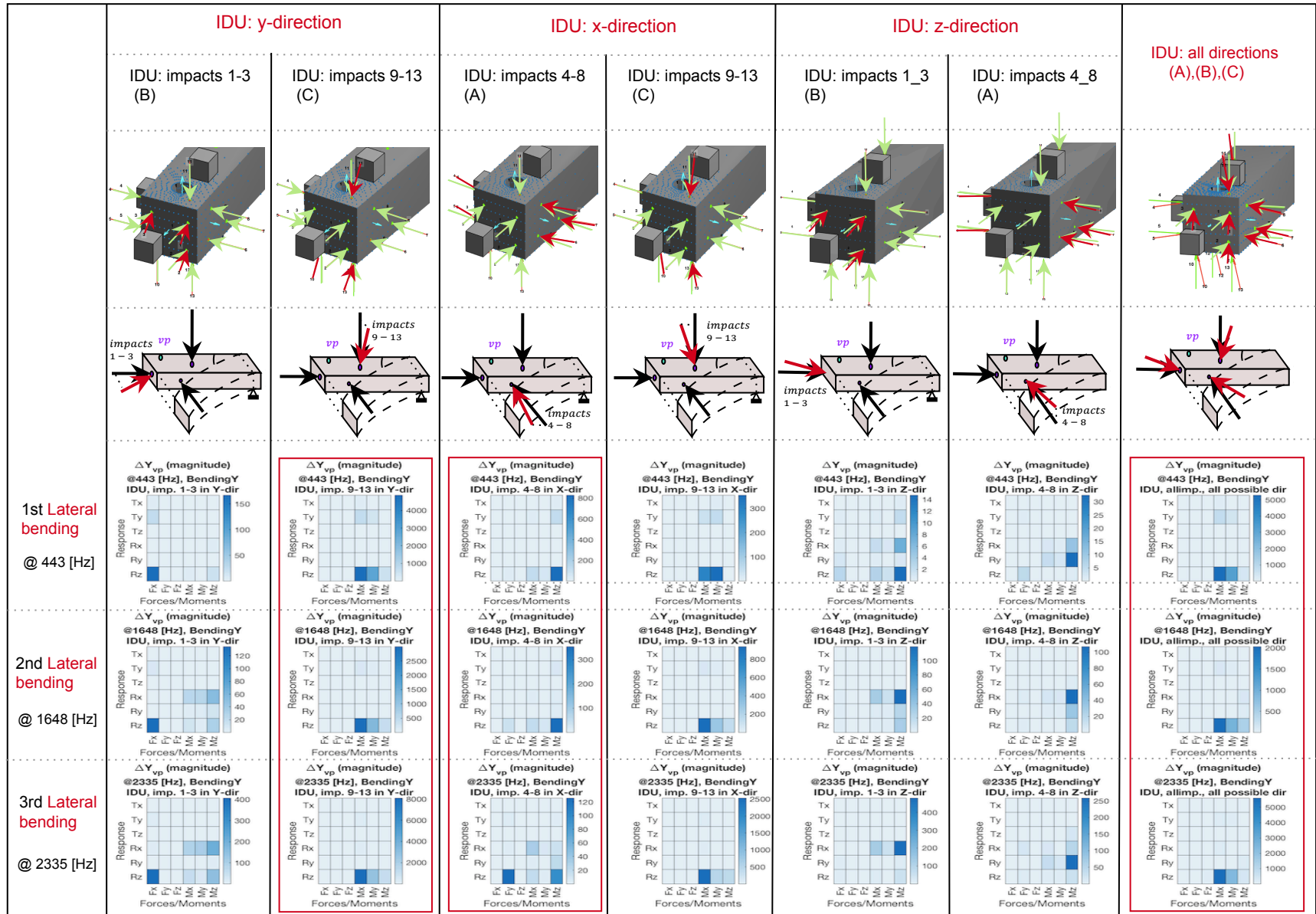
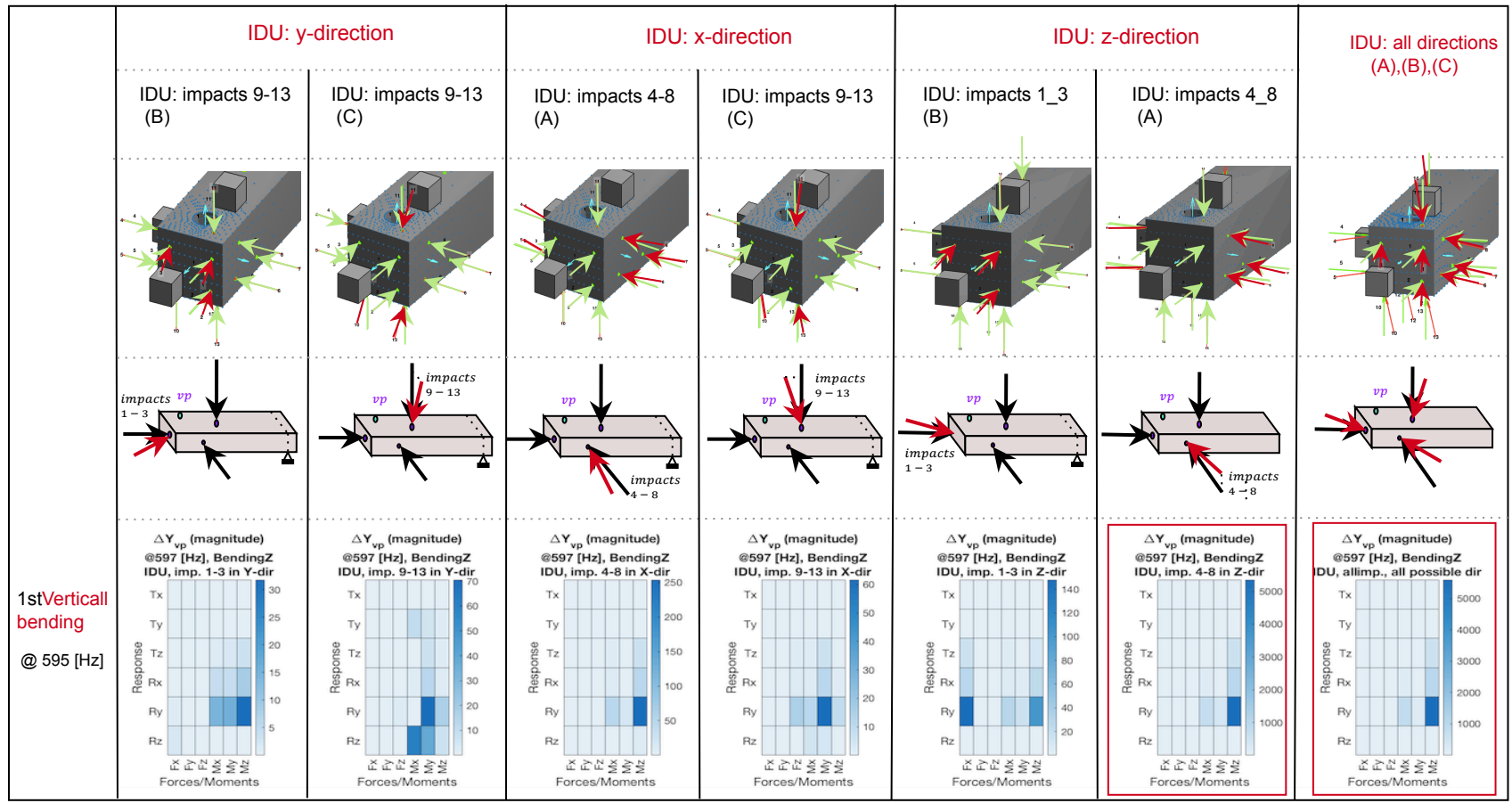


Figure 6.3: Case IDU, Super position of different directional error sources: the changes on the VP's FRF, ΔY_{vp} , at resonances corresponds to lateral bending motion (443, 1648 and 2335 [Hz]). Amount of directional error is exactly 5 degree.



1stVertical
bending
@ 595 [Hz]

Figure 6.4: Case IDU, Super position of different directional error sources: the changes on the VP's FRF, ΔY_{vp} , at resonances corresponds to vertical bending motion (595 [Hz]). Amount of directional error is exactly 5 degree.

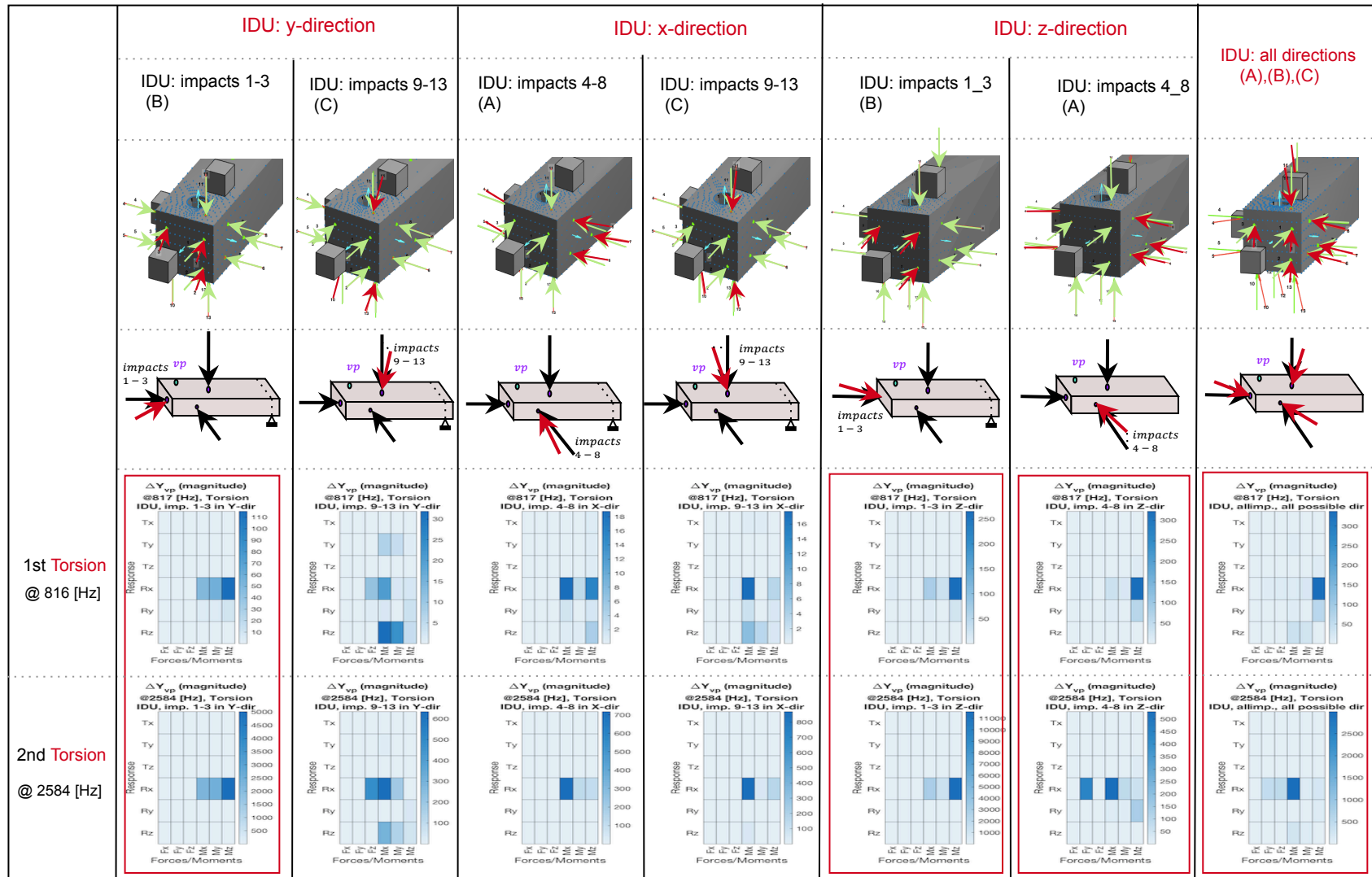


Figure 6.5: Case IDU, Super position of different directional error sources: the changes on the VP's FRF, ΔY_{vp} , at resonances corresponds to torsion motion (816 and 2585 [Hz]). Amount of directional error is exactly 5 degree.

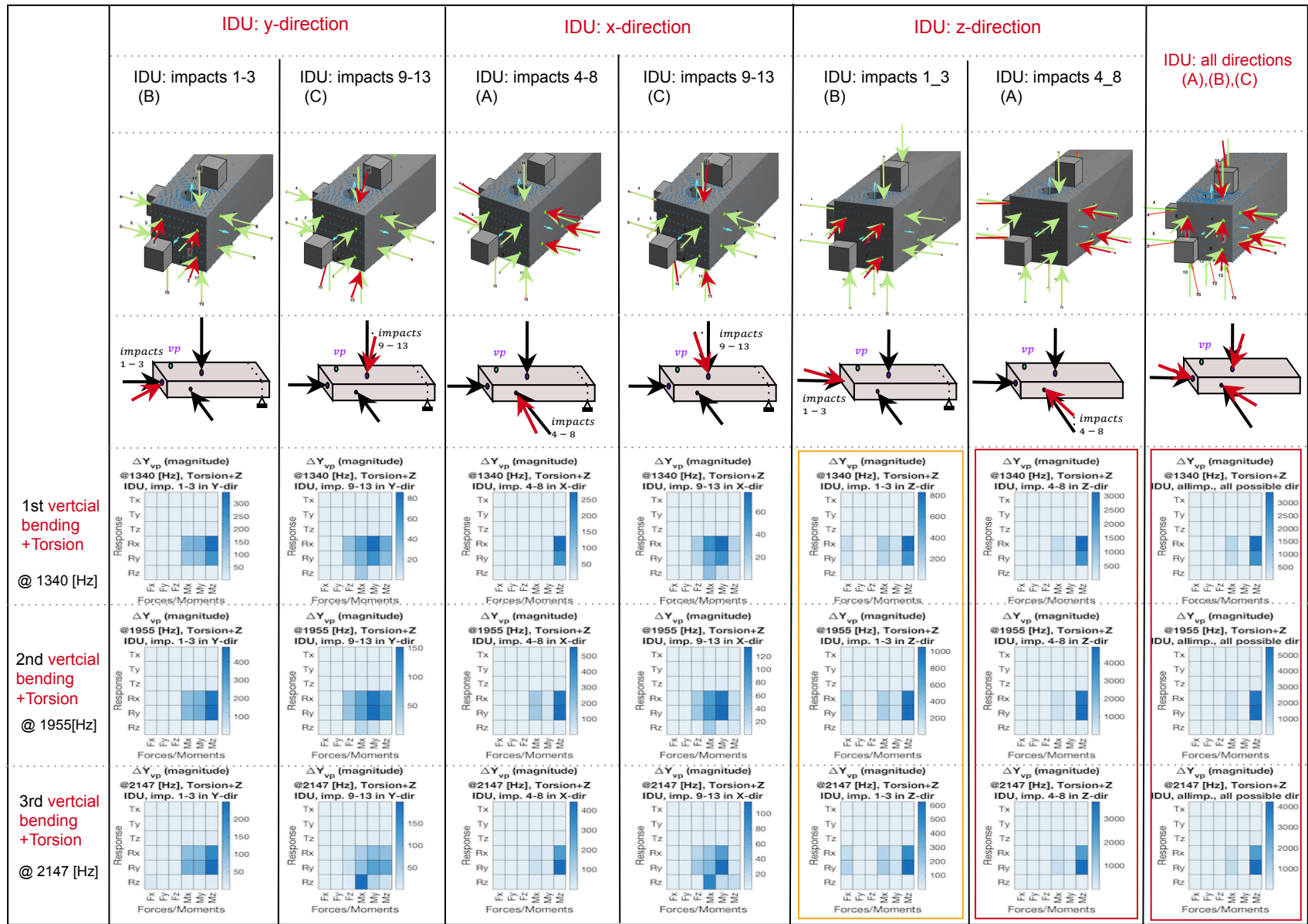


Figure 6.6: Case IDU, Super position of different directional error sources: the changes on the VP's FRF, ΔY_{vp} , at resonances corresponds to multiple mode shapes motion consisting both torsion and vertical bending (1340, 1955 and 2147 [Hz]). Amount of directional error is exactly 5 degree.

6.1.3. FRF of least precise VP 's cross-functions

From Figure., 6.3, 6.4, 6.5, and 6.6 we can observe that VP 's elements [64], [56], [46]/[44], and [56] are respectively the most sensitive VP 's cross-functions to the impact's directional errors, for lateral bending, vertical bending, torsion and torsion+lateral bending (mixed mode shape).

Figure.6.7, 6.8, 6.9a, 6.9b, and 6.8, are the frequency response function of these least precise VP 's when different directional errors are applied. These figures shows that; how each directional uncertainty affects the frequency response function and which one is most influential in error generation. We can observe that in all of these cross-functions, the dominant error source (with significant effect on error generation) for a particular type of mode shape has the same direction as those mode shapes.

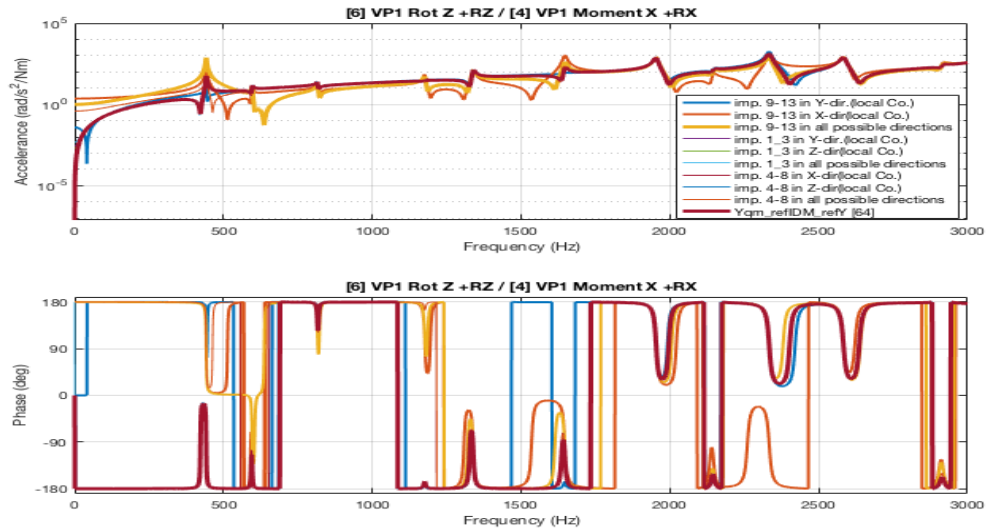


Figure 6.7: Case IDU, a comparison of different directional error sources on least precise VP 's FRF, element [66], at and around frequencies corresponds to lateral bending (443, 1648 and 2335 [Hz]). And, the dominant effect of impacts 9-13 with extra added DoF on Y direction (caused by DU). In general impacts 9-13 with all directional error causes the most error.

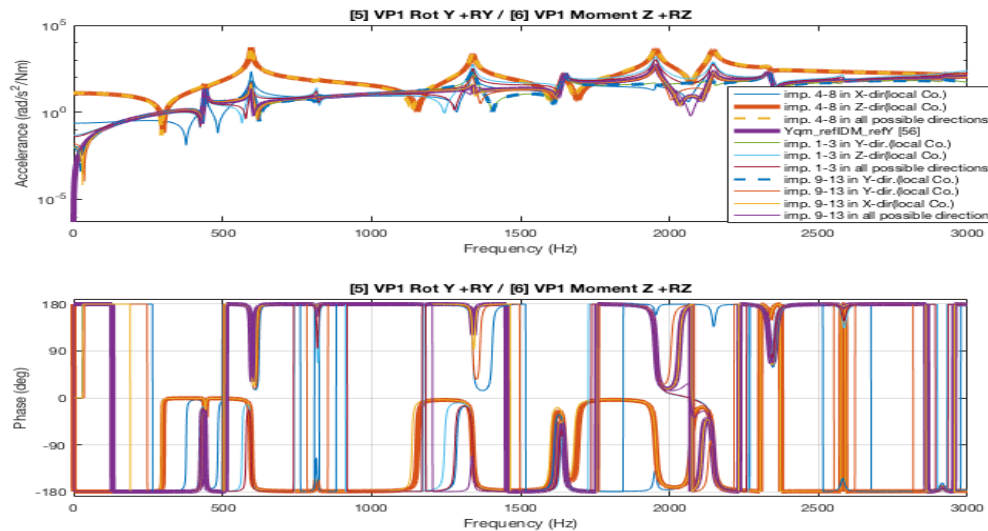
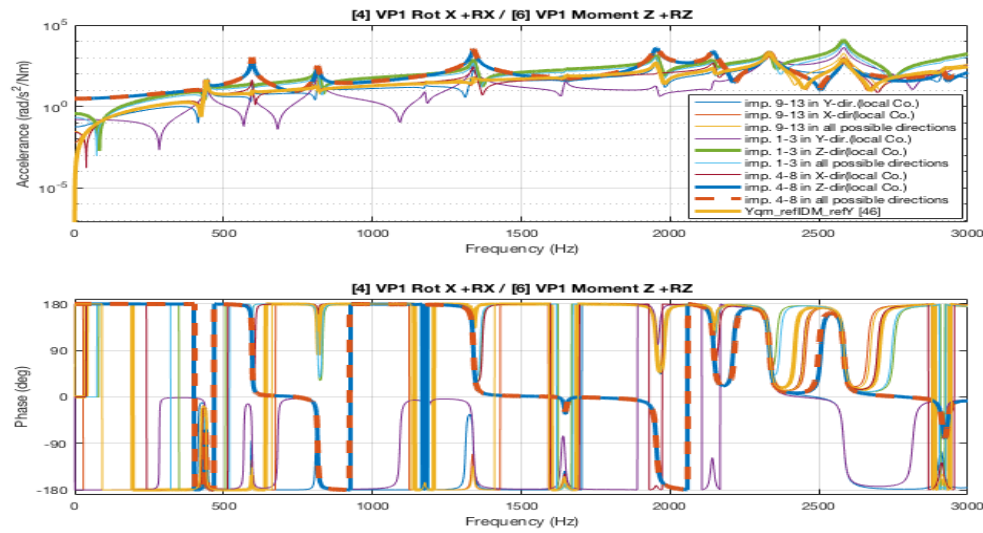
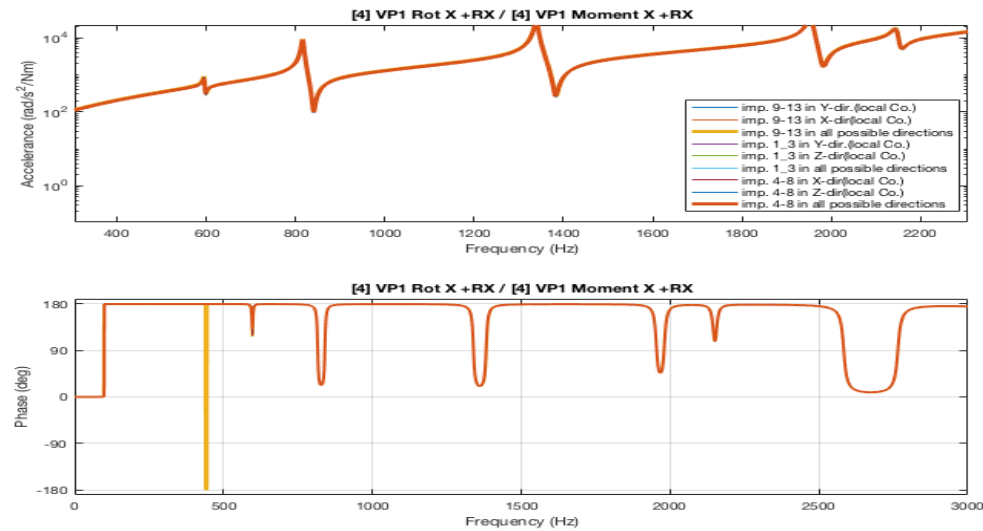


Figure 6.8: Case IDU, Super position of different directional error sources on least precise VP 's FRF, element [56], at and around frequencies corresponds to vertical bending (motion along z-axes) (595 [Hz]). And, the dominant effect of impacts 4-8 with extra added DoF on Z direction (caused by DU).



(a) Case IDU, Super position of different directional error sources on least precise *VP*'s FRF, element [46], at and around frequencies corresponds to torsion and also torsion+vertical bending (816 and 2584 [Hz] for torsion and 1349, 1955, and 2147 for mixed mode shape) . And, the dominant effect of impacts 4-8 with extra added DoF on Z direction (caused by DU). Note that these dominant error (impacts 4-8 with added force on Z direction) are also causing a significant error at 595 [Hz]. At this frequency the mode shape is also on z direction.



(b) Case IDU, element [44] of *VP*'s admittance. The absolute changes of this element observed to be high for second torsion (2585 [Hz]). Visually we do not see a lot of deviation on this FRF. Note the primary values of this FRF are also very high.

Figure 6.9

There was a groups in our mode shape categorization which has mixed-motions of vertical bending and torsion. At resonances corresponds to these mode shapes the most sensitive cross-functions of *VP* is those that are also observed on the each individual mode shape groups. At vertical bending element [56], at (first) torsion element [46], and at torsion+vertical bending both elements [56] and [46] are the most directional error sensitive cross-functions of *VP*.

In Figure.6.9b, we do not visually observe much deviation on the FRF. Nevertheless, the FRF itself has a very high value. As we discussed on section.6.1.1 (percentage- and absolute deviation), if the value of FRF is high, then its deviation can also be high compared with other FRFs, but in absolute value, it is not very high.

Note that in all FRFs with high absolute deviation (due to measurement error), the variation on phase is tiny. Maybe it is a better practice to take the phase changes to measure the FRF deviation.

6.2. Error cancellation

Section.4.2 discussed how the numerical split of each transformation matrices, R_u and R_f could lead to higher error amplification on rotational/rotational cross-functions of Virtual Point, comparing with other cross-functions.

Moreover, in Table.5.2.11 of previous chapter (in analytical approach), we have seen that the generated errors on rotational parts (rotational responses or moments) is depending on the distance to VP (r_x , r_y , and r_z). Further, the *direction* of generated errors on rotations (rotational responses or moments) is depending on the *sign of error direction* and on the *sign of the relative distance* of the error source to VP (for example the *sign* of $\delta\theta$ and r_x .)

There is a possibility for an error cancellation, where the generated errors with different signs can *cancel* each other. If the amount of these errors is also comparable, then a smart choice of measurement positions could lead to reducing the error propagation significantly.

In Appendix.I the numerical partition of transformation matrices, for the configuration presented in section5.3 is presented.

6.2.1. Effect of symmetrical impacts placement with respect to VP

If the operational errors are consistent, for example, if the experimental technician made a bias error and always excited the structure just on top-left of the true position, then there is a chance the errors cancel each other, especially on rotational/rotational part of admittance.

Figure.6.12 shows the absolute values of deviated VP 's admittance ΔY_{vp} at resonances corresponds to 1st, second, and third lateral bending. Each column shows a case where one or more impacts have positional error (IPU) of 2mm in all possible directions. For example column (a) corresponds to a case where just impact #6 contains a positional error.

Comparing columns shows that the effect of error cancellation is the best on column (h), where the most symmetry exists, mainly using impact 4 and 5 on one side of and impacts 6,7,8 on the other side of VP . This causes to have impacts of opposite directions (with respect to VP). Consequently, the generated error will have opposite directions. Since the distance of these impacts to VP is also very similar, the amount of generated errors on the rotational part are also very similar, but on the opposite direction, which leads to error cancellation on the rotational part of admittance (for lateral bending, in the case shown on Figure.6.12).

Comparing column (d), (e),(f) and (g) shows that error on impacts #6 and #8 (corresponds to column (e)) also provides a good error cancellation, which is better than error on impacts #7 and 8 (column (f)) and on impacts #6 and 7 (column (d)) and on impacts #6,7 and 8 (column(g)). The reason is that impacts #6 and #8 are on two different sides of VP , and their error is consistent, so on the calculation of VP , the generated error will be canceled with each other.

Guide Line:

Asymmetric impacts positioning is significantly helping to reduce the propagated error on the Virtual

Point's FRF, especially on rotational/rotational cross-functions.

In Figure.6.10 VP's cross-functions with higher sensitivity to IDU are given. For each plot, three types of FRFs are compared with each other, Y_{true} , $Y_{Max.Error}$, and $Y_{ErrorCancellation}$. We can see that those FRFs with error cancellation are closer to the true value. The same comparison for other uncertainty cases, IPU, SPU, and SDU, are given in Appendix ??

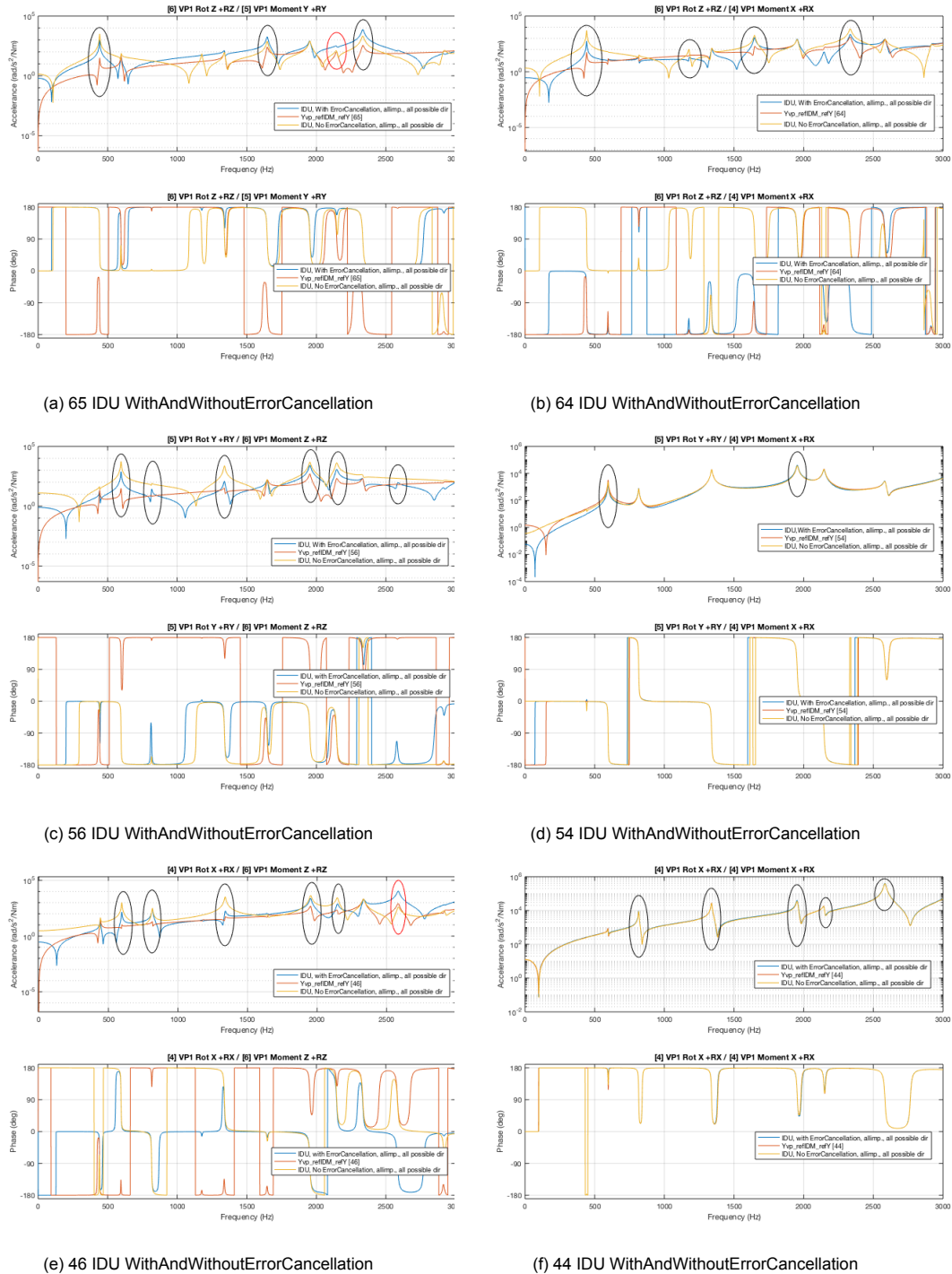


Figure 6.10: IDU

6.2.2. Effect of error's consistency on error cancellation

In order to see the effect of error cancellation in 1D, 2D, and 3D, we implement a positional error (on all directions) on dominant error source on impacts 4,5,6,7,8, and 9, for mixed motions, torsion+vertical bending. First, we implement a positional error on just one single impact, then we apply DU on two impacts, and finally, we implement errors in three or more impacts.

Figure/?? shows a comparison of the heatmaps of the VP 's admittance at resonances corresponds to these mode shapes and confirms our expectations on **error cancellation**.

In case (e), when the errors are available on just impact 6 and 8, there is a possibility to have a mirrored errors, the sign and the direction of the positional error of these two are mirrored (in x and y direction) with respect to VP . This case shows a significant error reduction.

In case (h), the mirroring is more advanced. In this case, we have the error-mirroring in more directions (in x,y, and z-direction). There are also mirrored impact's errors on the other side of the structure, on impacts 4,5. The results of this case are the best error cancellation and error reduction.

We can call case (h) a good error cancellation since we have no significant error generation on rotational/rotational cross-functions (of VP).

Figure.6.11 compares the absolute value of VP 's admittance of the best error cancellation, case (a), and a case of total no error cancellation, case (b). A significant error reduction is observed.

Guide line:

For the impacts with a particular direction, by choosing the position of the impacts on (almost) the same distances to the VP , **and** on all possible sides of VP , when the applied impacts contains the same operational error, then there is a big chance to reduce the error on calculated VP 's FRF due to errors cancellation, especially on rotational/rotational cross-functions.

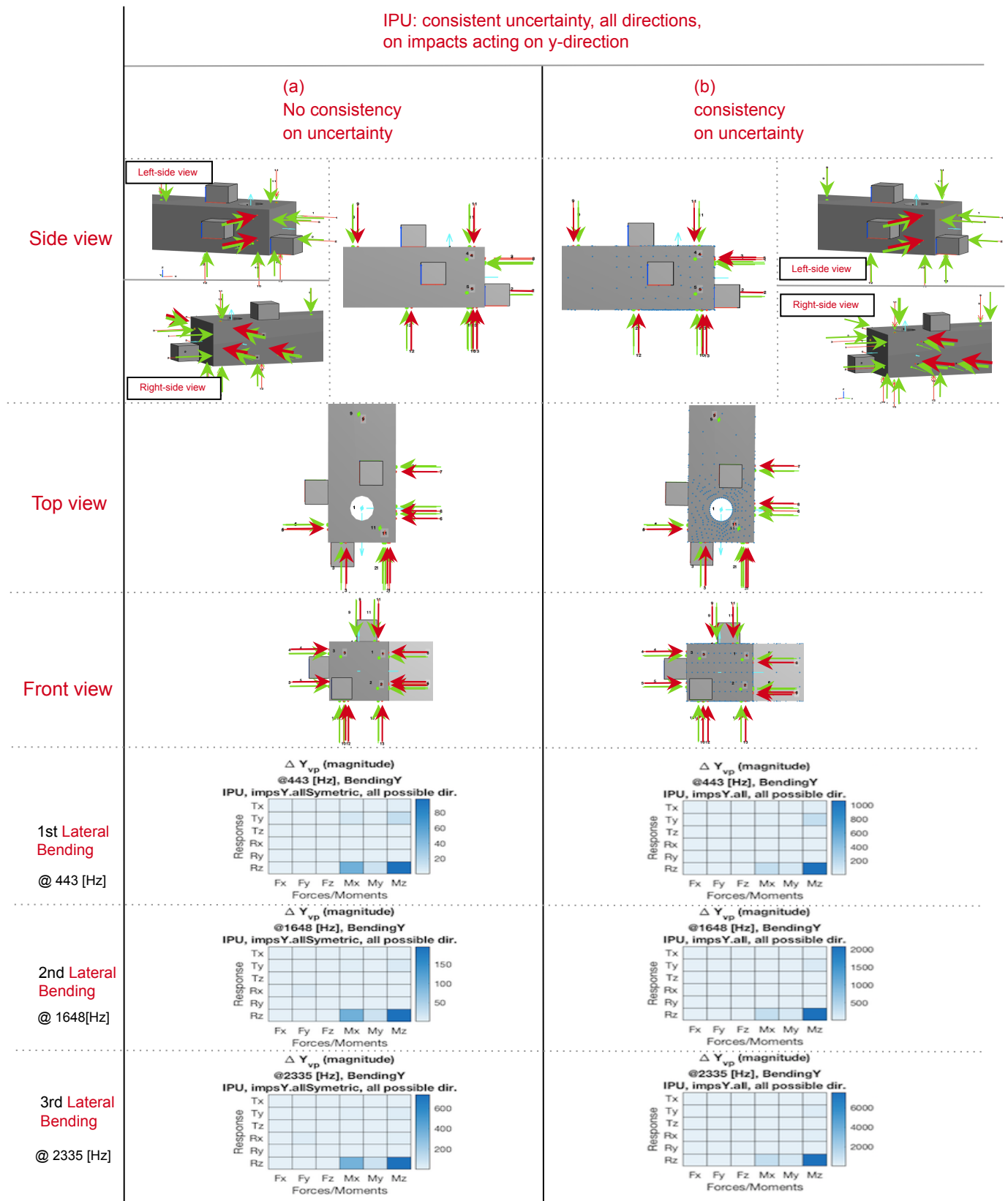


Figure 6.11: Effect of consistency on positional error implication, moment cancellation due to the same distance of these impacts to VP and the same changes on these distances due to uncertainty. Positional error of 2 [mm] is implemented in all impacts for all possible directions.

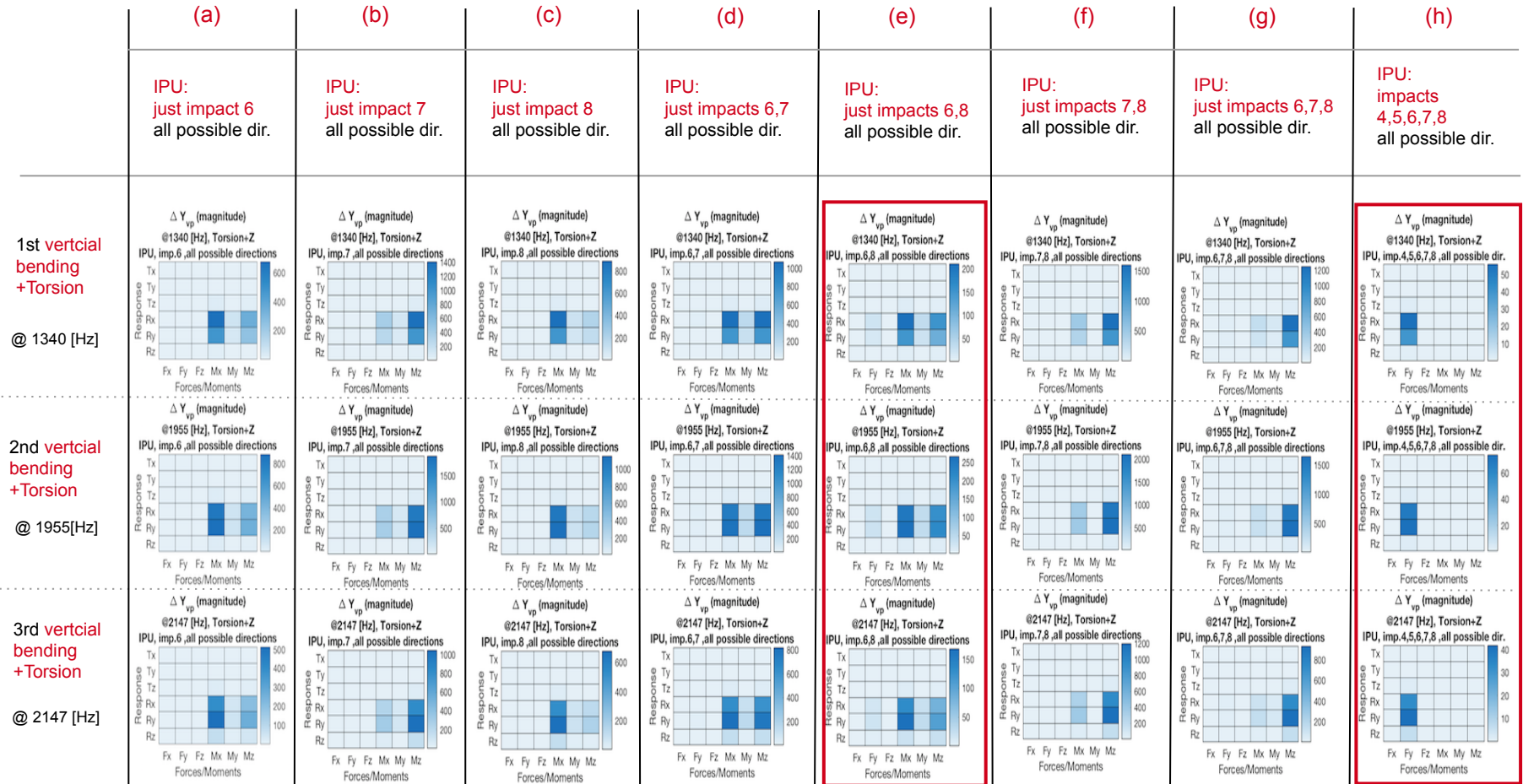


Figure 6.12: Error cancellation on VP; Positional error of 2 [mm] is implemented in all possible directions.

6.2.3. Effect of symmetrical Impacts placement on error cancellation

In order to see the effect of error cancellation, we change the arrangement of the impact on the same asymmetrical structure (FEM) introduced in section.5.3. In the new configuration, all the impacts are arranged as symmetric as possible around Virtual Point. Figure.6.13 shows the new configuration of impacts placement.

Figure.6.14 shows the effect of *symmetrical* impacts placement and *consistency on positional error* on the error propagation into *VP*'s admittance. Column (a) shows the heatmaps of the *VP*'s admittance at frequencies correspond to lateral bending. In column (b), the heatmaps of the same frequencies are obtained for the original setup (13 impacts with random distribution) with no consistency in positional error implementation.

Comparison of column (a) and (b) of Figure.6.14 shows that the combination of symmetrical impacts placements and consistency in error generation causes a significantly reduction on error propagation on rotational/rotational cross-functions of *VP*.

Comparison of column (a) of Figure.6.12 and column (a) of Figure.6.14 shows that symmetrical impacts placement, causes specifically a significant error reduction on rotational/rotational cross-functions of *VP*.

Figure.6.20 is a comparison on frequency range between 1) symmetrical impacts placement with consistent error, 2) asymmetrical impacts placement with consistent error, 3) asymmetrical impacts placement with inconsistent error, 4) true FRF (without any error) for symmetric impacts placement, and 5) true FRF (without any error) for asymmetric impacts placement.

This figures also confirms that on higher frequencies the effect of error propagation is higher, which is related to the distance of measure point and *VP* to the stand node, higher the number of a type of mode shape, higher the error generation and propagation, this is discussed in the analytical approach, in section about effect of distance to stand node and error propagation.

maybe a bit more uitleg

Guide line:

In order to reduce the error propagation caused by Impacts Positional Uncertainty (IPU), place the impacts around *VP* as symmetric as possible on all possible directions, and try to be consistent in hammering,

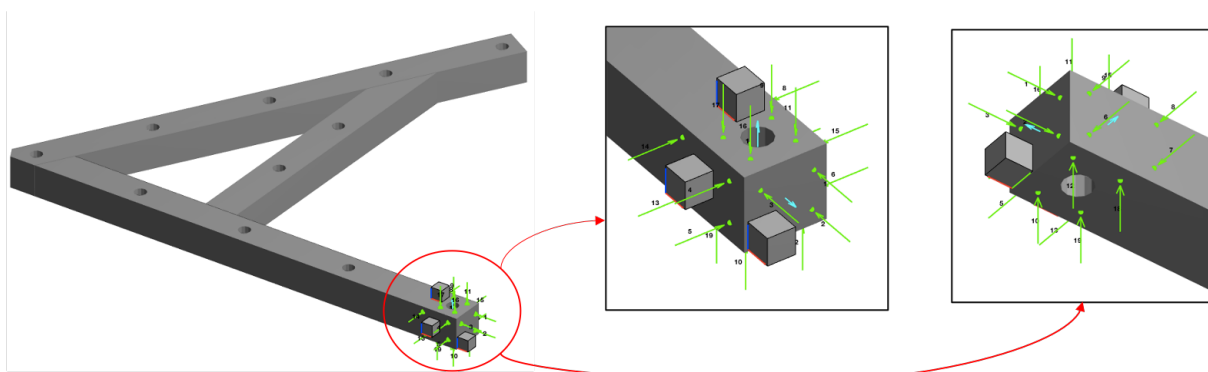


Figure 6.13: Changing the number of impacts (form 13 to 19), and the arrangement of impacts in order to have the symmetrical impacts placement around Virtual Point, as possible (we are not enable to have a symmetrical impacts placement for impacts 1, 2, and 3).

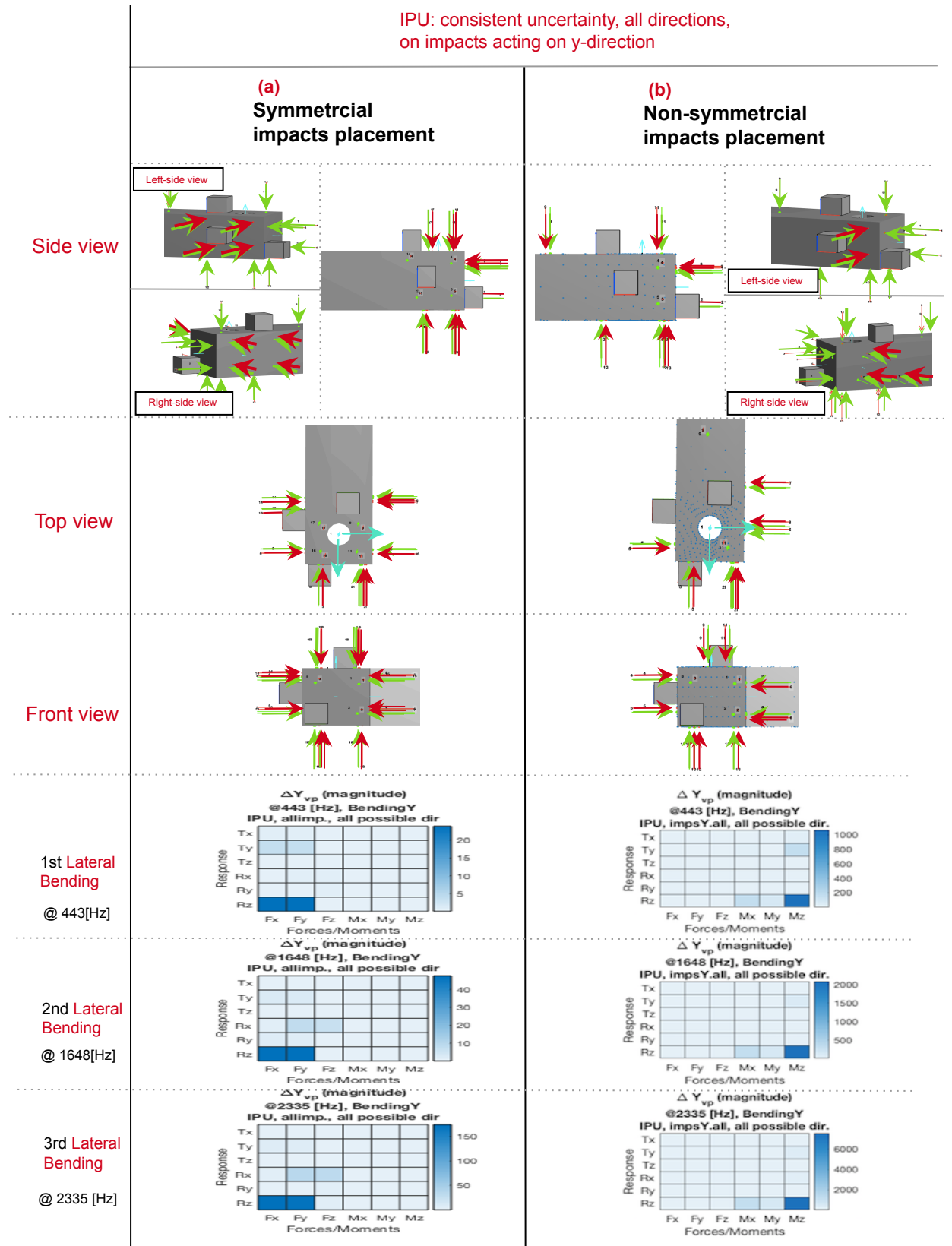
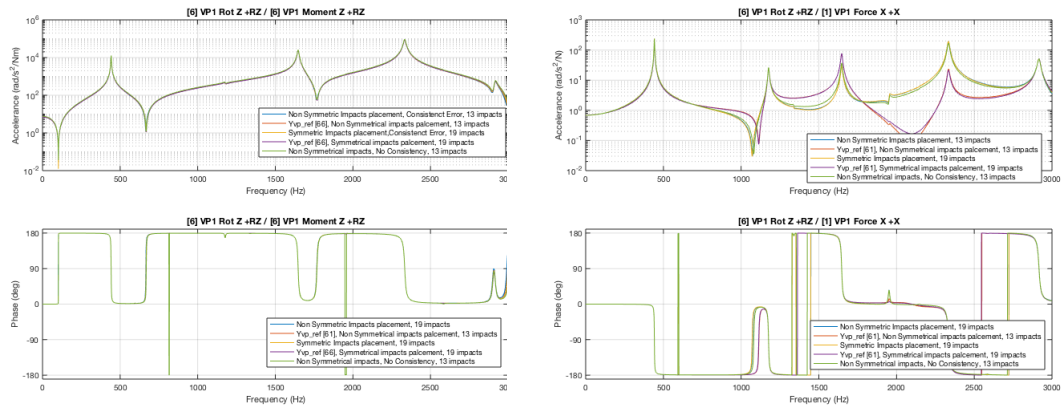


Figure 6.14: Effect of *symmetrical* impacts arrangement (with respect to *VP*), and *consistency* on positional error on moment cancellation. The same distance of these impacts to *VP* and the same amount of uncertainty (but just with opposite sign) caused the error cancellation on rotational/rotational cross-functions. Positional error of 2 [mm] is implemented in all impacts for all possible directions.



(a) Element [66] of VP 's admittance, this element has the highest deviation (in absolute value) from the *true configuration*, in the presence of IPU.

(b) Element [61] of VP 's admittance, this element has the highest deviation (absolute value) from the *true configuration*, in the presence of IPU.

Figure 6.15: Case IPU, frequency response function of Virtual Point's cross-functions [66] and [61], comparison of true measurement (simulation) for symmetrical and non-symmetrical impacts placement (new configuration) with symmetrical impacts placement with consistent error, non-symmetrical impacts placement with inconsistent error, non-symmetrical impacts placement with inconsistent error, and true measurement (simulation) for symmetrical and non-symmetrical impacts placement. Error is 2 [mm] in all impacts in all possible directions.

6.3. Results 2: Monte Carlo simulation

The Monte Carlo simulation was run 1500 times for each case. In each run, the corresponding variables are changed randomly and independently in all possible directions within a pre-default particular value.

In order to have a range of plausible values, we calculate the confidence interval of each entry (each cross-functions) at each frequency.

In statistics, the confidence interval is a type of estimate computed from the statistics of the observed data. Confidence interval proposes a range of plausible values for an unknown parameter; in our case, this parameter is the means value of each entry (each cross-function) of admittance at each frequency. First, we calculate the mean \bar{X} , and unbiased sample variance s^2 .

For a known population standard deviation σ , the confidence interval could be computed as follows:

$$(\bar{x} - z^* \frac{\sigma}{\sqrt{n-1}}, \bar{x} + z^* \frac{\sigma}{\sqrt{n-1}}) \quad (6.3)$$

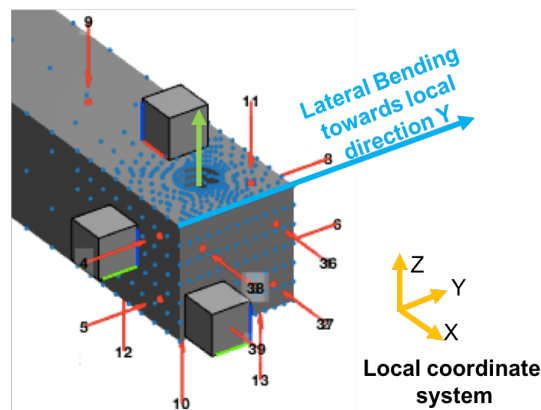
where

$$\hat{\mu} = \bar{X} = \frac{1}{n-1} \sum_{i=1}^n X_i \quad \text{and} \quad s^2 = \frac{1}{n-1} \sum_{i=1}^n (X_i - \bar{X})^2 \quad (6.4)$$

Where X_i is sample value, in our case a value of each entry of admittance at every frequency. We chose the confidence level of 95%. Since we can calculate the standard deviation, we can use Student's Distribution, and defining the value of Z^* . For the confidence interval of 95% the value of z^* is equal to 1.96. The 95%t means that if we repeat the measurement, and if we then calculate the means, there is a chance of 95% that the new calculated mean is in the determined confidence interval, but in 5% it will not be.

6.3.1. M.C. results: All cases on Lateral Bending

Comparison, the confidence interval of all cases at resonances corresponds to vertical bending. heatmap shows the elements with the most deviation.



Confidence Interval at resonances corresponds to Bending Y

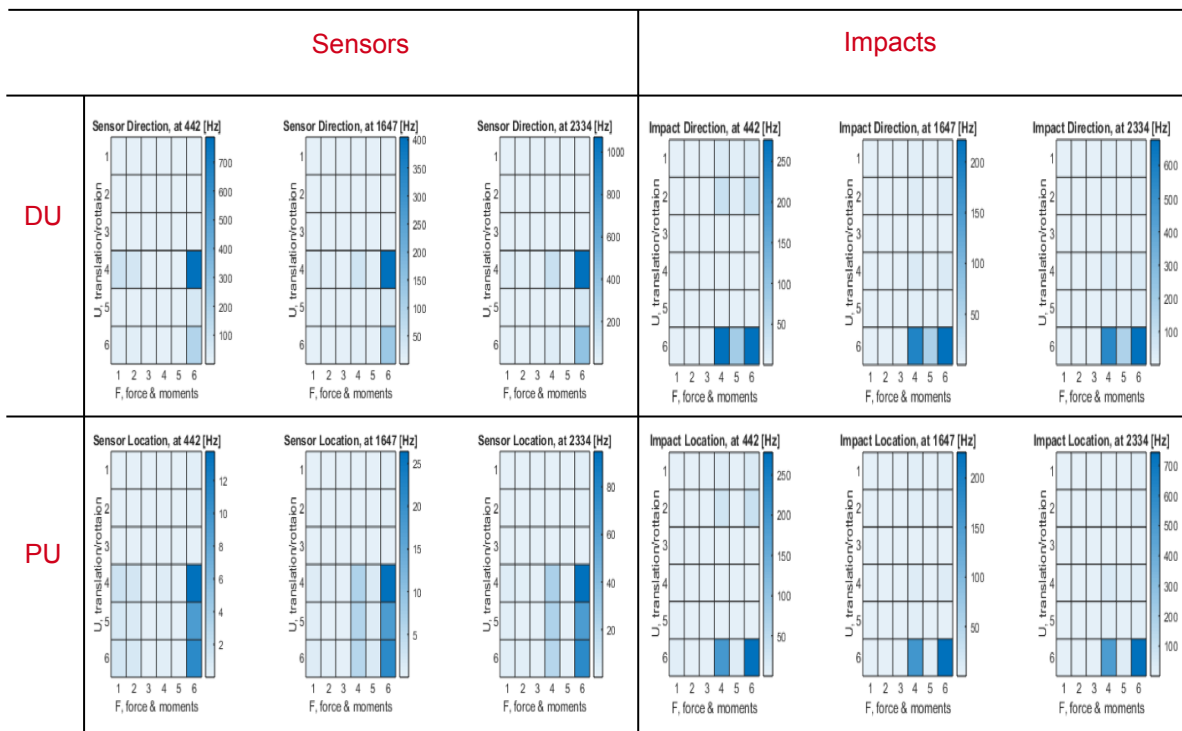


Figure 6.16: Confidence Interval, $n=1500$, The changes on the calculated FRF of Virtual Point at resonances corresponds to lateral bending motion (443, 1648 and 2335 [Hz]), sensors and impacts randomly and independently disoriented en dis-positioned

6.3.2. M.C. results: All cases on vertical bending

Confidence Interval at resonances corresponds to
Bending Z

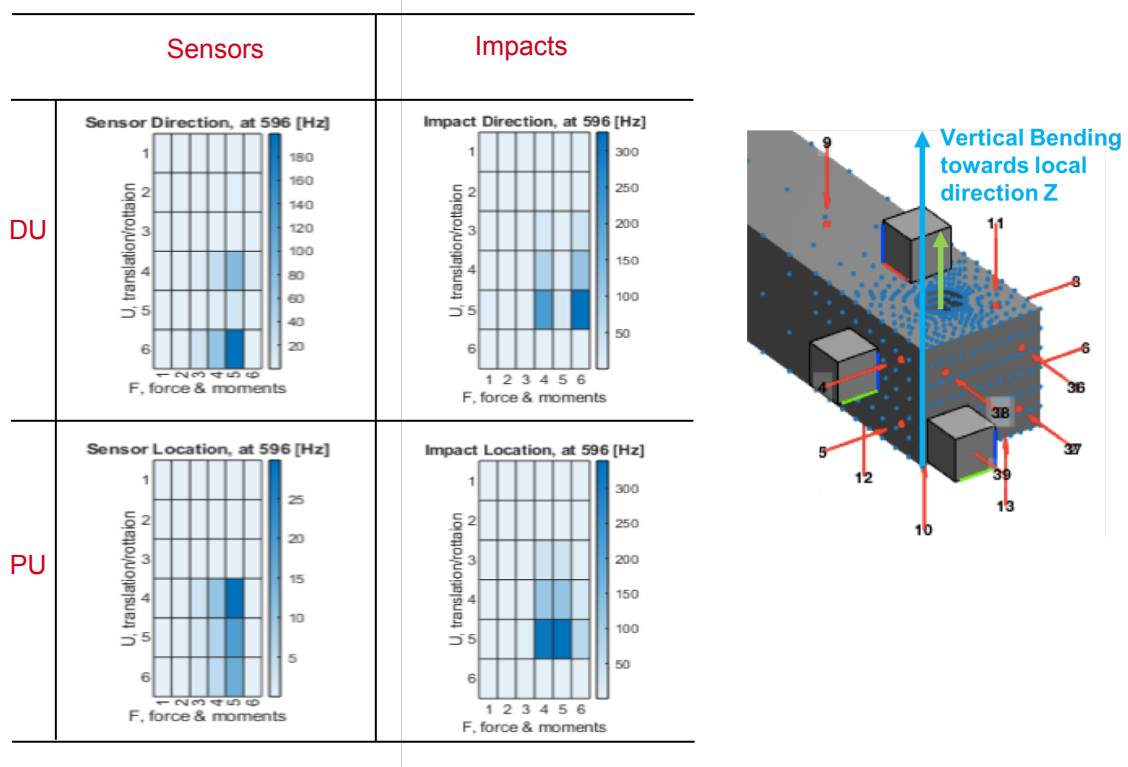


Figure 6.17: Confidence Interval, $n=1500$, The changes on the calculated FRF of Virtual Point at resonances corresponds to vertical bending motion (595 [Hz]), sensors and impacts randomly and independently disoriented en dis-positioned

6.3.3. M.C. results: All cases on Torsion

Confidence Interval at resonances corresponds to Torsion

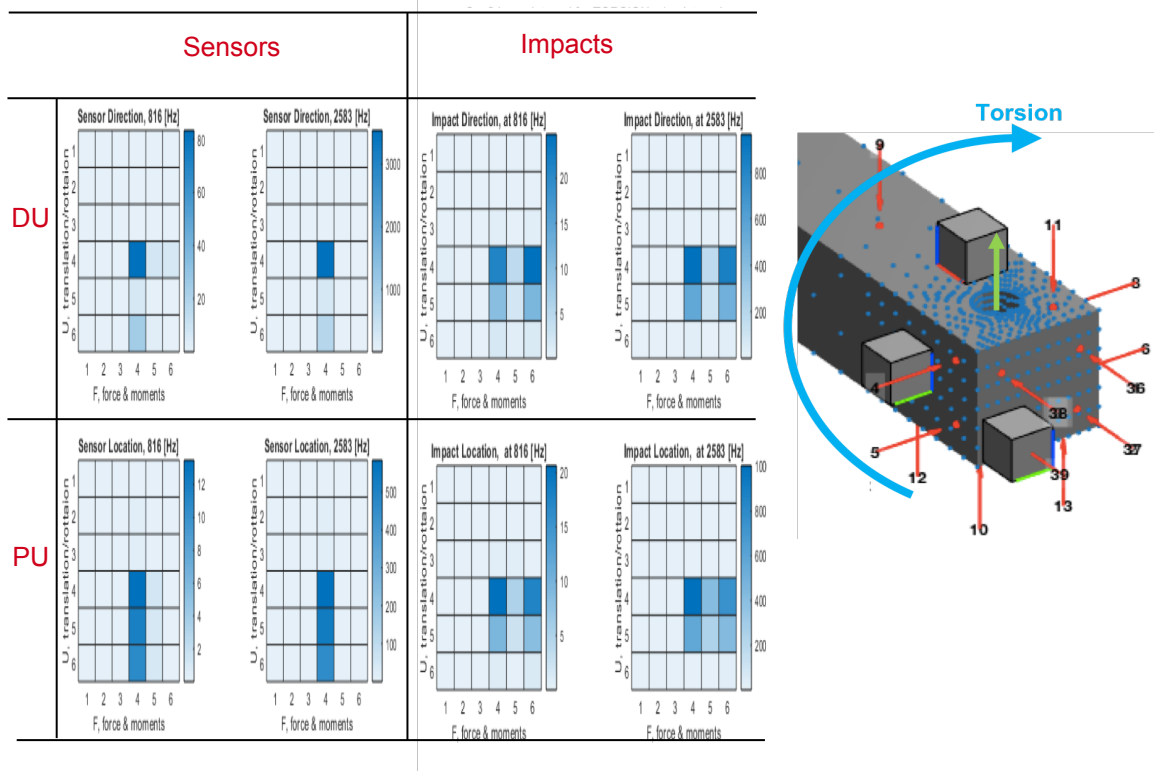


Figure 6.18: Confidence Interval, $n=1500$, The changes on the calculated FRF of Virtual Point at resonances corresponds to TORSION motion (816 and 2583 [Hz]), sensors and impacts randomly and independently disoriented en dis-positioned

The results from simulations confirm the expectations about the most deviated cross-functions of VP . All the elements with higher values are appeared on the rotational/rotational cross-functions (rotational response/moments, which is SE part of the admittance Y_{vp}).

6.3.4. Deviation on the admittance, absolute value or percentage

In Monte Carlo simulation, both cases of error cancellation and maximum error generation could happen. In the case of maximum error generation, the absolute values of deviations are much higher. Since we used statistical tools, the values of the worst cases are governing the final results of statistics. For example, in Figure.6.19 there is a sudden increase in the mean value (note that the results of Figure.6.19 are in percentage $\frac{Y_{measure}}{Y_{true}}$).

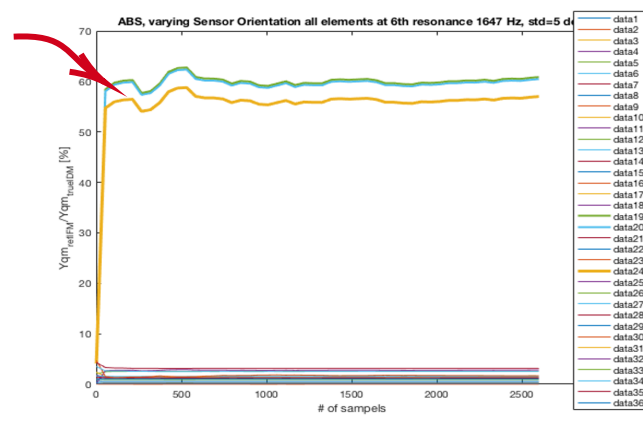
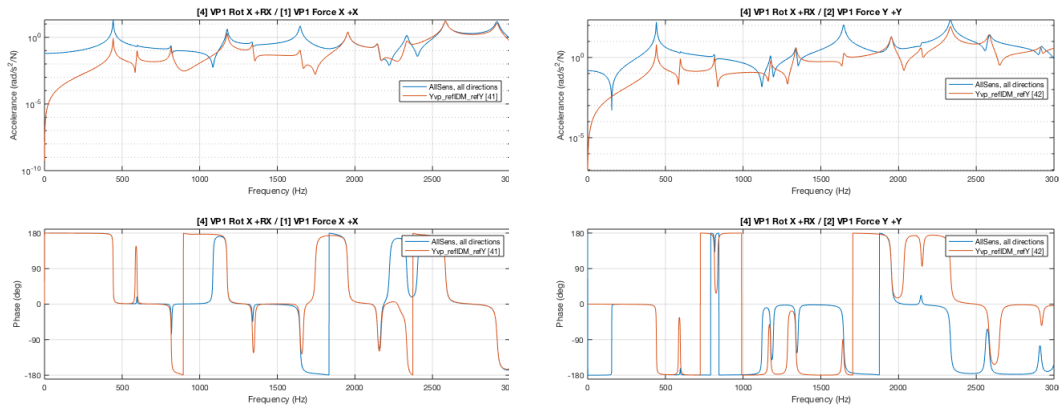
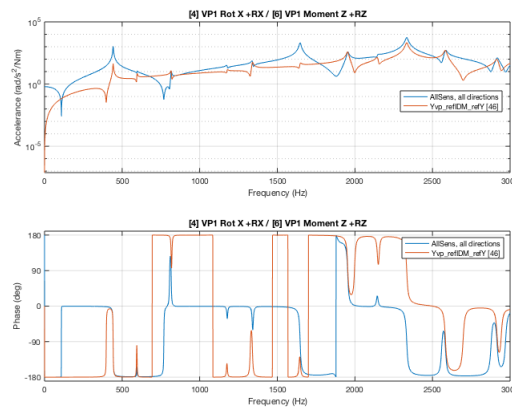


Figure 6.19: Case SDU, results from Monte Carlo simulation, mean of changes on percentage on all VP 's cross-functions, $\frac{Y_{measure}}{Y_{true}}$, as a function of sample size, at 1648 [Hz]. Elements (Cross-functions) [41], [42], and [46] (which are labelled as data 19, 20, and 24, respectively) have the highest values. The effect of worst case on error propagation can be observed with a sudden increase on error propagation. This is a case where during VP transformation all generated errors from different sources (in this case sensors) are added to each other.



(a) Element [41] of VP 's admittance, this element has the highest deviation (in percentage value) from the *true configuration*, when sensors have directional error. (b) Element [42] of VP 's admittance, this element has the highest deviation (in percentage value) from the *true configuration*, when sensors have directional error.



(c) Element [46] of VP 's admittance, this element has the highest deviation (in percentage value) from the *true configuration*, when sensors have directional error. This element has also high deviation (δY , but not the highest) on absolute value, and in case of error cancellation this entry has a relative low absolute value on absolute, at 1648 [Hz].

Figure 6.20: Case SDU, frequency response function of cross-functions with highest deviation in percentage value (Figure.C.1).

6.3.5. Evaluating the correctness of Monte Carlo simulation

In part. I of this thesis., in section.2.6.3, the characteristic of high-quality Monte Carlo simulation are listed (Sawilowsky [27]). We are confident (we checked it several times) that the algorithm used is correct and is proper for what is being used, and the proper sampling technique is used, and the generated errors are correctly random. Figures in Appendix.?? shows that the number of samples is enough to ensure the accurate results since the mean value of error (separately for each impact) after a massive number of sampling converges to (almost) zero.

In order to be able to check the correctness of Monte Carlo simulation, we need to be sure we used a sufficient number of samples. Figure6.21 shows that the *mean* value of the error of each direction for each impacts is converging to a very small value.

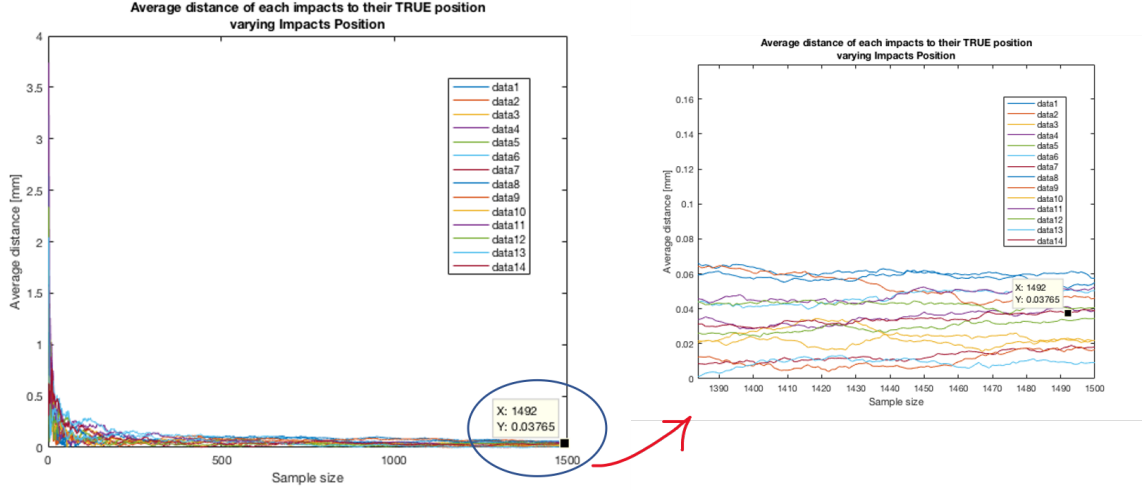


Figure 6.21: Converging the mean value of impact's positional error as a function of sample size.

6.4. Discussion

In this section, we compare the numerical results of four cases; IPU, IDU, SPU, and SPU. Case of IDU was presented in the current chapter, the results of other cases are shown in Appendix.F, H, and H.

6.4.1. Comparing numerical results of IPU and IDU cases

We comparing the deviations on the VP 's admittance caused by both types of impact's errors, IPU, and IDU, of all types of mode shapes. We can observe that a directional uncertainty of 5 degrees on impacts may cause higher error generation on the VP 's admittance than a 2 mm positional uncertainty on impacts. This comparison is based on the worst-case scenario when no error cancellation can happen.

For both cases, the amount of this error generation significantly depends on the direction of the errors, and the chance of error cancellation.

6.4.2. Comparing positional error and directional error on Sensors, numerical results

The numerical results of all four cases for each type of mode shape is given in Figure.B.1, and B.2. Comparing case SDU and SPU shows that the directional error of 5 degrees (on a single normal axes of sensor) causes less error on the most sensitive cross-functions of VP than the positional error of 1 mm, except on Torsional mode shapes, where the amount of generated errors are comparable.

6.4.3. Comparing the PU/DU on sensors and impacts, numerical results

Based on the Component Mode Synthesised method, at each mode shape, the DoFs with the highest modal value are governing the admittance at and around resonance corresponds to that mode shape. A cross-function between these DoFs has the highest value at and around those resonances. If any error causes a change in the contribution of just one of these DoFs (an input or an output), then the modal values of the other one are still significant and governing. The generated errors are also

becoming notable, comparing with other cross-functions.

This is the reason that in the presence of uncertainty on impacts, we are expecting the highest deviations (on absolute value) on the *rows*. These rows correspond to the highest response and motion of that mode shape. In the case of error cancellation, the deviation is more observable on translational cross-functions than rotational/rotational ones. This is confirmed by numerical results.

For the same reason, if there is an error on the sensor mounting, then we expect to see the most deviations on the *columns*. These columns correspond to force DoFs with the highest modal values.

For example consider the resonances corresponds to lateral bending (Figure.C.5, Figure.H.1, Figure.?? and Figure.6.3):

In the case of errors on sensors, for both rotational and directional uncertainty, the deviation on the admittance ΔY_{VP} is highest on the cross-functions corresponding to the moment around z -direction, M_z . This is observed even with error cancellation.

6.4.4. Effect of error cancellation on sensors, numerical results

The Results of directional-error cancellation on sensors is presented on Appendix.C. In this case each sensor has an rotational error in all directions, and not just in one direction. Having error on all directions for all sensors made them able to cancel the errors of each other.

Figure.?? gives a comparison of most sensitive cross-functions to SDU with- and without error cancellation.

6.4.5. Comparing analytical approach and numerical results

Correctness of symmetrical impacts placement on error reduction

Two more impacts are added to make the impacts positioning with respect to VP as symmetrical as possible, symmetry for impacts which are exciting the structure on y -direction.

Figure.6.22 compares the symmetrical impacts placement and non symmetrical impacts placement.

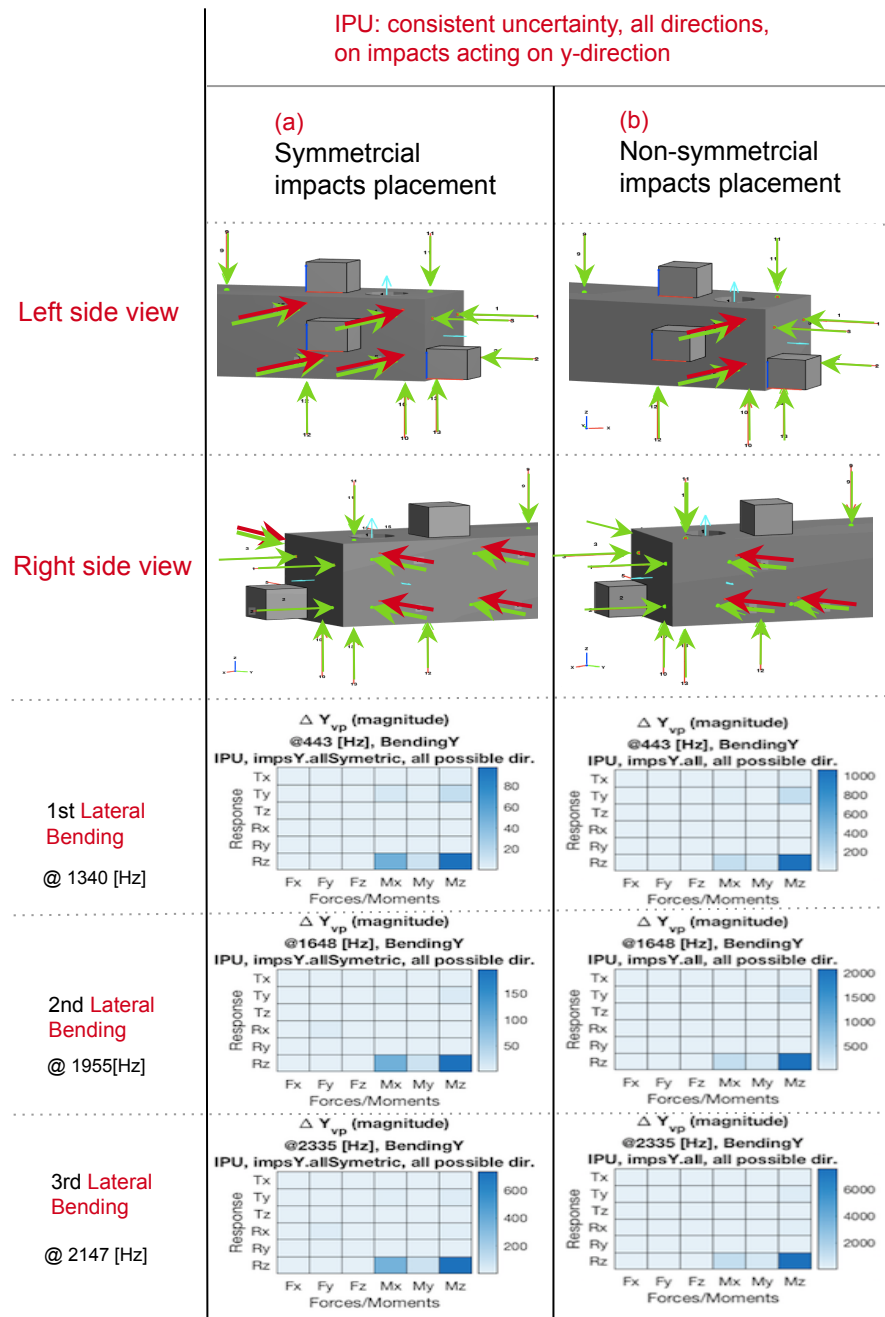


Figure 6.22: Error cancellation (IPU) on V_P 's FRF due to symmetrical impacts placement. IPU (impacts positional error) is a consistent positional uncertainty on impacts acting on y-direction, error is exactly 2mm all possible direction.

Conclusion

Building test-based models for EDS (Experimental Dynamic Substructuring) require very accurate measurement, and this thesis examines how uncertainty on sensors and impacts affects the accuracy of the test-based model.

The propagation of the positional and directional uncertainties on sensors and impacts into the calculation of super element's (so-called Virtual Points, *VP*) FRF are investigated analytically as well as numerically.

The main question and its sub-questions of this study were as follows;

- How uncertainty in the position and direction of the measuring equipment propagates to the frequency response function of the super element (so-called Virtual point, *VP*).
 - Which error at which amount is the most dominant error source?
 - At which frequencies we can expect the less precise?

7.1. Conclusion

This chapter gives the answer to these questions, and summarises the conclusions of this thesis.

The most dominant error source

Based on the local mode shape motion of measurement area, and using the Component Mode Synthesized method; expectations can be made on the inputs' or outputs' DOF with dominant effect on error generation for a particular mode shape.

According to the Component Mode Synthesized method, the modal values of each input and output (force and response) defines the behavior of admittance at and around each resonance. These modal values (of both input and output) are depending on the mode shape motion. DOFs with the highest modal value for a specific type of mode shape are playing a significant role in error propagation. Any action leading to an extra contribution of these DoFs leads to a significant change on the FRF at- and around frequencies correspond to that particular mode shape.

At each mode shape, the impacts acting in the same direction as the movement direction of the mode shape (MDMS) have the highest modal values, comparing with all other impacts directions.

If there is a directional deviation on these impacts, the portion of the contribution of these high modal value will decrease, and instead, some lower values will add.

On the other hand, the same directional deviation on other impacts (which their primary directions is not the same as the MDMS) have smaller modal value at that certain mode-shape.

A directional deviation, with the same direction as mode shape movement direction on these impacts,

will increase the modal value of those impacts. A portion of these primary low modal values will be replaced by recently activated DOF with high modal value. Since these new added modal values are high, a portion of them is also high. Consequently, the FRF at- and around frequencies corresponds to that type of mode shape will deviate the most.

This thesis shows, analytically as well as numerically, that the dominant error source (with a significant effect on error generation) for a particular type of mode shape has the same direction as that particular type of mode shapes.

Guide line:

We can suggest if a certain mode shape of the structure is on interest, make sure the impacts acting perpendicular to that specific mode shape direction is hitting the structure as close as possible to the assigned direction.

Frequencies with less precise expectations

This thesis shows analytically and confirms with numerical results that the error generation of a particular error (for example, a specific error direction for positional uncertainty in an impact) is mode shape- and frequency-dependent. Moreover, the propagated errors into Virtual Point admittance are also mode shape- and frequency-dependent.

Since the dominant error generation depends on the mode shape motion, the *VP*'s cross-functions with least precision can also be defined.

At each mode shape, the DoFs having the highest modal value (at that mode shape) are governing the admittance at and around resonance corresponds to that mode shape. A cross-function between these DoFs has the highest value at and around those resonances.

If the contribution of just one of these DoFs (an input or an output) is changing, then the modal values of the other one are still significant and governing. Then, the generated errors for these cross-functions are also becoming notable, comparing with other cross-functions.

The amount of the error propagation caused by dominant error source

By studying the error generation caused by incorrect and inaccurate transformation operators, we obtain the amount of the influence of each dominant error source on the calculation of the forces and responses of Virtual Point, on both rotational and translational forces and responses.

Table.5.2.11 summarizes all the errors on the calculation of forces and responses (for both rotational and directional kind of error).

It is also shown that based on the decomposition of transformation matrices, the rotational/ rotational cross-functions are the most sensitive ones to both positional and directional uncertainties, when we are looking to the changes in absolute value.

Error Cancellation

The *direction* of the generated errors on rotational part (rotational responses or moments) is depending on the *sign of error direction*, and on the *sign of the relative distance* of the error source to *VP* (*sign of $\delta\theta$ and r_x* .)

Further, the *amount* of generated errors on rotational parts (rotational responses or moments) is depending on the distance of measure point to *VP*, and the amount of uncertainty.

Altogether, there is a possibility for an error cancellation, where the generated errors with different signs can *cancel* each other. If the amount of these errors is also comparable, then a significant reduction on the error propagation can happen. The numerical results also confirm this possibility of significant error cancellation strongly.

In the case of IPU (Impacts Positional Uncertainty), the symmetrical placement of impacts and *consistency* on applying the error can lead to the best error cancellation on rotational/rotational cross-functions of *VP*. The consistency of applying impacts means having a bias positional error, for example, most of the time hitting the North-East of the true position.

In case of impacts, the error cancellation is more plausible; and, error cancellation in sensors is much challenging. The main challenge is the need to use more sensors all-around *VP*.

Guide line:

In order to reduce the error propagation caused by Impacts Positional Uncertainty (IPU), place the impacts around *VP* as symmetric as possible on all possible directions, and try to be consistent in hammering, section 6.2.3.

Note: as long as measuring equipment and *VP* remain on the linear area, the *placement* of inputs and outputs (with respect to *VP*) does *not* have an influence on the amount of error propagation into translational transformation of *VP*'s FRF.

Guide line:

Significant error reduction on sensors, SDU case. Figure C.5.

Maximum error generation

It is numerically shown that if all the generated errors, including dominant ones, have the same direction, then these errors will be added on top of each other, and the maximum error can be generated. The difference of this maximum error generation with the true value could be considered as the maximum expected error.

Error generation in percentage value:

In case of directional error, the *portion* of replaced modal value remains constant for a certain amount of directional error. This leads to greater *percentage change on FRF* for measuring point with primary low modal value.

Comparing the uncertainty propagation on impacts; IPU VS IDU

We compared the deviations on the *VP*'s admittance caused by both types of impact's errors, IPU, and IDU, separately for all types of mode shapes. We observed from numerical results that a directional uncertainty of 5 degrees on impacts may cause higher error generation on the *VP*'s admittance than a 2 mm positional uncertainty on impacts. This comparison is based on the worst-case scenario when no error cancellation can happen.

For both cases, the amount of this error generation significantly depends on the direction of the errors, and the chance of error cancellation.

Comparing the uncertainty propagation, sensors VS impacts

In the presence of uncertainty on impacts, we are expecting the highest deviations (on absolute value) on the cross-functions on a same *row of admittance*. This (ese) row(s) corresponds to response DoF(s) with the highest response and motion of that particular mode shape.

Further, if a sensor has a mounting error, then we expect to see the most deviations on the cross-functions on the same *columns of admittance*. These columns correspond to force DoF(s) with the highest modal values.

For example, in the case of IDU, some elements on the fourth row (element [46]) have the greatest changes on the absolute value of amplitude at frequencies correspond to lateral bending. Row four corresponds to rotational around x-axes. At lateral bending, the beam also rotates around x-axes.

Error propagation on higher numbers of each mode shape type

If the measured point is still on the same side of stand node, a certain amount of positional error δr_x will cause *higher error generation* on higher frequencies for the *higher number* of a particular mode shape, section.5.2.3. This is also confirmed by numerical results.

This is related to the distance of measure point (and VP) to the stand node; smaller the distance between the measuring point (and VP) to stand node, the higher the error propagation into VP 's admittance. In other words, higher the number of a certain type of mode shape, higher the error generation and propagation.

Effect of b_x (distance between VP and a stand-node) on percentage modal changes of VP

For a set of measurement points and VP , and for a certain type of mode shape, on *higher number of a mode shape type*, we have a reduction in the distance between VP and a stand-node, $b_{x,VP}$. From the analytical approach, We expect less percentage error on VP (P_{VP}) for the higher number of that type of mode shape. However, the numerical results did not confirm these expectations, for all mode shapes.

Guide line:

In order to reduce the percentage error propagation, place the VP more close to stand node than the measured point to stand node (section.5.2.7).

Effect of nonlinearity on error propagation into VP 's admittance

If the measuring point and VP are not placed on the linear regime, then the calculated FRF at VP is much smaller than the real values of that point (section.2.5.3). Also, the amount of error generation in the nonlinear regime in a real case is much higher than the expectation based on linear assumptions. It means, in the nonlinear regime, the error propagation is higher than the linear regime for both absolute and percentage values.

However, in the nonlinear regime, as long as $b_{VP,x}$ (distance between VP and stand node) is smaller than a_x (distance between measuring point and stand node), the generated percentage error on VP (P_{VP}) is smaller than the measurement point.

Guide line:

Since we need to be sure measuring equipment and VP are placed on the linear region, it is a good practice to locate the measurement equipment as close as possible to VP , minimizing r_x , to make sure that we accomplish the linearity assumption.

7.2. Recommendations

During the analytical approach, we have discussed multiple factors that could affect the error propagation. For a few of them, the numerical results did not confirm our expectations from analytical analysis. These unexpected results can be of interest for future work.

Moreover, by the knowledge of this thesis, the research topic can be expanded for future works. Furthermore, the chosen method to observe the sensitivity of error propagation can be evaluated for the future researches.

How to evaluate the sensitivity on error propagation, amplitude VS phase

We have seen that the propagated error (in absolute values) in some cross-functions of VP is higher than the other ones. However, if we are looking to the FRF of these cross-functions, the changes are not very visible. The percentage error in these cross-functions could be high or low. Also, the phase change of these cross-functions is not very sensitive to uncertainty.

There are also some cross-functions of VP , with high sensitivity to errors in absolute value, in which their FRF (in case of uncertainty) has a visible deviation from its uncertain case. For these cross-functions, the phase is more sensitive to changes.

In this thesis, we focused on the changes in the amplitude of the resonance. Since it seems that phase changes are more sensitive than amplitude when the deviation on FRF is observable, it is maybe a

better practice to study the variation on phase at resonances.

Modal map

It has been shown that the linearity assumption is crucial for accurate transforming the measured data into Virtual Point.

From FEM model, we can extract the modal values of each node. If we can find an area where the modal values of its nodes have a linear relation, then maybe we could call this area a rigid region, where can be used to place the sensors and impacts and Virtual Point.

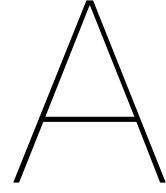
Occurrence of multiple error sources in the same time

This thesis studied the positional and directional uncertainty on the impacts and sensors separately. In real measurement, these all can happen at the same time. We recommend for future works to combine these errors on the calculation of VP 's FRF, which can be done based on the founding of this thesis.

Error cancellation on translational/rotational cross-functions of VP

This thesis shows the way we can reduce the error propagation into rotational/rotational cross-functions of VP . We recommend a further study to reduce the error propagation also on translational/rotational cross-functions of VP .

Appendices



Appendix A

$\delta\theta_y$ on impact B.

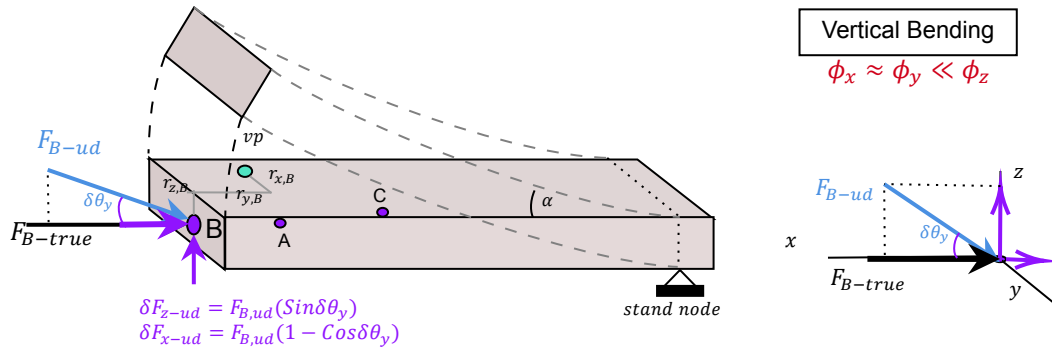


Figure A.1: verticalBending deltaZ impactB UD

First we obtain the true transformation matrix \mathbf{R}_{true} by substituting the directional difference between impact B and VP, which is $\delta\theta_y$, on rotational part (around x axes) of Eulerian rotational matrix \mathbf{E} . (Since the impacts and VP have the same generalized coordinate, the relative angular difference between impact B and VP is the uncertainty $\delta\theta_y$.) By comparing true and uncertain transformation matrices (which gives $\delta\mathbf{R}_f$) the generated error on the calculation of forces and moment of VP can be obtained. Note that the true direction of this impact (B) is along x axes ($f_B = f_x, f_{B,y} = f_{B,z} = 0$).

$$\text{forces B: } \begin{cases} \delta f_{x,vp}^{UD,\delta\theta_y} = -F_x \cdot (1 - \cos\delta\theta_y) \\ \delta f_{y,vp}^{UD,\delta\theta_y} = 0 \\ \delta f_{z,vp}^{UD,\delta\theta_y} = -F_x \cdot \sin\delta\theta_y \end{cases} \quad \text{Moments: } \begin{cases} \delta M_{\theta_x,vp}^{DU,\delta\theta_y} = F_x \cdot r_y \cdot \sin\delta\theta_y \\ \delta M_{\theta_y,vp}^{DU,\delta\theta_y} = F_x [r_x \cdot \sin(\delta\theta_y) - r_z (1 - \cos\delta\theta_y)] \\ \delta M_{\theta_z,vp}^{DU,\delta\theta_y} = -F_x \cdot r_y \cdot (1 - \cos\delta\theta_y) \end{cases} \quad (\text{A.1})$$

Forces and responses of VP, in the presence of DU, lateral bending

On lateral bending, any directional error which will lead to the contribution of forces with the same direction as the mode shape motion, will cause a significant error on the measurement, and if the transformation is not adjusted with it will cause error on the calculation of forces and moments (also responses) of VP.

We have seen that directional error $\delta\theta_x$ on impacts C and directional error $\delta\theta_z$ on impacts B generates the most deviations on FRF, at and around frequencies corresponds to this mode shape.

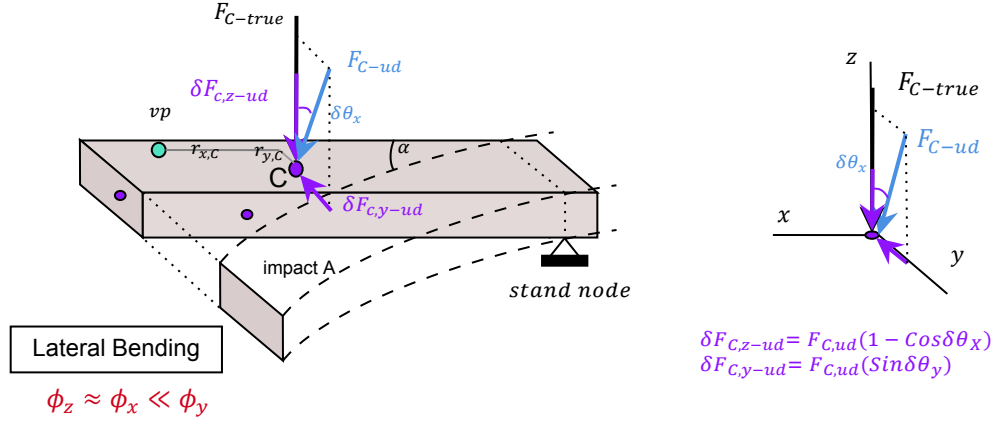


Figure A.2: UD impactC deltataetax

When impact C (which supposed to excite the structure along z axes) contains a directional error around $\delta\theta_x$, (and if the transformation matrix is not adjusted) we expect the following error generation on the forces and the moments of vo .

$$\text{forces C: } \begin{cases} \delta f_{x,vp}^{UD,\delta\theta_x} = 0 \\ \delta f_{y,vp}^{UD,\delta\theta_x} = -F_z(\sin\delta\theta_x) \\ \delta f_{z,vp}^{UD,\delta\theta_x} = -F_z(1 - \cos\delta\theta_x) \end{cases} \quad \text{Moments: } \begin{cases} \delta M_{\theta_x,vp}^{UD,\delta\theta_x} = F_z[r_y \cdot (1 - \cos\delta\theta_x) + r_z \cdot \sin\delta\theta_x] \\ \delta M_{\theta_y,vp}^{UD,\delta\theta_x} = -r_x \cdot F_z(1 - \cos\delta\theta_x) \\ \delta M_{\theta_z,vp}^{UD,\delta\theta_x} = r_x \cdot F_z(\sin\delta\theta_x) \end{cases} \quad (A.2)$$

Impact B with reference direction along z also has a dominant directional error which is $\delta\theta_z$. This error causes an error generation on forces and moments of VP which are as follow:

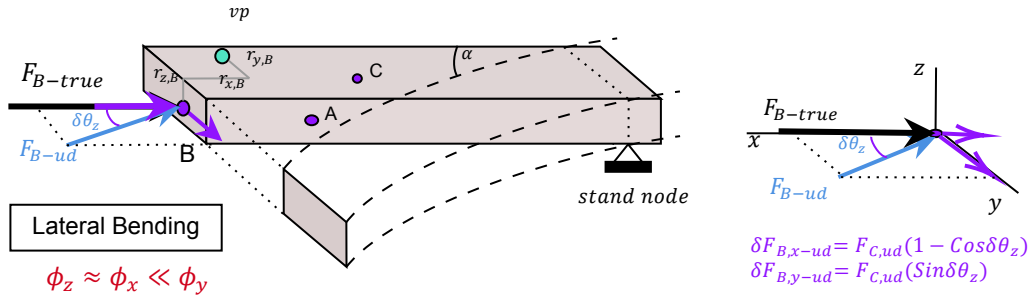
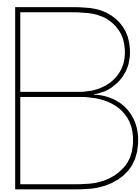


Figure A.3: UD impactB deltataetaz

$$\text{forces B: } \begin{cases} \delta f_{x,vp}^{UD,\delta\theta_z} = -F_x(1 - \cos\delta\theta_z) \\ \delta f_{y,vp}^{UD,\delta\theta_z} = F_x(\sin\delta\theta_z) \\ \delta f_{z,vp}^{UD,\delta\theta_z} = 0 \end{cases} \quad \text{Moments: } \begin{cases} \delta M_{\theta_x,vp}^{UD,\delta\theta_z} = -F_x r_z \sin\delta\theta_z \\ \delta M_{\theta_y,vp}^{UD,\delta\theta_z} = F_x r_z (1 - \cos\delta\theta_z) \\ \delta M_{\theta_z,vp}^{UD,\delta\theta_z} = F_x[r_y \cdot (1 - \cos\delta\theta_z) + r_x \cdot \sin\delta\theta_z] \end{cases} \quad (A.3)$$

take all $\sin(\delta\theta = \delta\theta)$ and $\cos(\delta\theta = 1)$ because the dominant error is in the direction of delta sin!!!!



Comparison of all cases from numerical results

This part compares the results of all four cases; IPU, IDU, SPU, and SDU, for each group of mode shape type. In each case, just the position or just the direction of just sensors or impacts are changed. In each case, the position (or the direction) of all the sensors (or impacts) changes, with the same amount. The position of sensors and impacts are changed 1 and 2 mm, respectively. The directional error for both sensors and impacts is 5 degrees.

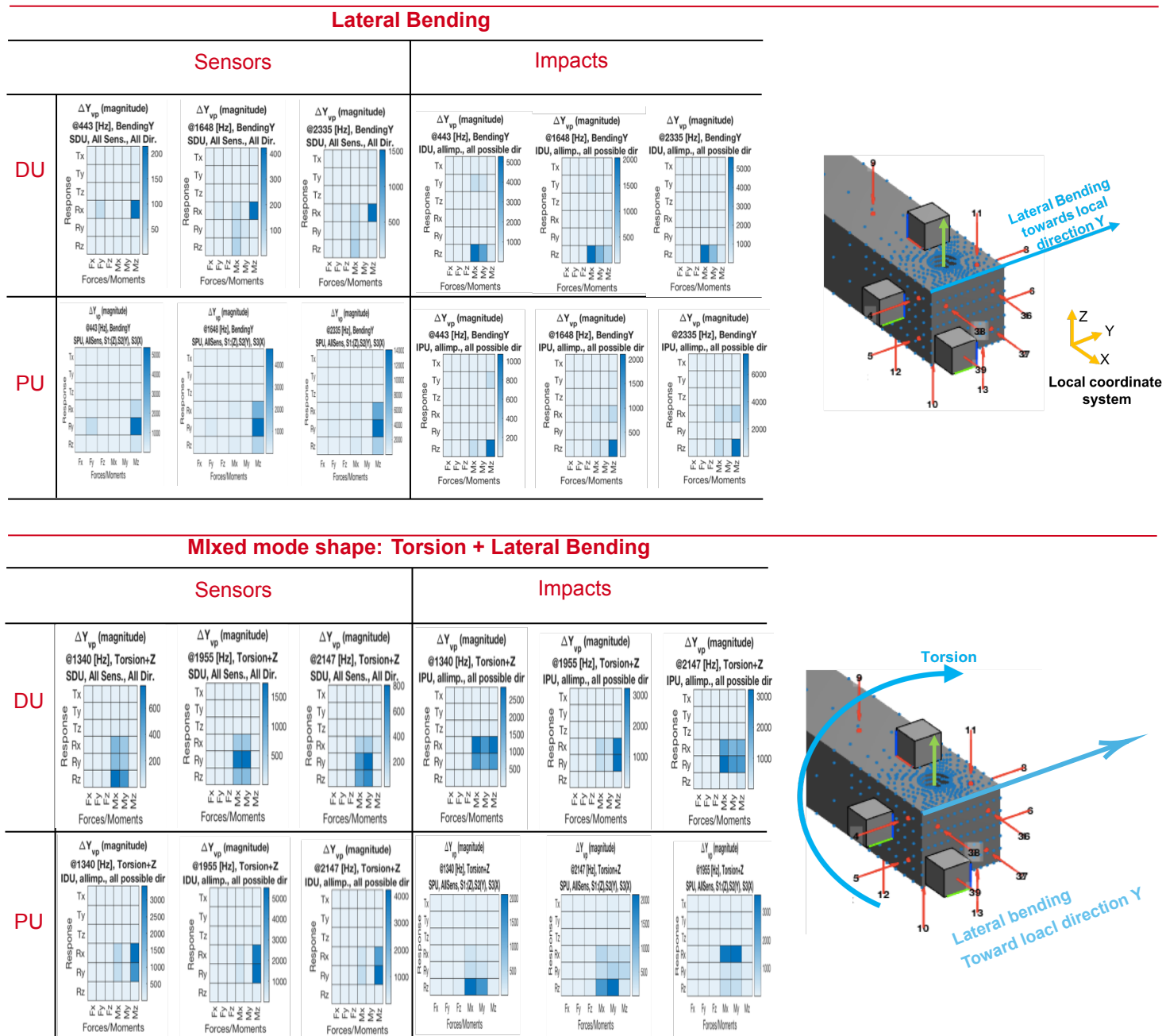


Figure B.1: comparison Y and TZ AllFinalNumericalResults withoutErrorCancellation

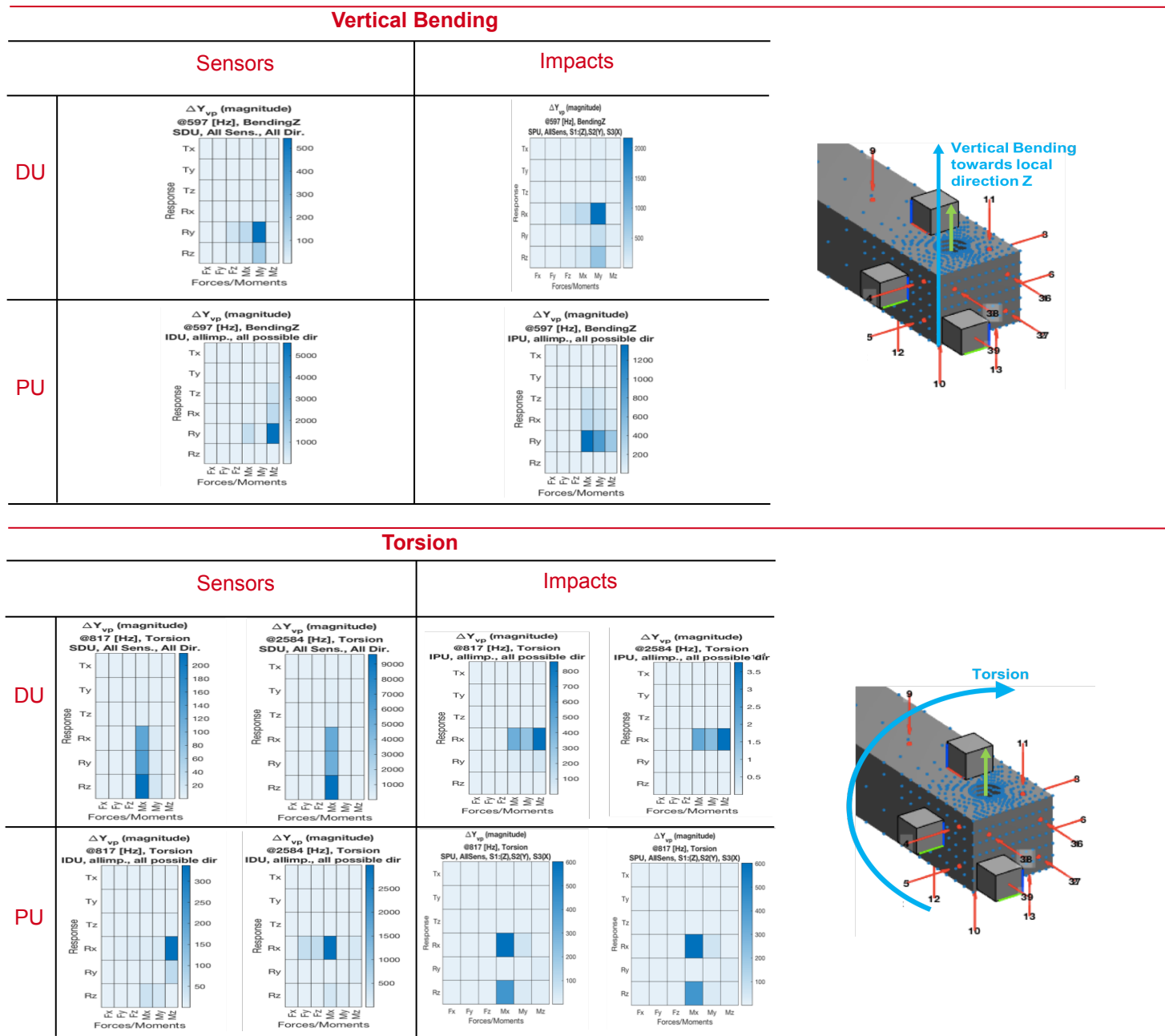
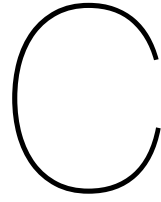


Figure B.2: comparison Z and T AllFinalNumericalResults withoutErrorCancellation



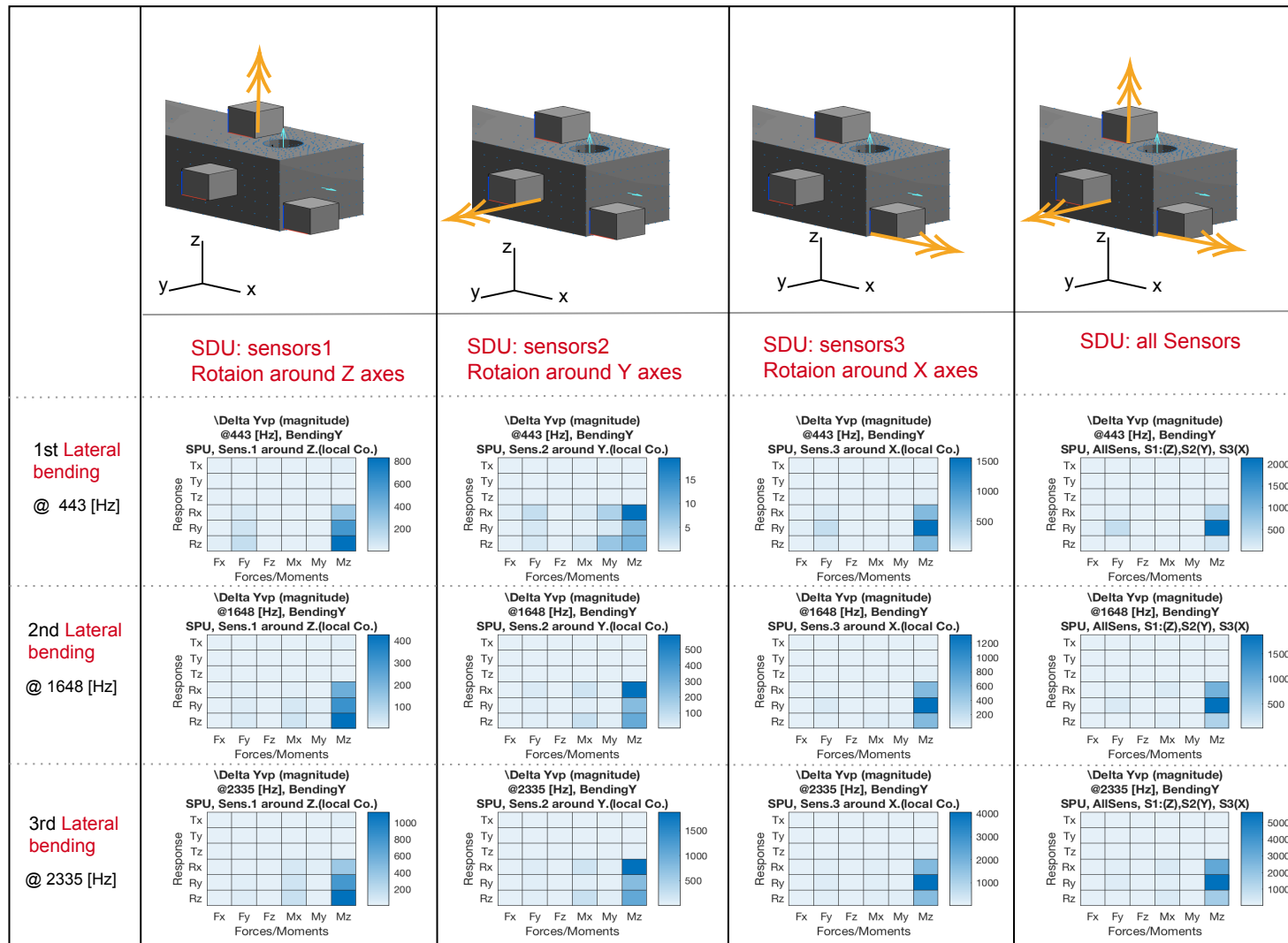
SDU, Sensors Directional Uncertainty

C.1. Case SDU, without error cancellation

We take an assumption, sensors are sticking perfectly to the structure and there is no rotational errors on those directions. It means each sensor may have a rotational error on just one direction, which is rotating around the normal axes of the surface of structure. The amount of rotational error is equal to 5 degrees.

In every column of each figure, one of the sensors is rotating around the normal-axes of the surface. The most right column shows a case where all sensors contain rotational uncertainty.

From Figure.C.1 we can see that in frequencies corresponds to lateral bending motion, the rotational error on sensors #3 is the dominant error source (second column from right of Figure.C.1). The reason could be that in lateral bending, the sensor 3 has the most motion and its modal values are y-direction is significant. Slightly rotation around x-axes will cause that two channels of this sensor record data also from the y-direction. Since the motion of this sensor is significantly higher than other sensors, this directional uncertainty becomes a dominant directional error source. Since the impacts do not have any uncertainty, their value for corresponding DoFs remains high. Moreover, the dominant motion of lateral bending is rotation around z axes, θ_z . That is the reason the most sensitive cross-function (in absolute value comparison) corresponds to M_z .

Figure C.1: Super position of errors for SDU Amount of directional error is *exactly* 5 degree.

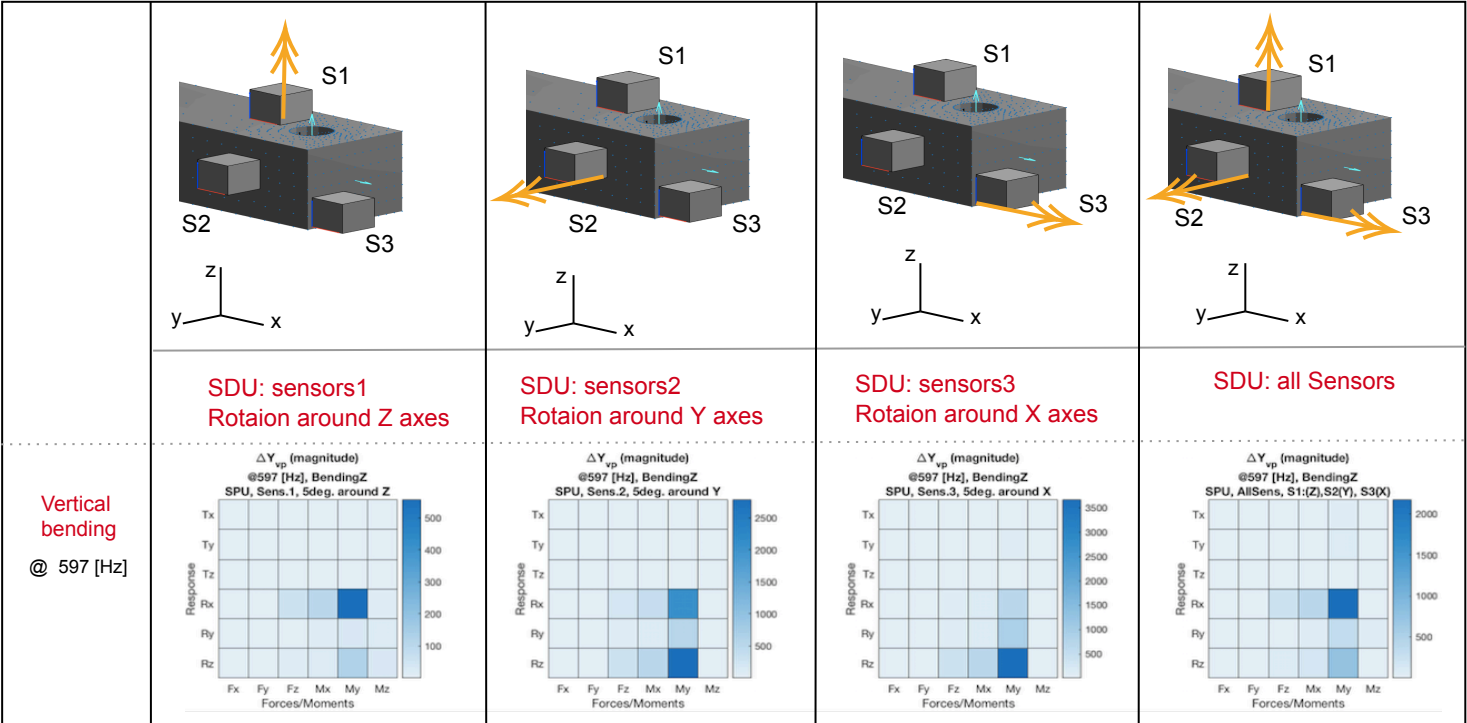


Figure C.2: SDU VerticalBending, Super position of errors for SDU Amount of directional error is *exactly* 5 degree.

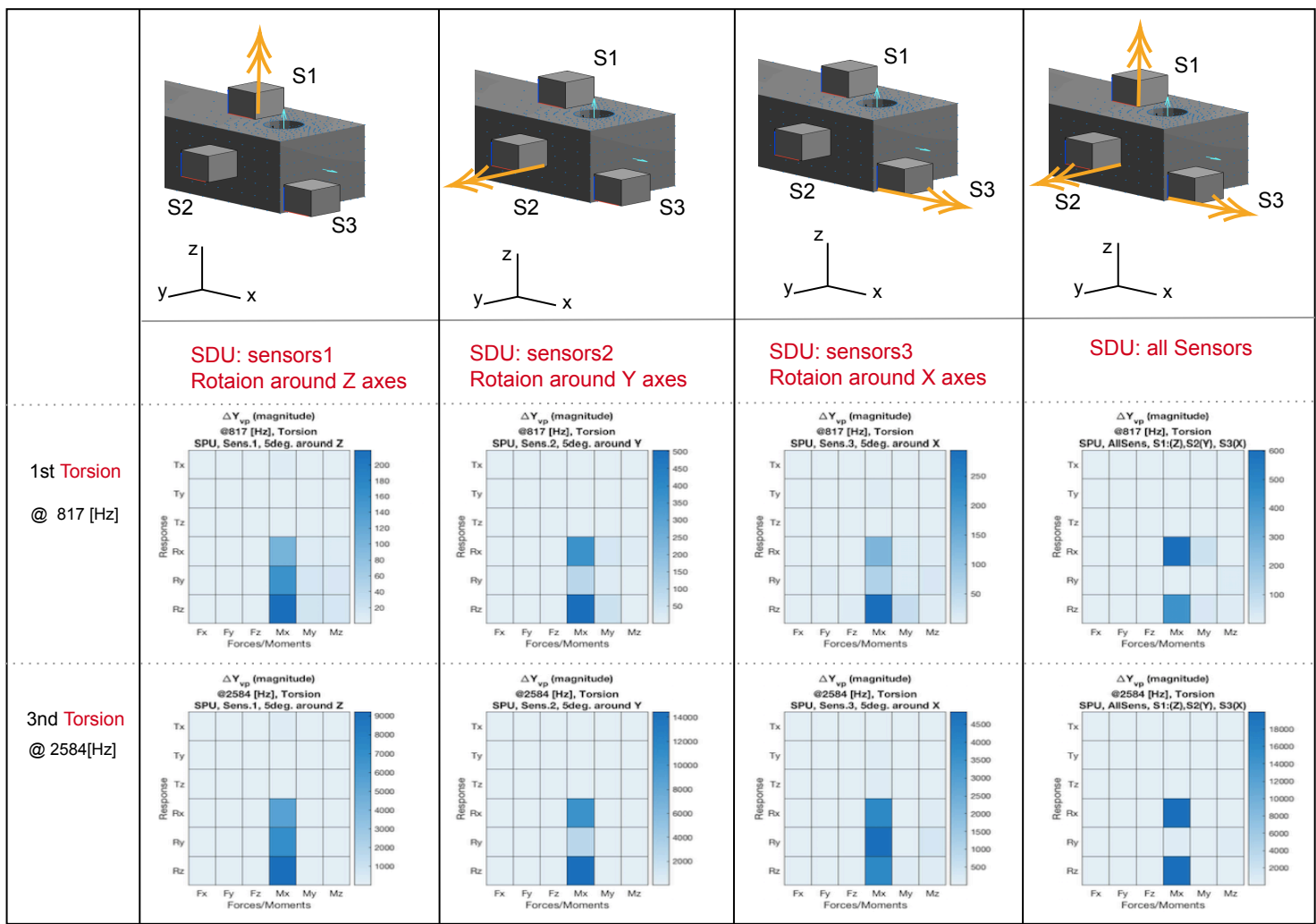


Figure C.3: SDU Torsion, Super position of errors for SDU Amount of directional error is *exactly* 5 degree.

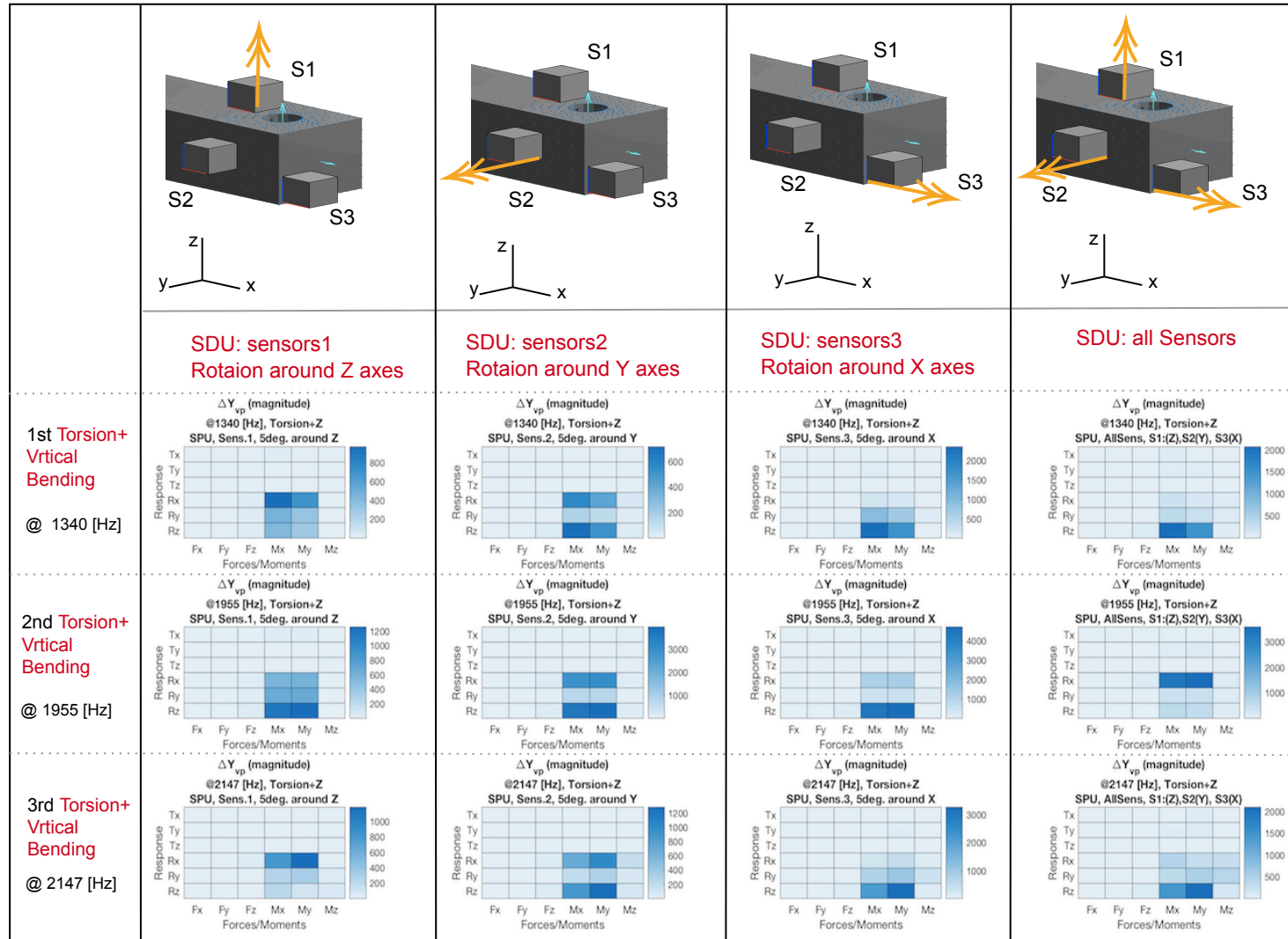
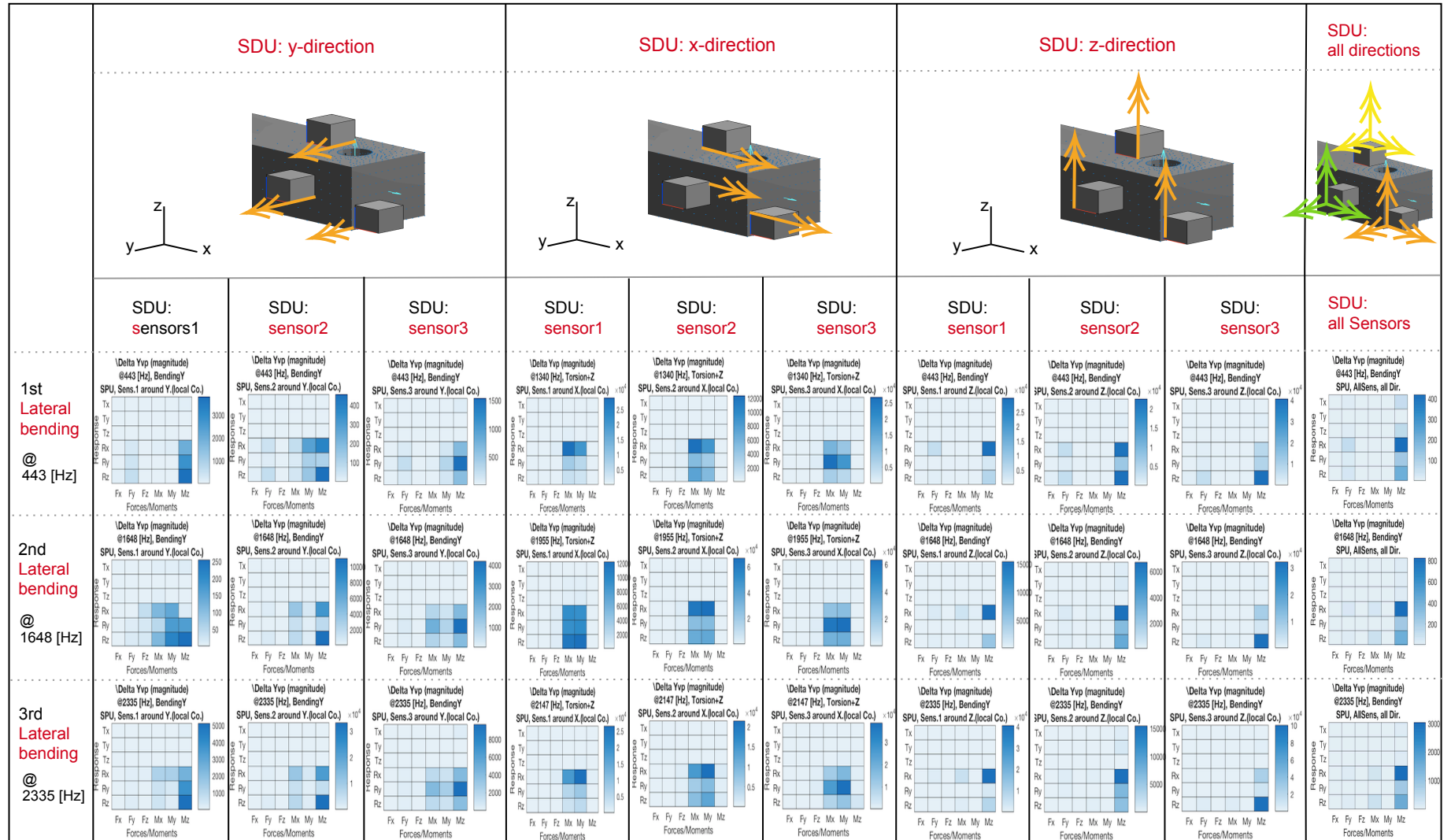
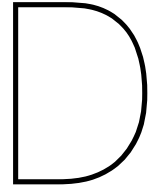


Figure C.4: SDU Torsion+ VerticalbEnding, Super position of errors for SDU Amount of directional error is exactly 5 degree.

C.2. Case SDU, effect of error cancellation on sensors

The following table (Table.C.5) is representing the deviation on admittance on resonances corresponds to lateral bending (first, second, and third lateral bending) when each sensor may have Directional errors in **all** direction. In this case we can see the lower error generation on virtual point due to the error cancellation. This error cancellation is a consequence of having more possibility of making errors which can cancel each other. For this table, the amount of directional error is 2 degree, for each direction.

Figure C.5: Super position of errors for SDU Amount of directional error is *exactly* 5 degree.

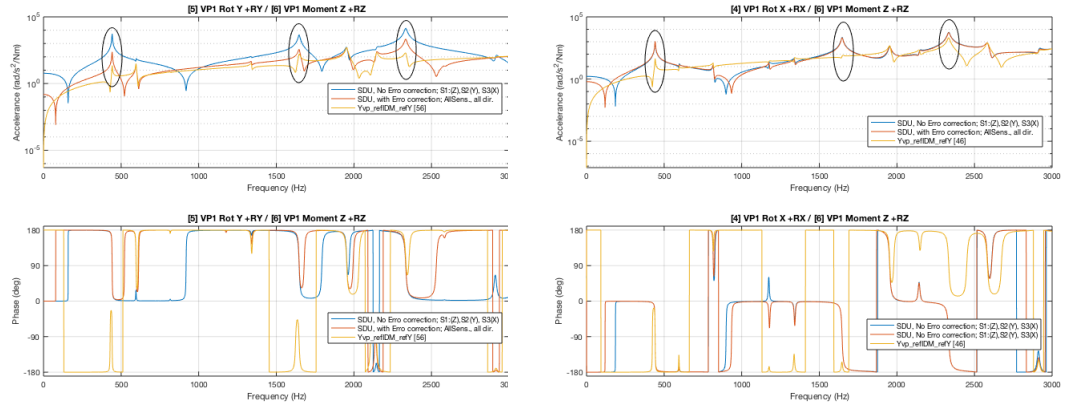


Effect of Error cancellation, case SDU

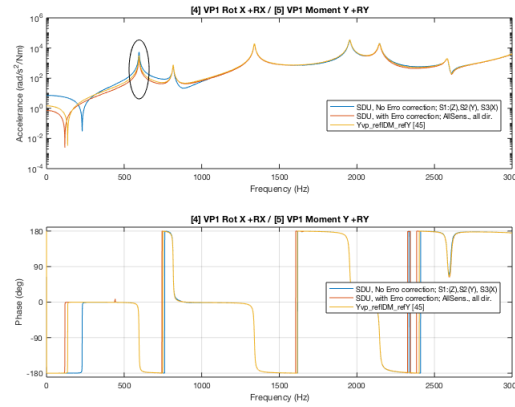
From Figure., C.5, C.2, C.3, and C.4 we can observe that VP 's elements [56], [45], [44], and [64] are respectively the most sensitive VP 's cross-functions to the sensor's directional errors, for lateral bending, vertical bending, torsion and torsion+lateral bending (mixed mode shape), respectively.

From results that partially is shown, we observed that element [46], [45], [44] and [64] are the most sensitive to SDU, when the sensors have some error cancellations.

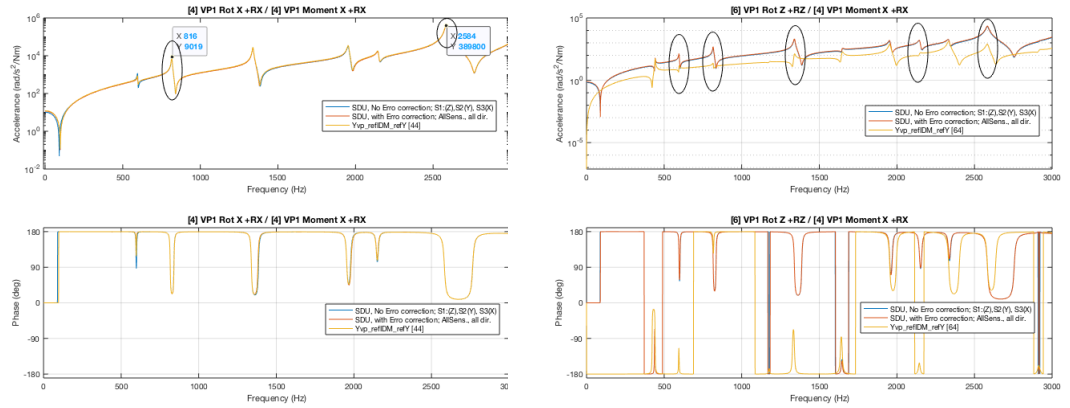
In order to see the effect of error cancellation we consider the FRF of element [56] and [46] VP 's admittance which contains the highest deviation on lateral bending(s) with- and without error cancellation. Figure.D.1 also shown element [45] which is the most sensitive cross-function for vertical bending, for both cases of with and without error cancellation. The FRF of cross-functions [44] and [64] are shown to see the effect of error cancellation in frequencies corresponds to a mode shape with torsion motion, and also for mixed motion (torsion+vertical bending).



(a) 56, lateral bending SDU WithAndWithoutErrorCancellation (b) 46, lateral bending SDU WithAndWithoutErrorCancellation



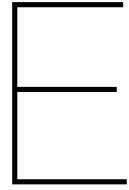
(c) 45 Vertical bending, SDU WithAndWithoutErrorCancellation



(d) 44, Torsion and torsion+vertical bending, SDU WithAndWithoutErrorCancellation

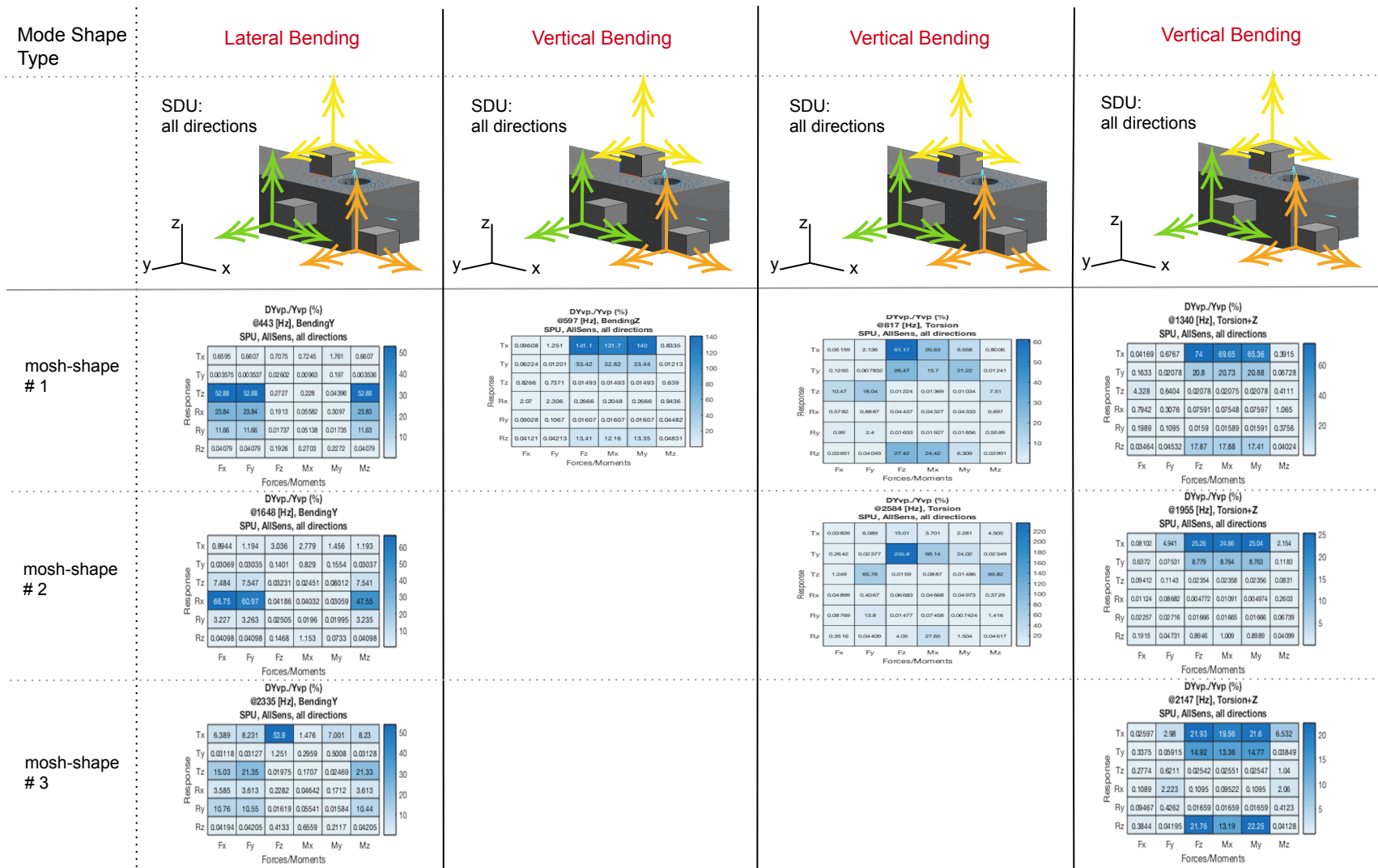
(e) 64, Torsion and torsion+vertical bending, SDU WithAndWithoutErrorCancellation

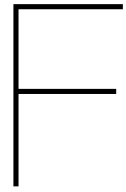
Figure D.1: Case IPU, comparison of the most sensitive cross-functions with and without error cancellation



Error propagation in percentage value;case SDU

Figure.E.1 shows the heatmap of percentage error, $P_{VP} = \frac{\Delta Y_{VP}}{Y_{VP,true}}$, for different type of mode shapes. From section.5.2.5 we expected that the percentage error on VP will decrease for higher *number* of a particular mode shape, for a certain amount of error. This results confirms the expectations for just one types of mode shapes (mixed mode shape of torsion and vertical bending), but not for all of them.

Figure E.1: Percentage value of propagated error to VP, case SDU, directional error is *exactly* 5 degree on all directions.



IPU; Impacts Positional Uncertainty

F.1. IPU, Impacts Positional uncertainty, No Error Cancellation, Non-symmetrical Error direction

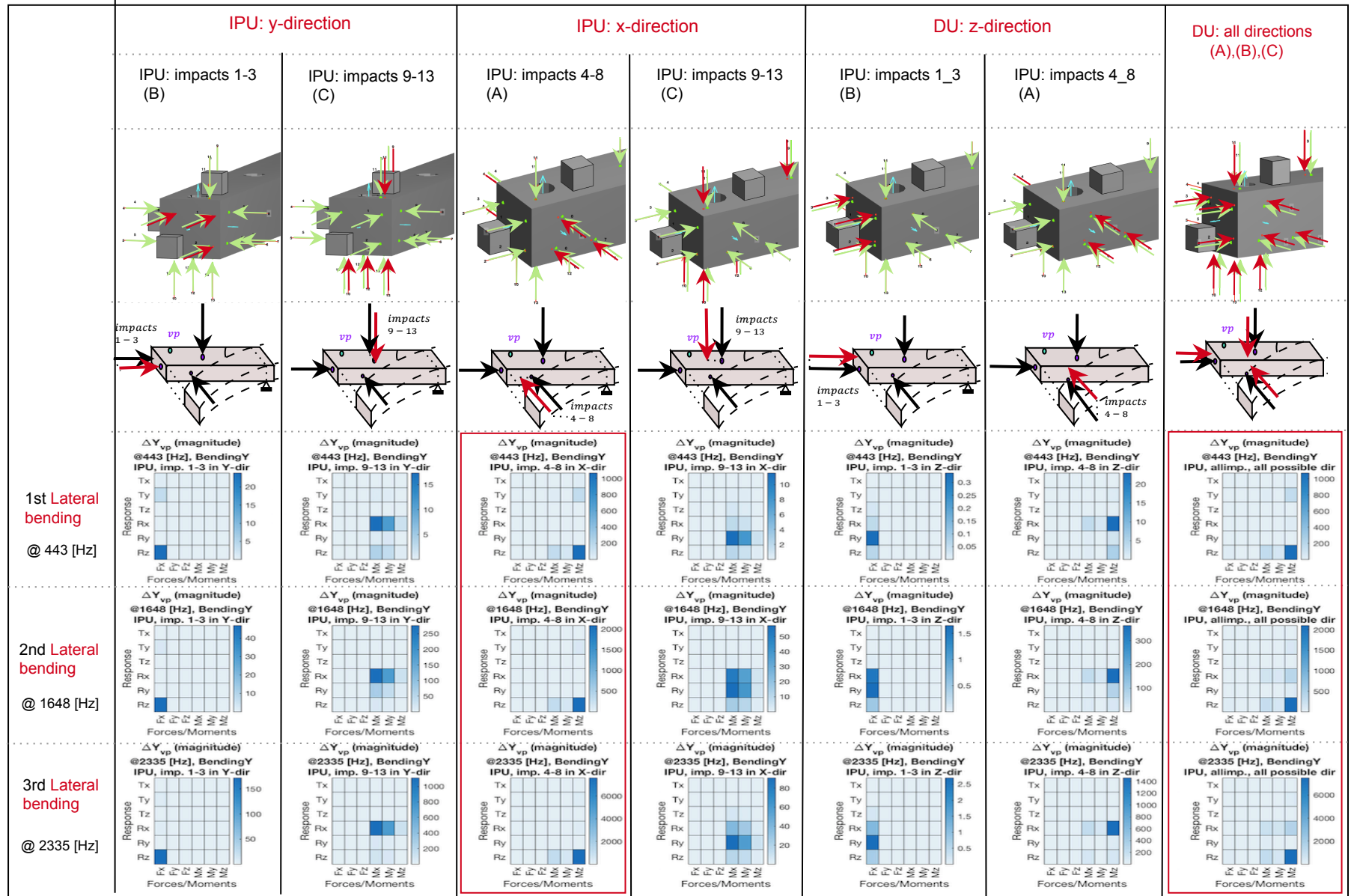


Figure F.1: Case IPU, NonSymetricalError NonSymetricalImpacts BendingY, Super position of errors for IPU Amount of directional error is exactly 2mm.

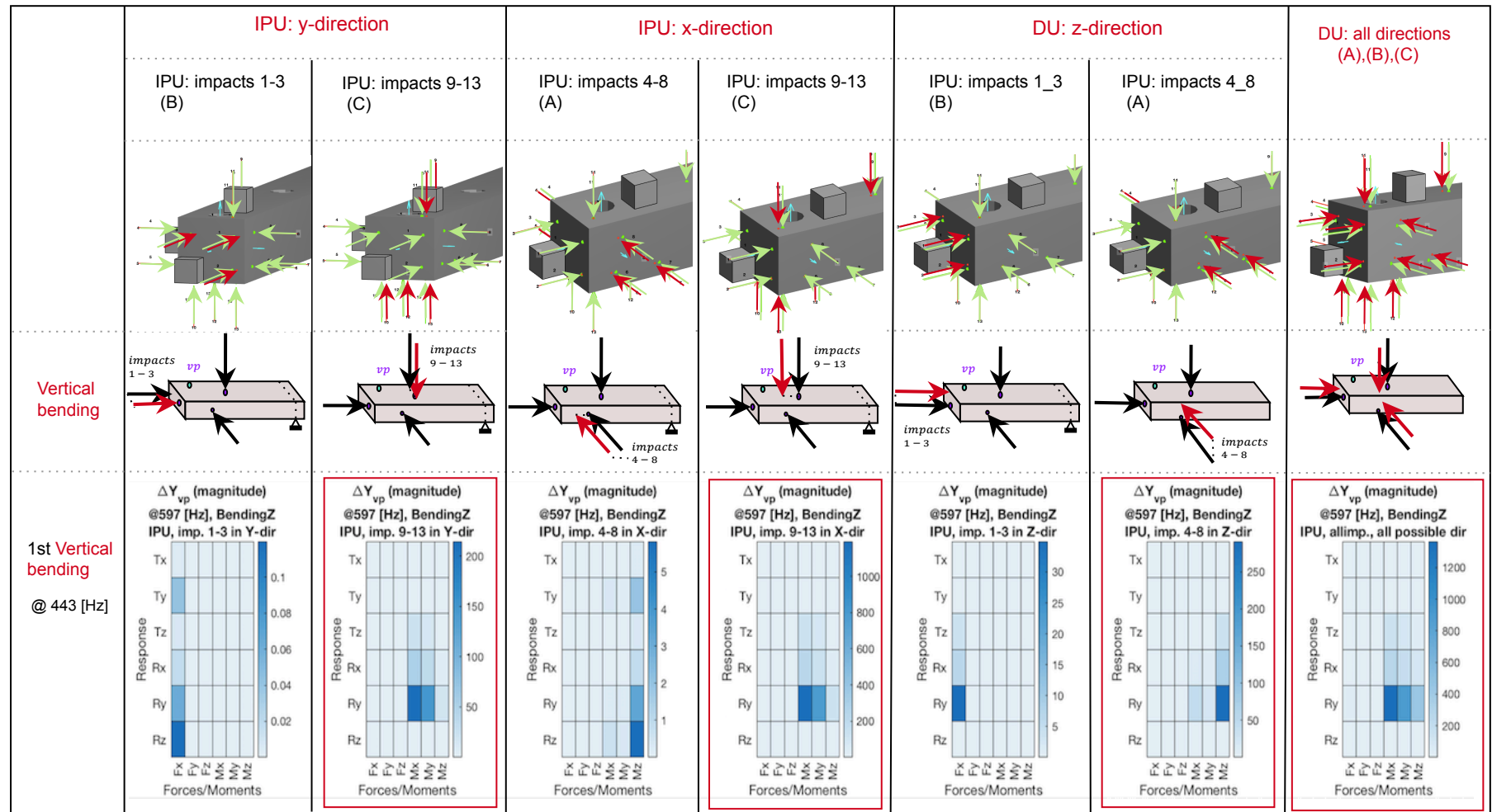


Figure F.2: Case IPU, NonSymetricalError NonSymetricalImpacts BendingZ, Super position of errors for IPU Amount of directional error is exact/y 2mm.

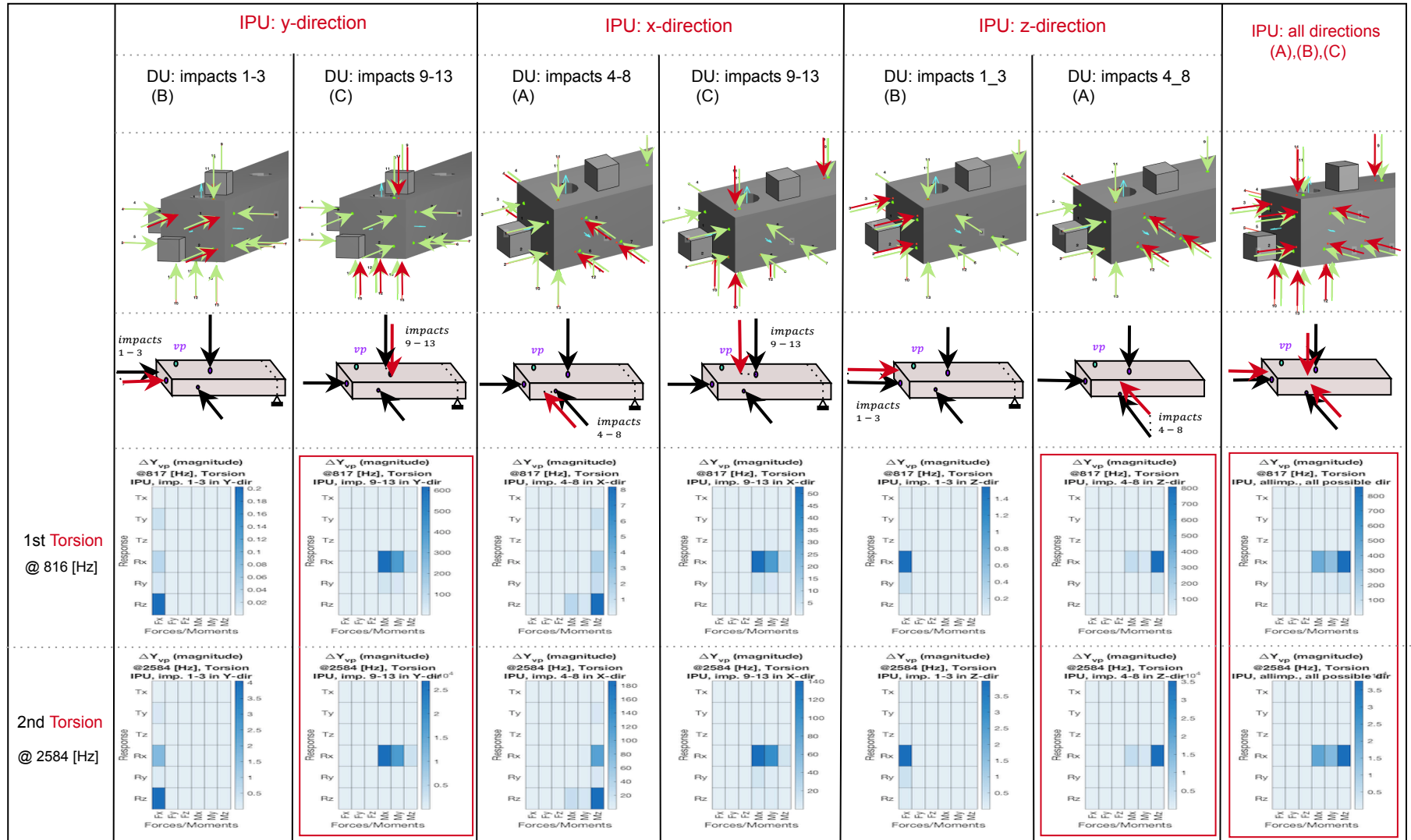


Figure F.3: Case IPU, NonSymmetricalError NonSymmetricalImpacts Torsion, Super position of errors for IPU Amount of directional error is exactly 2mm.

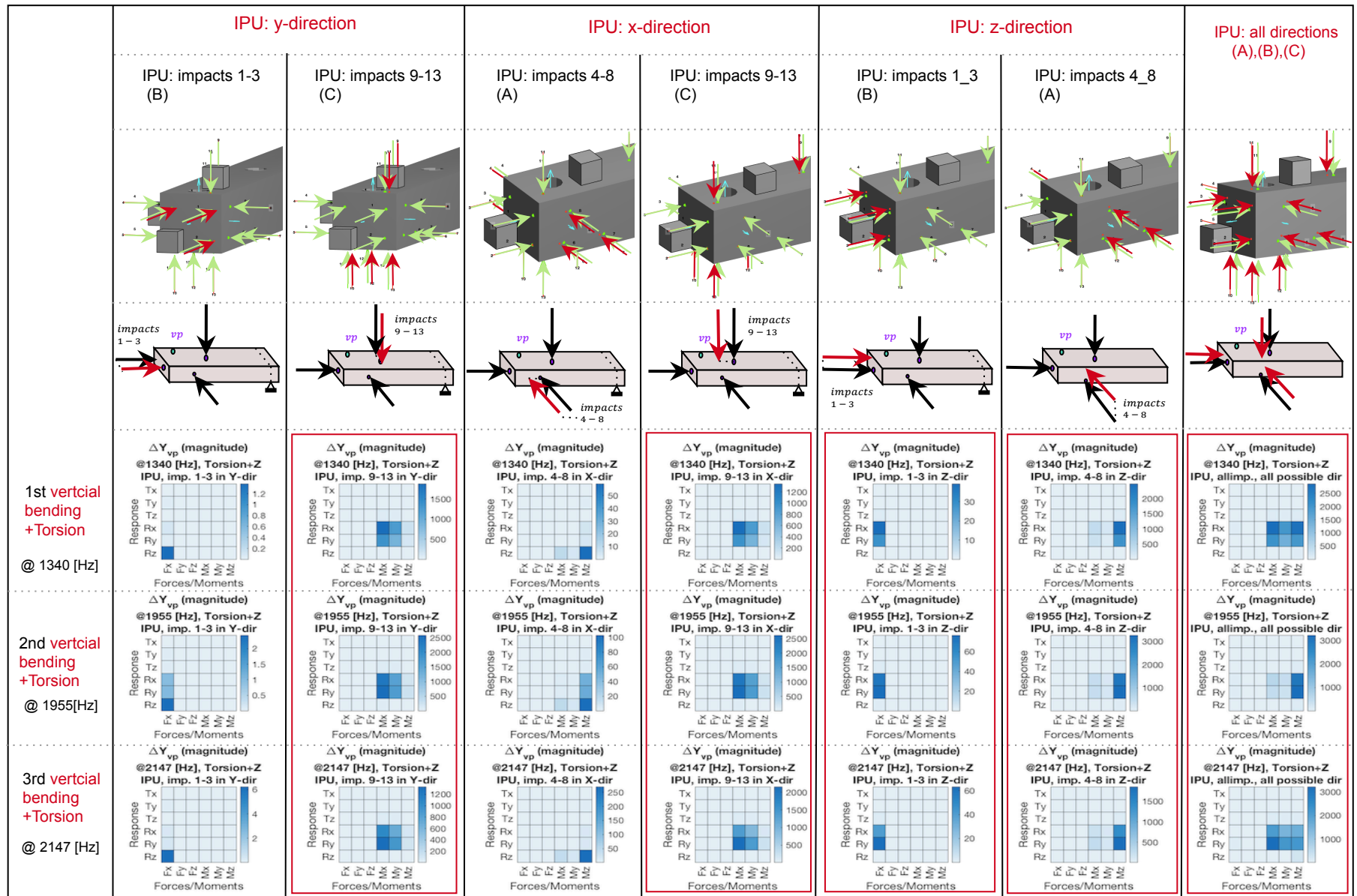


Figure F.4: Case IPU, NonSymmetricalError NonSymmetricalImpacts Torsion+BendingZ, Super position of errors for IPU Amount of directional error is exactly 2mm.

F.2. IPU, Impacts Positional uncertainty, with Error Cancellation

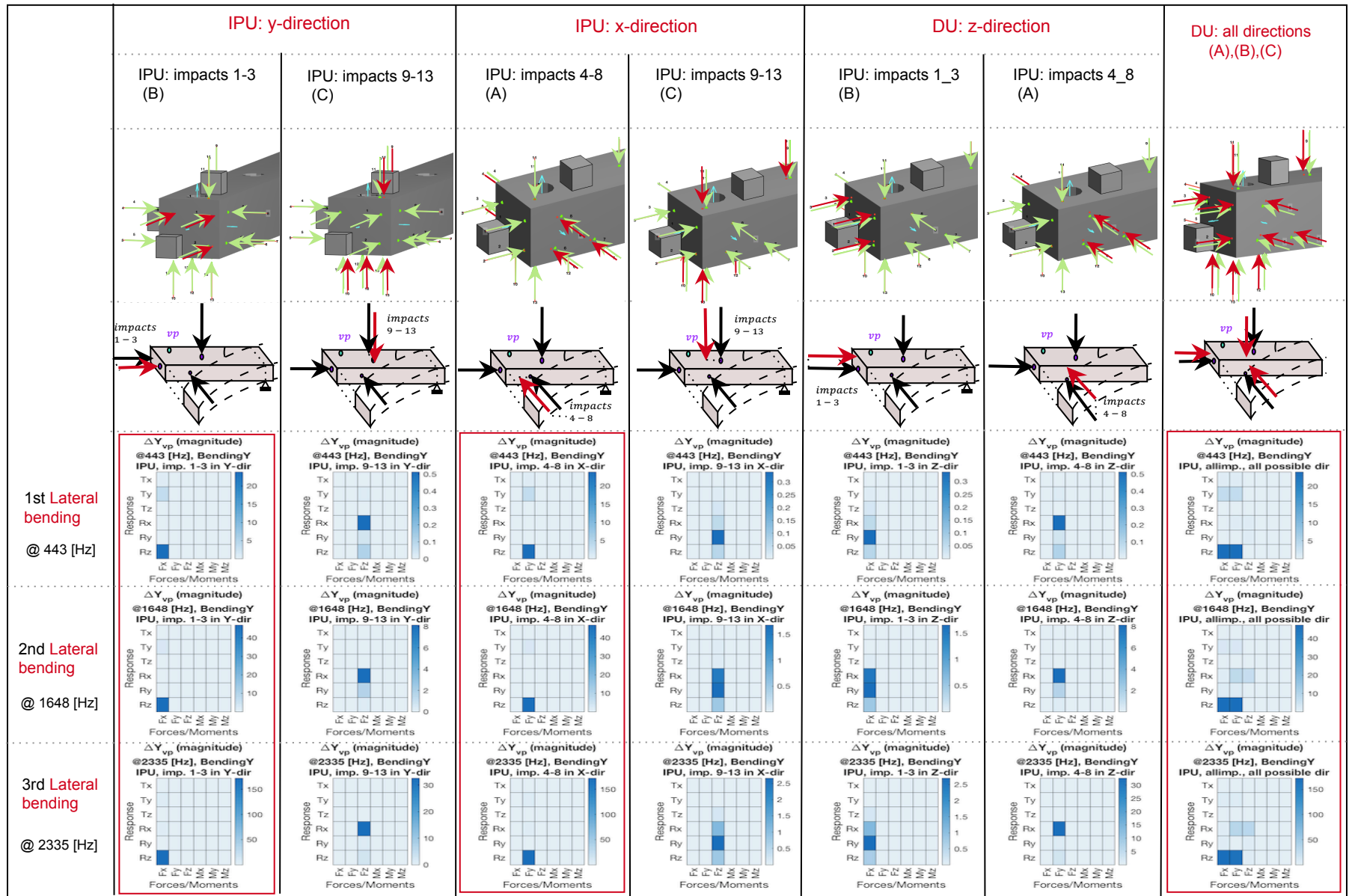


Figure F.5: Case IPU, SymetricalError NonSymetricalImpacts BendingY, Super position of errors for IPU Amount of directional error is *exactly* 2mm.

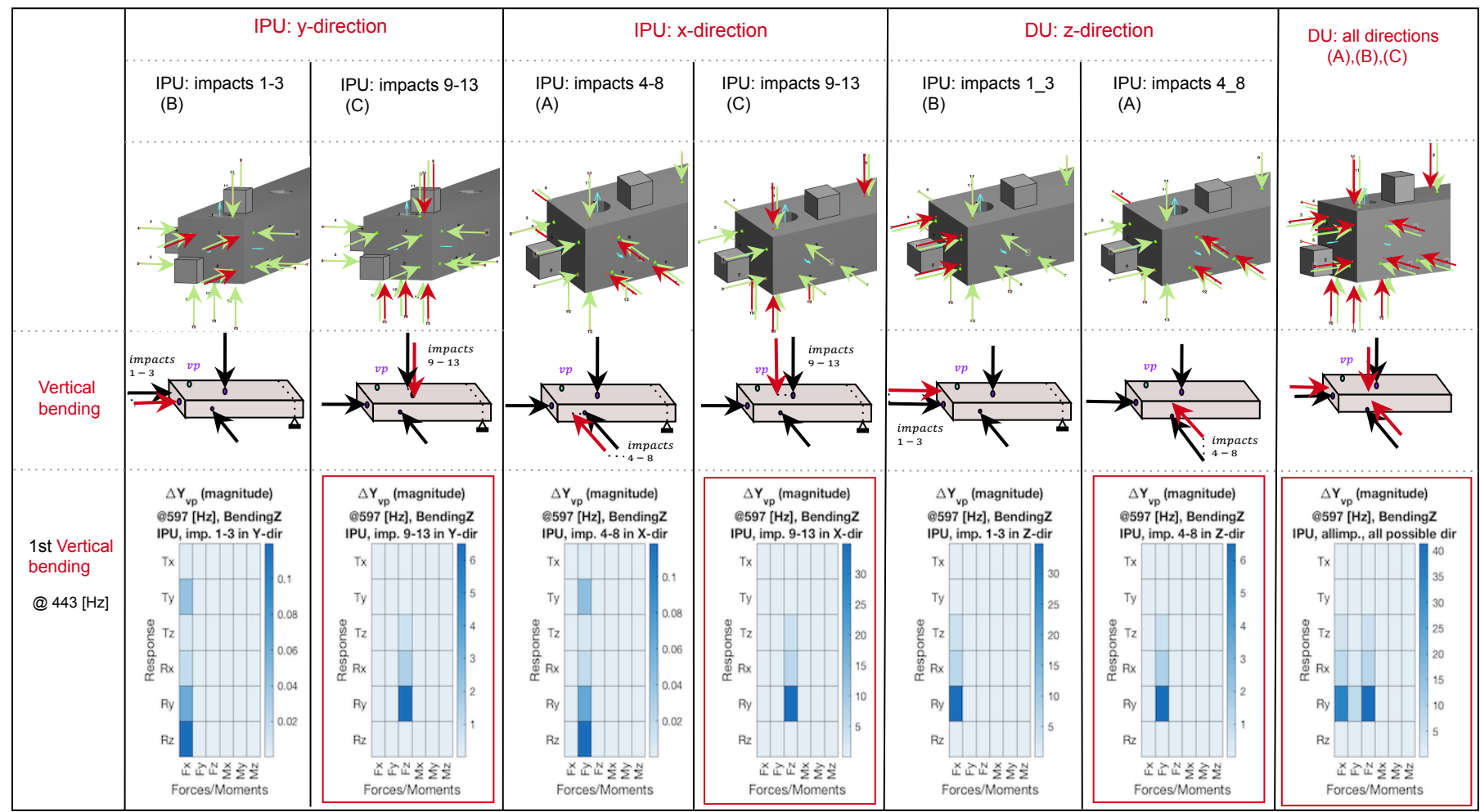


Figure F.6: Case IPU, SymmetricalError NonSymmetricalImpacts BendingZ, Super position of errors for IPU Amount of directional error is exactly 2mm.

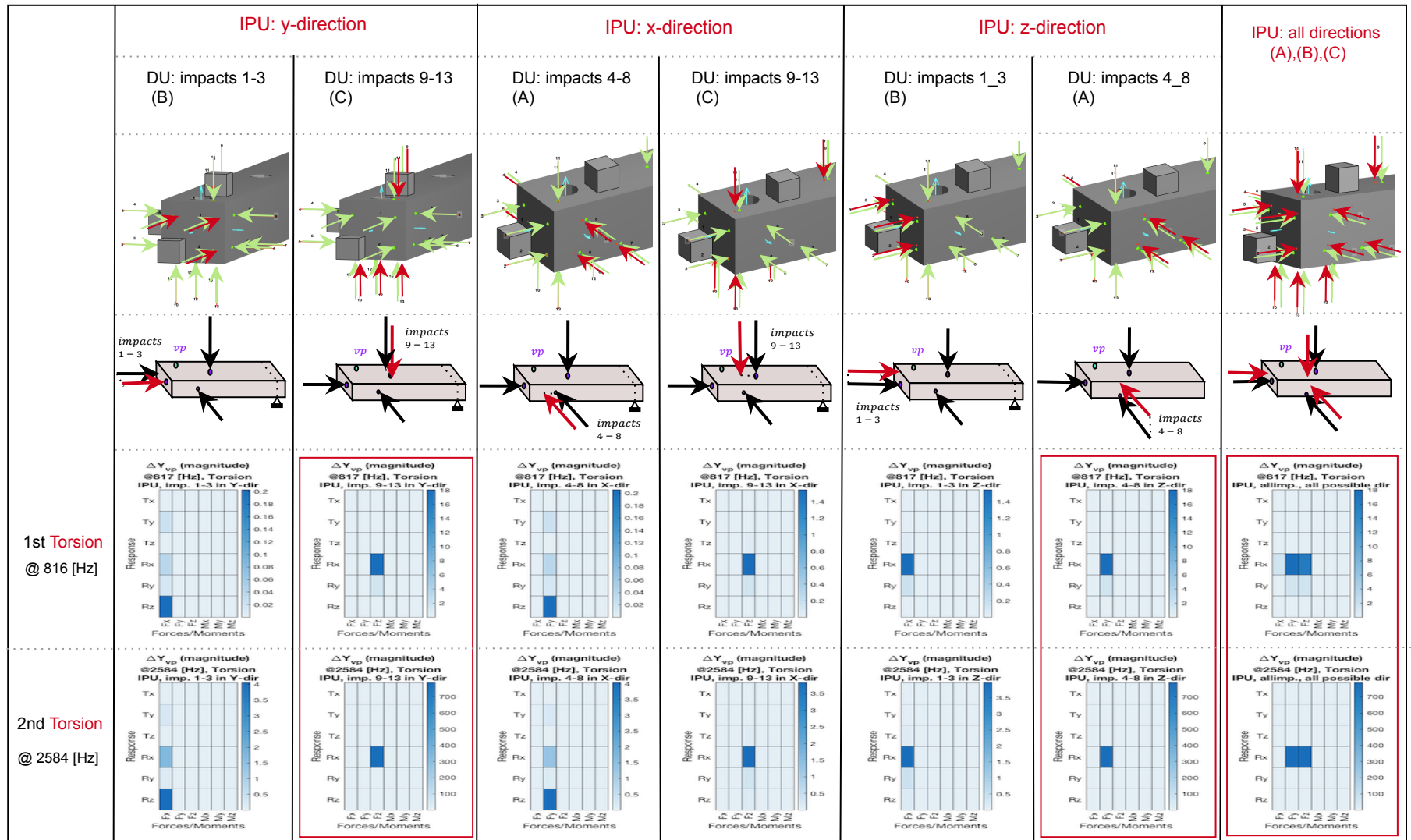


Figure F.7: Case IPU, SymmetricalError NonSymmetricalImpacts Torsion, Super position of errors for IPU Amount of directional error is *exactly* 2mm.

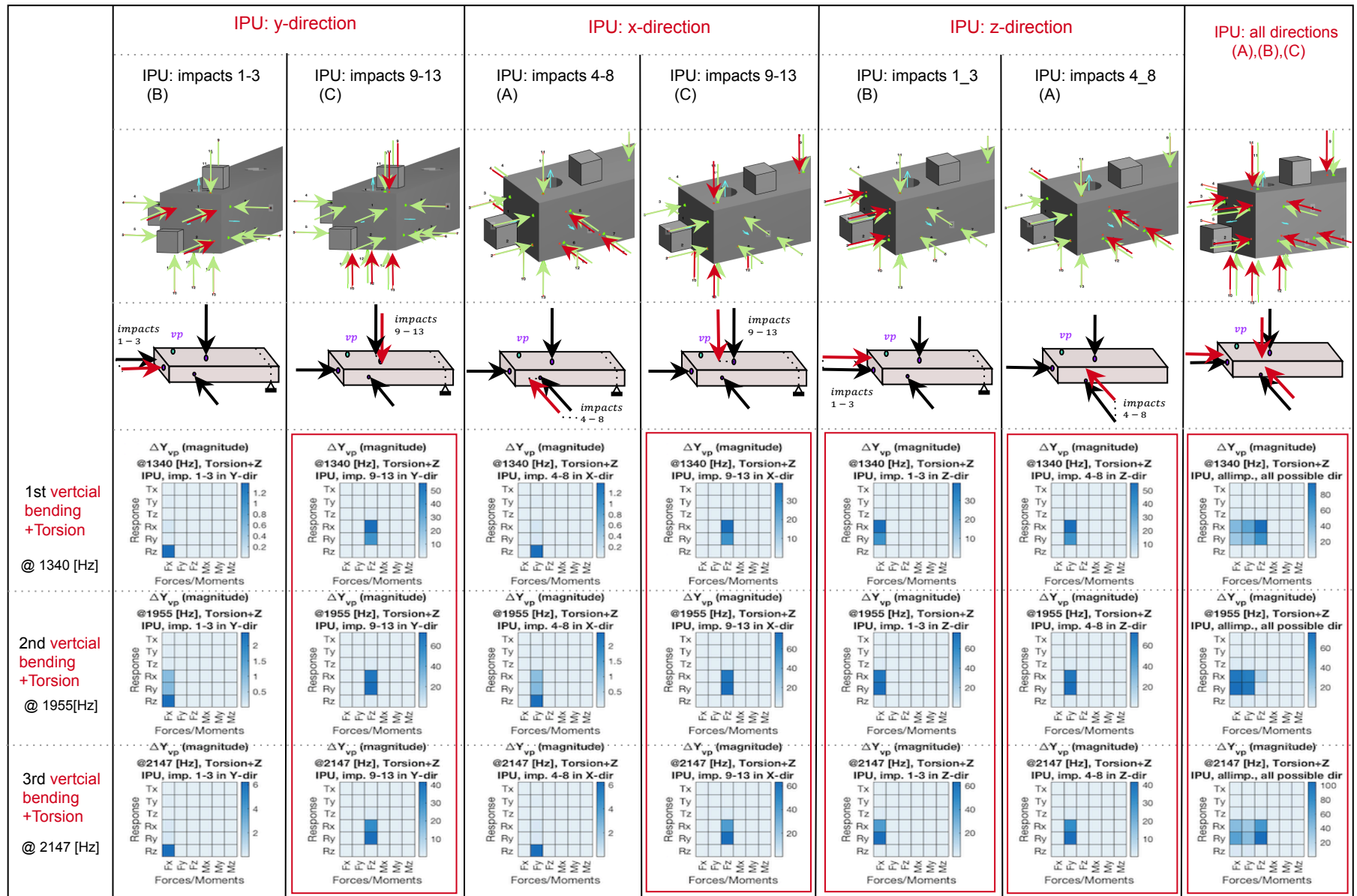
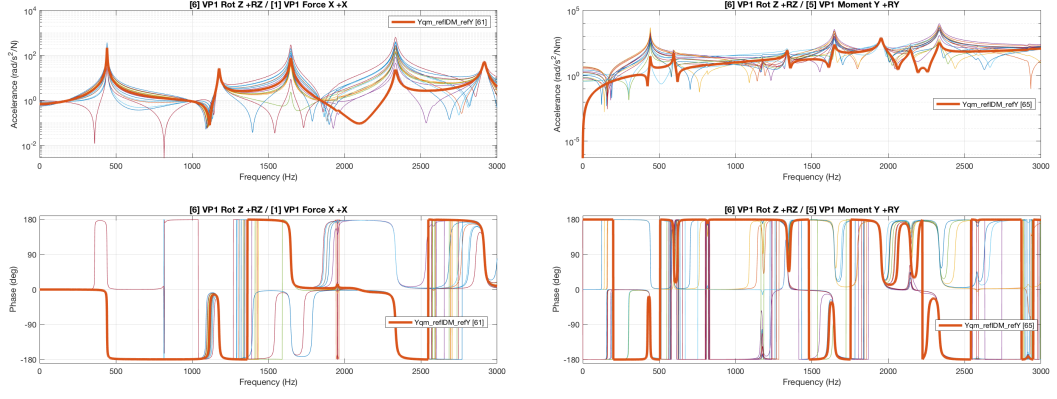


Figure F.8: Case IPU, SymetricalError NonSymetricalImpacts Torsion+BendingZ, Super position of errors for IPU Amount of directional error is exactly 2mm.

F.2.1. FRF of most sensitive cross-functions for dominant error sources

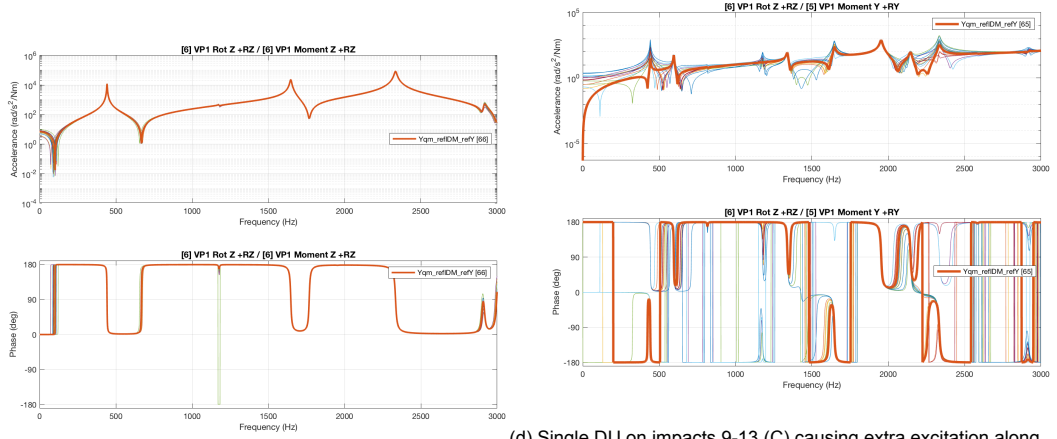
Now we are applying an error with different values (which are around 5 degree) randomly and for each independent impact target.

Comparing Figure.F.9b and F.9d confirms our expectations from analytical approach. In these two cross-functions we can see that uncertainty with the same direction as mode shape (Figure.F.9b, implement uncertainty on y-direction on impacts 9-13) causes a higher deviation, than on a direction (Figure.F.9b, implement uncertainty on x-direction on impacts 9-13) where the corresponding modal values for this mode shape are smaller.



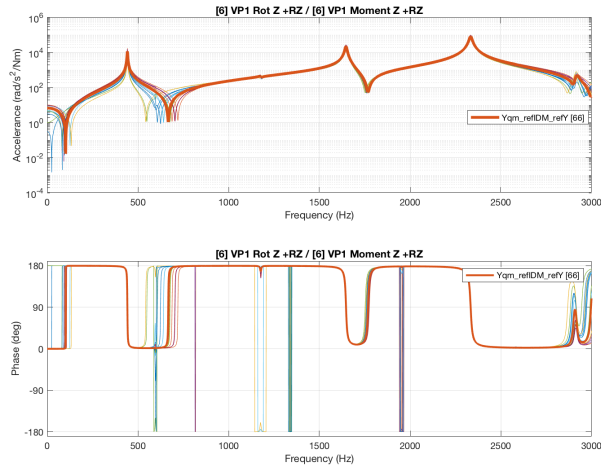
(a) Single DU on impacts 1,2,3 (B) causing extra excitation along y-direction, which causes dominant deviation on element [61] (θ_z/M_x) of VP. The dominant effect of this uncertainty is the most on frequencies corresponds to lateral bending (340, 1648, and 2335 [Hz]), with a motion also along y-direction.

(b) Single DU on impacts 9-13 (C) causing extra excitation along y-direction, which causes dominant deviation on element [65] (θ_z/M_y) of VP. The dominant effect of this uncertainty is the most on frequencies corresponds to lateral bending (340, 1648, and 2335 [Hz]), with a motion also along y-direction.



(c) Single DU on impacts 4-8 (A) causing extra excitation along x-direction, which causes dominant deviation on element [66] (θ_z/M_z) of VP.

(d) Single DU on impacts 9-13 (C) causing extra excitation along x-direction, which causes dominant deviation on element [65] (θ_z/M_y) of VP. The dominant effect of this uncertainty is the most on frequencies corresponds to lateral bending (340, 1648, and 2335 [Hz]), with a motion also along y-direction.



(e) Multiple DU (randomly and independently for each direction) on all impacts (A,B,C), which causes dominant deviation on element [65] (θ_z/M_y), [66] (θ_z/M_z) and [64] (θ_z/M_x) of VP.

Figure F.9: Frequency response function of virtual point (coupling point) elements containing the most deviation in the presence of directional uncertainty. (a),(b),(c) and (d) are the cases where single directional uncertainty is applied on just a group of impacts with the same reference direction. The amount of these directional errors are independently and randomly chosen for the targeted impacts. (d) is the case where all impacts have directional uncertainty, which are chosen independently and randomly for each impact and each direction. For each case the process is repeated for 15 times, each time each directional uncertainty is randomly and independently chosen for each impact with a value of *around* 5 degree.



Effect of error cancellation, case IPU

From Figure., F.1, F.2, F.3, and F.4 we can observe that VP 's elements [66], [54], [46], and [46] are respectively the most sensitive VP 's cross-functions to the impact's positional errors, for lateral bending, vertical bending, torsion and torsion+lateral bending (mixed mode shape), respectively.

The frequency response function of these least precise cross-functions of VP 's are shown in Figure.D.1b, D.1c, D.1e. These figures compares the effect of error cancellation on the FRF of the most sensitive cross-functions of VP , for each type of mode shape. For each case all impacts have a positional error of 2 mm.

Figure., F.5, F.6, F.7, and F.8 show the heatmaps of the case of error cancellation on IPU. From this figures we can see that elements [61], [51], [42] and [43] of VP are the most sensitive cross-functions. The FRF of these cross-functions and the influence of error cancellation is also shown in Figure.G.1.

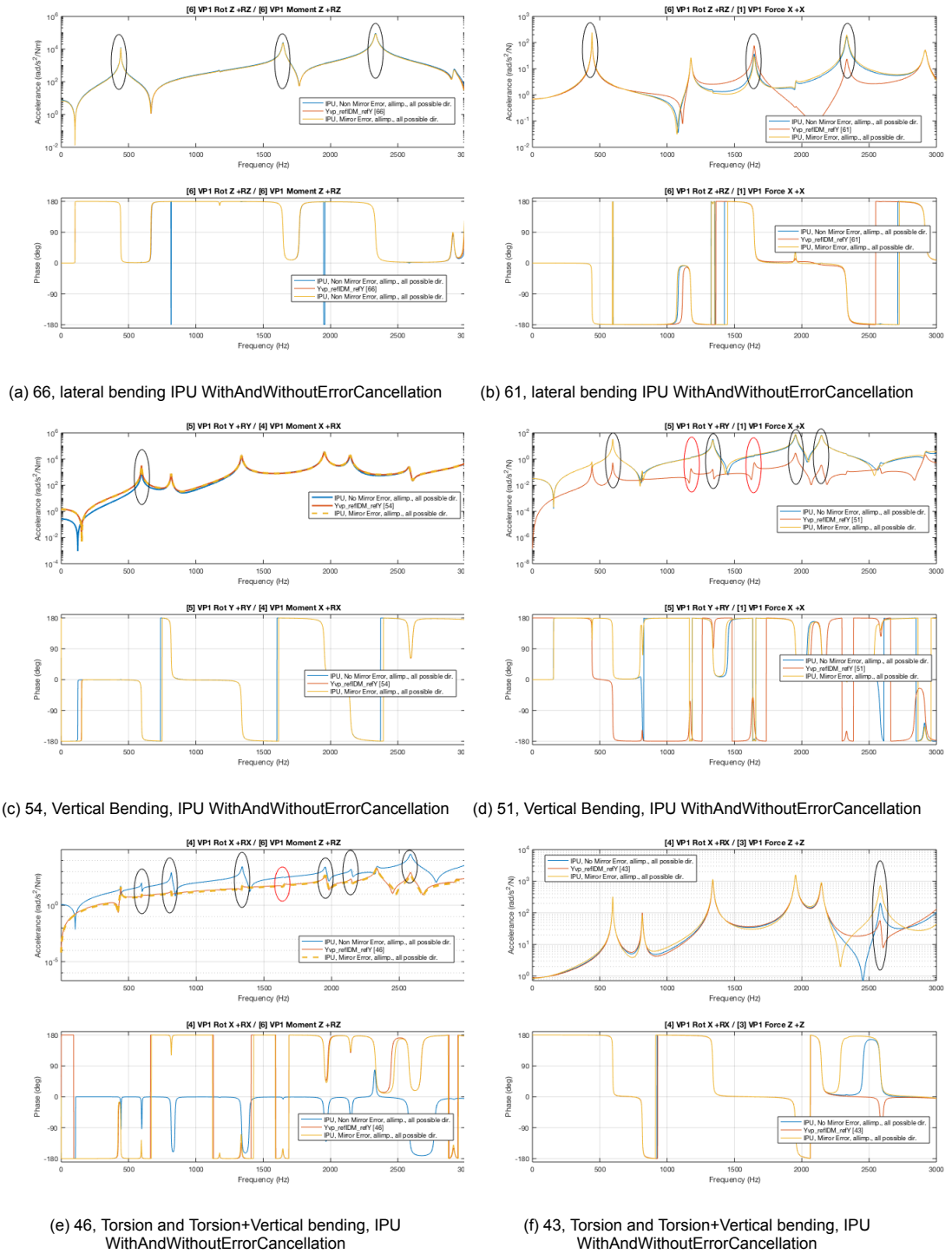
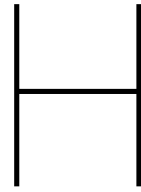


Figure G.1: Case IPU, comparison of the most sensitive cross-functions with and without error cancellation



Case SPU; Sensors Positional Uncertainty

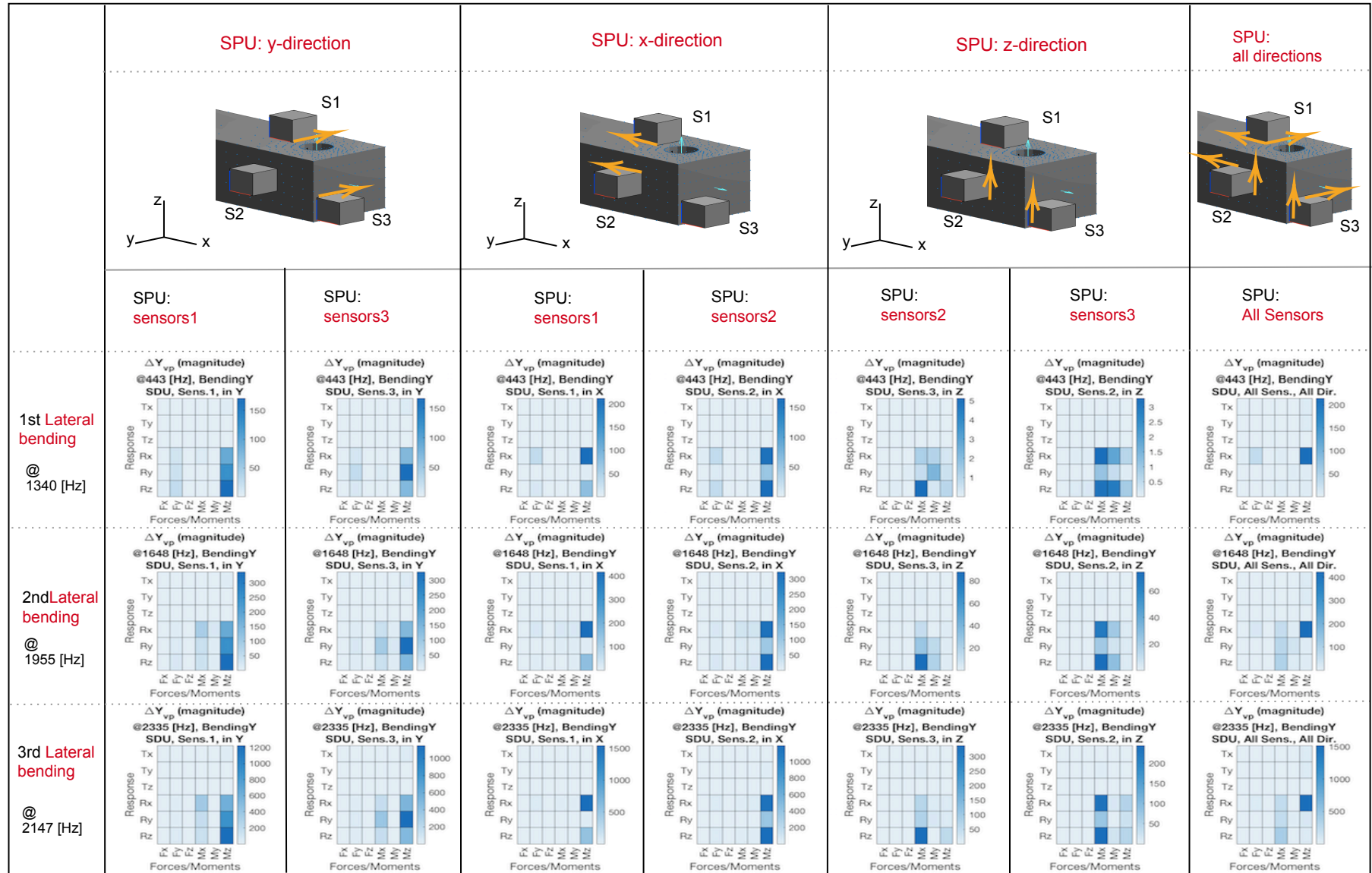


Figure H.1: SPU LateralBending

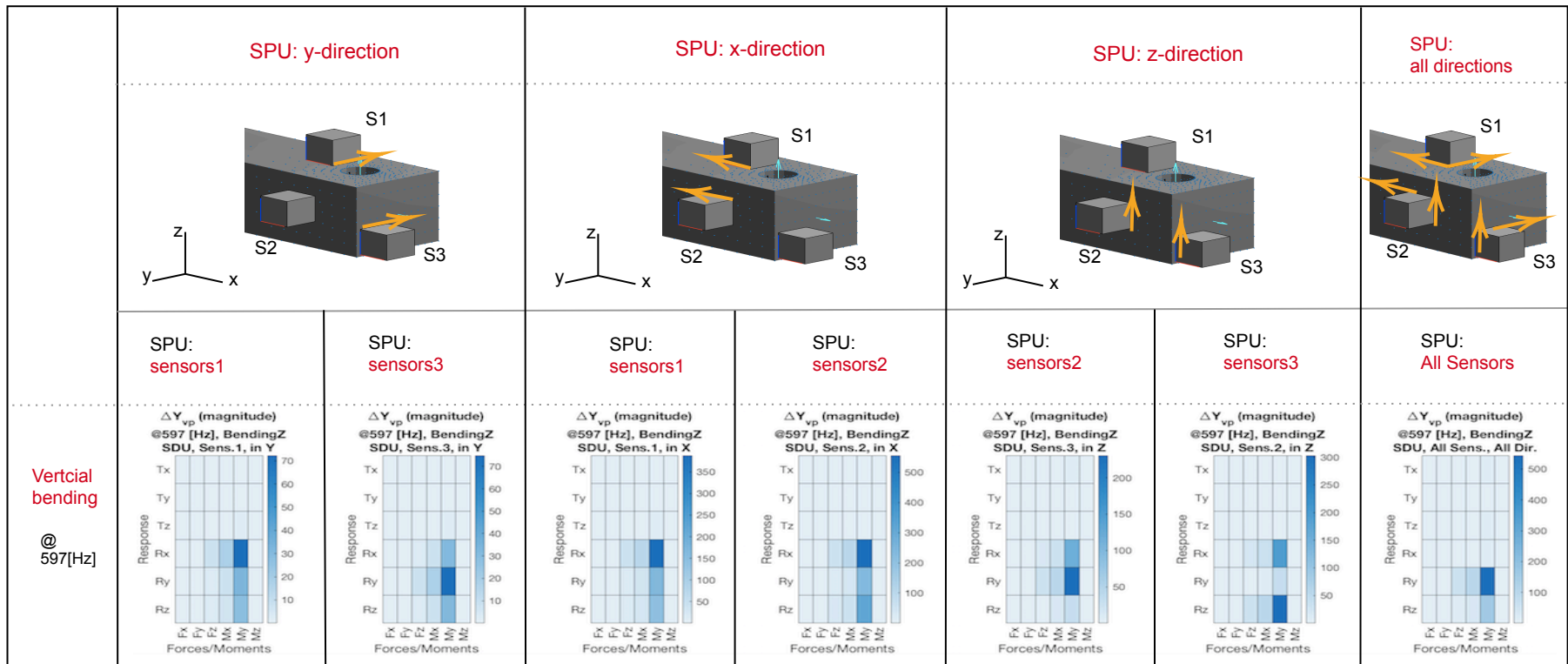


Figure H.2: SPU verticalBending

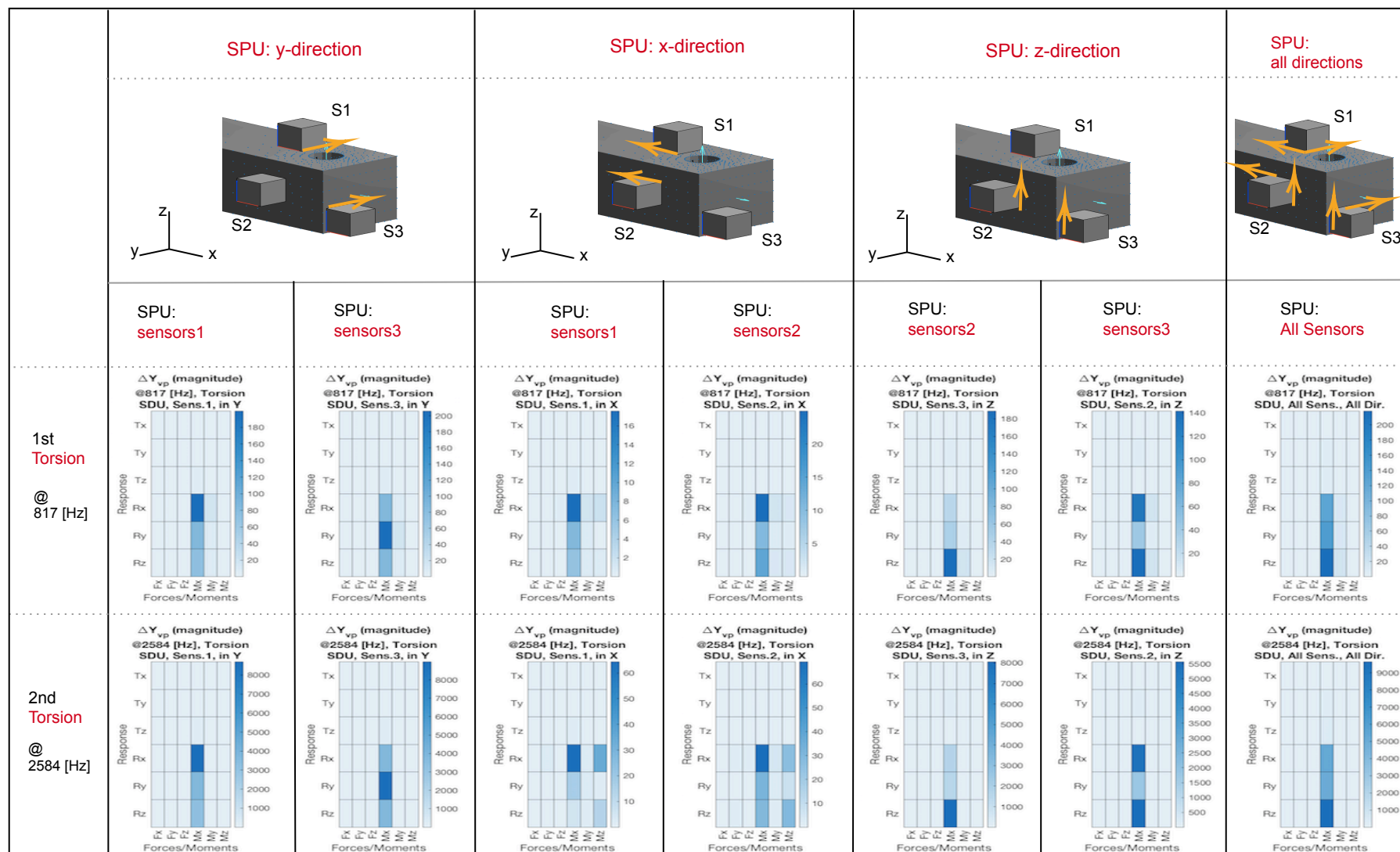


Figure H.3: SPU Torsion

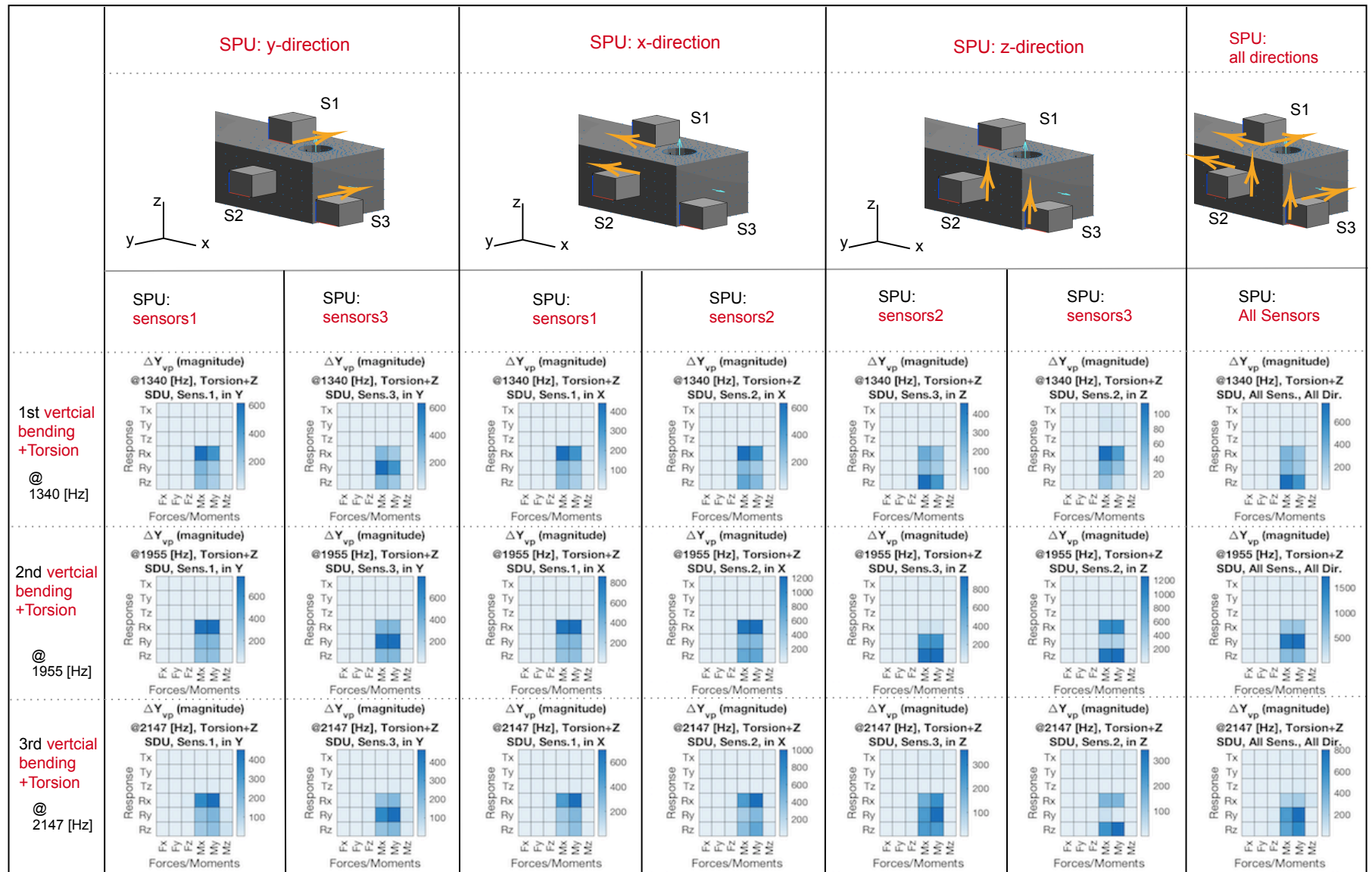
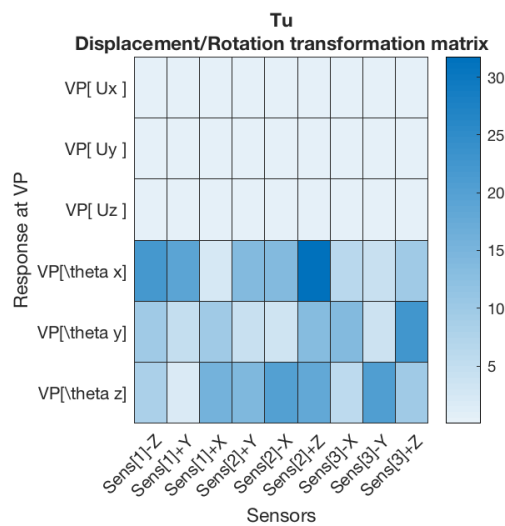


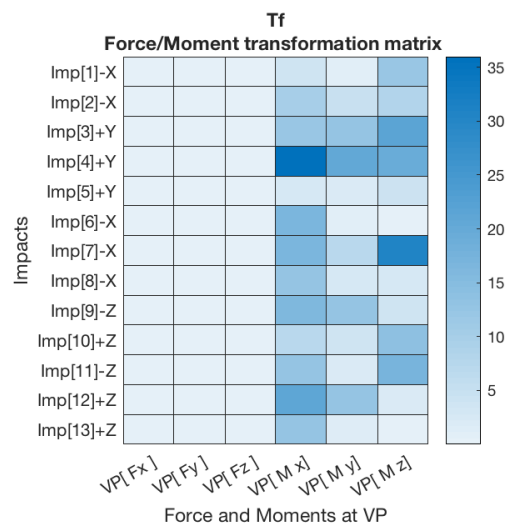
Figure H.4: SPUTorsion+verticalBending

Transformation matrices

The heatmaps (absolute value) of reference transformation matrices for configuration presented on section.5.3 is shown in Figure.I.1a and I.1b. As expected (analytical approach, section.??) the lower part of displacement transformation has highest values, and the right part of force transformation matrix contains the highest values.



(a) caption



(b) caption

Bibliography

- [1] Matthew S Allen and Randall L Mayes. Estimating the degree of nonlinearity in transient responses with zeroed early-time fast fourier transforms. *Mechanical Systems and Signal Processing*, 24(7): 2049–2064, 2010.
- [2] Matthew S Allen, Daniel C Kammer, and Randall L Mayes. Uncertainty in experimental/analytical substructuring predictions: a review with illustrative examples. In *International Conference on Noise and Vibration Engineering (ISMA), Leuven, Belgium, Sept*, pages 20–22, 2010.
- [3] Matthew S Allen, Randall L Mayes, and Elizabeth J Bergman. Experimental modal substructuring to couple and uncouple substructures with flexible fixtures and multi-point connections. *Journal of Sound and Vibration*, 329(23):4891–4906, 2010.
- [4] Matthew S Allen, Daniel Rixen, Maarten van der Seijs, Paolo Tiso, Thomas Abrahamsson, and Randall L Mayes. *Substructuring in Engineering Dynamics: Emerging Numerical and Experimental Techniques*, volume 594. Springer, 2019.
- [5] RAB Almeida, APV Urgueira, and NMM Maia. Identification of rigid body properties from vibration measurements. *Journal of sound and vibration*, 299(4-5):884–899, 2007.
- [6] Javad Baqersad, Peyman Poozesh, Christopher Niezrecki, and Peter Avitabile. Comparison of modal parameters extracted using mimo, simo, and impact hammer tests on a three-bladed wind turbine. In *Topics in Modal Analysis II, Volume 8*, pages 185–197. Springer, 2014.
- [7] Robert D Blevins. Formulas for natural frequency and mode shape. 1979.
- [8] David L Brown, Randall J Allemang, and Allyn W Phillips. Forty years of use and abuse of impact testing: a practical guide to making good frf measurements. In *Experimental Techniques, Rotating Machinery, and Acoustics, Volume 8*, pages 221–241. Springer, 2015.
- [9] DL Brown. Weaknesses of impact testing. In *Proceedings-Spie The International Society For Optical Engineering*, pages 1672–1676. spie International Society for optical, 1997.
- [10] RL Campbell and SA Hambric. Application of frequency domain substructure synthesis technique for plates loaded with complex attachments. Technical report, Pennsylvania State Univ University Park Applied Research Lab, 2004.
- [11] Thomas G Carne and Clark R Dohrmann. Improving experimental frequency response function matrices for admittance modeling. In *Proceedings of the Nineteenth International Modal Analysis Conference*, 2006.
- [12] James W Cooley and John W Tukey. An algorithm for the machine calculation of complex fourier series. *Mathematics of computation*, 19(90):297–301, 1965.
- [13] K Cuppens, Paul Sas, and L Hermans. Evaluation of the frf based substructuring and modal synthesis technique applied to vehicle fe data. In *Proceedings of the International Seminar on Modal Analysis*, volume 3, pages 1143–1150. KU Leuven; 1998, 2001.
- [14] D. de Klerk. How bias errors affect experimental dynamic substructuring. *International Modal Analysis Conference (IMAC XXVIII)*, 28, 2010.
- [15] D De Klerk and S Voormeeren. Uncertainty propagation in experimental dynamic substructuring. In *Proceedings of the Twenty Sixth International Modal Analysis Conference, Orlando, FL*. Society for Experimental Mechanics Bethel, CT, 2008.

- [16] Dennis de Klerk, D Rixen, SN Voormeeren, and Fs Pasteuning. Solving the rdof problem in experimental dynamic substructuring. In *26th International Modal Analysis Conference (IMAC XXVI)*, Orlando, FL, 2008.
- [17] MLM Duarte and DJ Ewins. Some insights into the importance of rotational degrees-of-freedom and residual terms in coupled structure analysis. In *Proceedings-Spie The International Society For Optical Engineering*, pages 164–164. Spie The International Society For Optical, 1995.
- [18] John Faragher. Probabilistic methods for the quantification of uncertainty and error in computational fluid dynamic simulations. Technical report, Defence Science And Technology Organization Victoria (Australia) Air, 2004.
- [19] Jimin He and Zhi-Fang Fu. 7 - Frequency response function measurement. In Jimin He and Zhi-Fang Fu, editors, *Modal Analysis*, pages 140–158. Butterworth-Heinemann, Oxford, 2001. ISBN 978-0-7506-5079-3. doi: <https://doi.org/10.1016/B978-075065079-3/50007-3>. URL <http://www.sciencedirect.com/science/article/pii/B9780750650793500073>.
- [20] Stefaan Helderweirt, Herman Van der Auweraer, Peter Mas, Luigi Bregant, and Daniele Casagrande. Application of accelerometer-based rotational degree of freedom measurements for engine subframe modelling. In *IMAC-XIX: A Conference on Structural Dynamics*, volume 2, pages 1298–1304, 2001.
- [21] L Hermans, P Mas, W Leurs, and N Boucart. Estimation and use of residual modes in modal coupling calculations: A case study, # 329. In *Proceedings of IMAC-XVIII: A Conference on Structural Dynamics*, volume 4062, page 930, 2000.
- [22] Toshihiko Horiuchi and Takao Konno. A new method for compensating actuator delay in real-time hybrid experiments. *Philosophical Transactions of the Royal Society of London. Series A: Mathematical, Physical and Engineering Sciences*, 359(1786):1893–1909, 2001.
- [23] N Hunter and T Paez. Nonlinear behavior of a 45 degree bolted lap joint. In *Proceedings of the Twentyfourth International Modal Analysis Conference, St. Louis, MO. Society for Experimental Mechanics, Bethel, CT*, 2006.
- [24] M Imregun, D A Robb, and D J Ewins. Structural modification and coupling dynamic analysis using measured frf data. *5th International Modal Analysis Conference (IMAC V)*, pages 2049–2064, 1987.
- [25] H Kanda, ML Wei, RJ Allemang, and DL Brown. Structural dynamic modification using mass additive technique. In *4th International Modal Analysis Conference (IMAC IV)*, 1986.
- [26] D de Klerk, Daniel J Rixen, and SN Voormeeren. General framework for dynamic substructuring: history, review and classification of techniques. *AIAA journal*, 46(5):1169–1181, 2008.
- [27] Dirk P Kroese, Thomas Taimre, and Zdravko I Botev. *Handbook of monte carlo methods*, volume 706. John Wiley Sons, 2013.
- [28] A Liljerehn and Thomas Abrahamsson. Dynamic sub-structuring with passive state-space components. In *26th International Conference on Noise and Vibration Engineering, ISMA 2014, Including the 5th International Conference on Uncertainty in Structural Dynamics, USD 2014; Leuven; Belgium; 15 September 2014 through 17 September 2014*, pages 3879–3890, 2014.
- [29] W Liu and D Ewins. The importance assessment of rdof in frf coupling analysis. In *Proceedings of the seventeenth international modal analysis conference, Orlando, FL*, pages 1481–1487. Citeseer, 1999.
- [30] Daryl L Logan. *A first course in the finite element method*. Cengage Learning, 2011.
- [31] KD Mali and PM Singru. Study on the effect of the impact location and the type of hammer tip on the frequency response function (frf) in experimental modal analysis of rectangular plates. In *IOP Conference Series: Materials Science and Engineering*, volume 330, page 012102. IOP Publishing, 2018.

- [32] Randall L Mayes and Matthew S Allen. Comparison of frf and modal methods for combining experimental and analytical substructures. Technical report, Sandia National Lab.(SNL-NM), Albuquerque, NM (United States), 2007.
- [33] Merriam-webster.com. Systematic errors, 2019. URL <https://www.merriam-webster.com/dictionary/systematic%20error>.
- [34] Nicholas Metropolis and Stanislaw Ulam. The monte carlo method. *Journal of the American statistical association*, 44(247):335–341, 1949.
- [35] Himanshu Mevada and Dipal Patel. Experimental determination of structural damping of different materials. *Procedia Engineering*, 144:110–115, 2016.
- [36] Diogo Montalvão, AMR Ribeiro, NMM Maia, and JMM Silva. Estimation of the rotational terms of the dynamic response matrix. *Shock and Vibration*, 11(3-4):333–350, 2004.
- [37] Lennart Nieuwenhuijse, Eric Pasma, Mathieu Wernsen, and Peter Steeneken. Experimental dynamic substructuring and its application in automotive research, 2018.
- [38] John C O'CALLAHAN. System equivalent reduction expansion process. In *Proc. of the 7th Inter. Modal Analysis Conf.*, 1989, 1989.
- [39] John C O'Callahan, Peter Aitavale, and Chaur Choi. Consistent scaling of rigid body and experimental flexural modes. In *International Modal Analysis Conference, 5th, London, England*, pages 1538–1544, 1987.
- [40] Bernt Øksendal. Stochastic differential equations. In *Stochastic differential equations*, pages 65–84. Springer, 2003.
- [41] John C O'Callahan, Inn-Wei Lieu, and Chaur-Ming Chou. Determination of rotational degrees of freedom for moment transfers in structural modifications. In *Proceedings of the Third International Modal Analysis Conference, Orlando, FL*, pages 465–470, 1985.
- [42] F Pasteuning. Robust experimental dynamic substructuring: Enhanced quality indicators application of semm to an industrial case, 2007.
- [43] S Unnikrishna Pillai and A Papoulis. *Probability, random variables, and stochastic processes*. McGraw-Hill Higher Education, New York, NY USA, 2002.
- [44] Xinlin P Qing, Hian-Leng Chan, Shawn J Beard, Teng K Ooi, and Stephen A Marotta. Effect of adhesive on the performance of piezoelectric elements used to monitor structural health. *International Journal of Adhesion and Adhesives*, 26(8):622–628, 2006.
- [45] Daniel J Rixen. How measurement inaccuracies induce spurious peaks in frequency based substructuring. In *26th International Modal Analysis Conference, Orlando, FL, Feb*, page 87, 2008.
- [46] Brian J Schwarz and Mark H Richardson. Experimental modal analysis. *CSI Reliability week*, 35(1):1–12, 1999.
- [47] Daniel J Segalman. A four-parameter iwan model for lap-type joints. *Journal of Applied Mechanics*, 72(5):752–760, 2005.
- [48] John Taylor. *Introduction to error analysis, the study of uncertainties in physical measurements*. 1997.
- [49] MV Van der Seijs. *Experimental dynamic substructuring: analysis and design strategies for vehicle development*. PhD thesis, 2016.
- [50] SN Voormeeren, D De Klerk, and DJ Rixen. Uncertainty quantification in experimental frequency based substructuring. *Mechanical Systems and Signal Processing*, 24(1):106–118, 2010.
- [51] C Yang, DE Adams, S-W Yoo, and H-J Kim. An embedded sensitivity approach for diagnosing system-level vibration problems. *Journal of sound and vibration*, 269(3-5):1063–1081, 2004.